

# Fabrication of Lithiated Boron Doped Diamond on Tungsten for Field Emission Testing

---

**Devan Panchal**

April 2014



University of  
**BRISTOL**

*A dissertation submitted to the University of Bristol in accordance with the requirements for the award of the Honours degree of Master of Science in Chemistry*

Supervisor: Dr. N.A Fox

Second Assessor: Professor P.W. May



## Acknowledgements

First and foremost, hearty thanks go to Dr. Neil Fox for his unending enthusiasm, encouragement and continuous stream of exciting ideas throughout the duration of the project. Very special thanks goes to Zamir Othman who stepped in during the late stages of the project, helped turn my thoughts into coherent science and provided useful advice on a day to day basis. Thanks to Prof. Paul May and Dr. David Fermin for their helpful tips on various problems encountered during the project. I'd like to thank Piotr Wolanin for his help in taking conductivity measurements, Dr. Andrei Sarua for his advice and help in taking Raman measurements and Philip Coulter for helping me take zeta potential measurements. Thanks to Sarah Haliwell for training me on the SEM and Alex Croot, as we shared samples and some DLS data due to the finite amount of resources we had. Big thanks to the Bristol University Diamond Group that made the project year a very enjoyable experience.

## Table of Contents

|          |   |           |
|----------|---|-----------|
| <b>1</b> | <b>INTRODUCTION</b>   | <b>1</b>  |
| 1.1      | DIAMOND   | 1         |
| 1.2      | DOPING DIAMOND  | 4         |
| 1.3      | NEGATIVE ELECTRON AFFINITY (NEA)  | 7         |
| 1.4      | FIELD EMISSION  | 9         |
| 1.5      | APPLICATIONS  | 11        |
| 1.6      | WHY ELECTROSTATIC SELF-ASSEMBLY (ESA)   | 12        |
| 1.7      | PURPOSE OF STUDY  | 13        |
| <b>2</b> | <b>EXPERIMENTAL</b>   | <b>15</b> |
| 2.1      | OPTIMIZED SELF-ASSEMBLY PROCEDURE   | 16        |
| 2.2      | SURFACE TREATMENTS  | 17        |
| 2.2.1    | <i>Cleaning W Using Wet Chemistry</i>   | 17        |
| 2.2.2    | <i>Electrochemical Etch</i>   | 17        |
| 2.2.3    | <i>UV-Ozone Treatment of W</i>  | 19        |
| 2.2.4    | <i>Heat Treatment of W</i>  | 20        |
| 2.3      | BALL-MILLING BORON-DOPED DIAMOND SQUARES  | 20        |
| 2.4      | ACID WASHING DIAMOND  | 21        |
| 2.5      | POLYMER MOLECULAR WEIGHT  | 22        |
| 2.6      | RAMAN SPECTROSCOPY  | 23        |
| 2.7      | OPTICAL MICROSCOPY AND SEM  | 23        |
| 2.8      | VACUUM THERMAL-ANNEALING  | 24        |
| 2.9      | DYNAMIC LIGHT SCATTERING (DLS)  | 25        |
| 2.10     | ZETA POTENTIAL MEASUREMENTS   | 26        |
| 2.11     | 4-POINT PROBE MEASUREMENTS  | 27        |
| 2.12     | FIELD-EMISSION SETUP  | 28        |
| <b>3</b> | <b>RESULTS AND DISCUSSION</b>   | <b>30</b> |
| 3.1      | UV-RAMAN ANALYSIS   | 30        |
| 3.2      | CHARACTERIZING AND OPTIMIZING THE NOMINAL PARTICLE SIZE DISTRIBUTION OF DIAMOND | 32        |
| 3.3      | OPTIMIZING THE SIZE OF BDD PARTICLES  | 34        |
| 3.4      | CENTRIFUGED VS. NON-CENTRIFUGED SAMPLES   | 36        |
| 3.5      | SELF-ASSEMBLING BDD TO W  | 37        |
| 3.6      | IMPORTANCE OF THE OXIDE LAYER   | 37        |
| 3.7      | ENHANCING THE SURFACE OXIDE AND THE EFFECT OF PEI MOLECULAR WEIGHTS             | 39        |
| 3.8      | EFFECT OF PEI MOLECULAR WEIGHT ON NUCLEATION DENSITY                            | 41        |
| 3.9      | ASSESSING THE STABILITY OF THE DIAMOND SUSPENSION USING ZETA POTENTIALS         | 42        |
| 3.10     | FIELD EMISSION  | 44        |
| 3.11     | POST-FIELD EMISSION ANALYSIS  | 47        |
| 3.11.1   | <i>Surface Conductivity</i>   | 47        |
| 3.11.2   | <i>4-Point Probe Measurements</i>   | 48        |
| 3.12     | CHARACTERISING THE LITHIATED SAMPLE USING UV-RAMAN                              | 50        |
| 3.13     | SUMMARY   | 51        |
| <b>4</b> | <b>CONCLUSION</b>   | <b>53</b> |
| <b>5</b> | <b>FUTURE WORK</b>  | <b>55</b> |

|          |                         |           |
|----------|-------------------------|-----------|
| <b>6</b> | <b>REFERENCES .....</b> | <b>57</b> |
| <b>7</b> | <b>APPENDICES .....</b> | <b>61</b> |

## Abbreviations

BDD – Boron Doped Diamond

CVD – Chemical Vapour Deposition

DLS – Dynamic Light Scattering

LMW – Low Molecular Weight

HMW – High Molecular Weight

PEI – Polyethyleneimine

W – Tungsten

XPS- X-ray Photoelectron Spectrometry

## Symbols

$\Delta$  – Heat Treated

O<sub>3</sub> – Ozone Treated

## List of Figures

|  |    |
|--|----|
| Figure 1. Crystal structure of diamond where an infinite arrangement of $sp^3$ hybridised carbon atoms exist to give a tetrahedral lattice. Reference 1.....   | 1  |
| Figure 2. Eight allotropes of carbon. “ a) Diamond, b) Graphite, c) Lonsdaleite, d) C60 (Buckminsterfullerene or buckyball), e) C540, f) C70, g) Amorphous carbon, and h) single-walled carbon nanotube, or buckytube.” Reference 2. ....  | 1  |
| Figure 3. Extreme properties of diamond. Reference 6. ....   | 2  |
| Figure 4. Classification of diamond types. Reference 8.....  | 3  |
| Figure 5. SEM Image of polycrystalline diamond film grown via HFCVD. Reference 14. ....  | 4  |
| Figure 6. (A) Position of ground state levels of donors and acceptors relative to the conduction band minimum $E_C$ and the valence band maximum $E_V$ . $E_A$ and $E_D$ are the ionization energies of the acceptors and donors. (B) Upon ionization, electrons from valence band are excited to the acceptor level leaving behind a positively charged hole (p-type semiconductor) whereas electrons residing in impurity bands near the conduction band are excited in to it (n-type semiconductor). Reference 18. .... | 5  |
| Figure 7. Band gap diagram of (A) positive electron affinity (PEA), (B) true NEA and (C) effective NEA. Reference 40. ....   | 7  |
| Figure 8. Simplified field emission model showing the quantum mechanical tunnelling of electrons (dashed green line) under a high electric field (solid red line). Adapted from reference 55. ....   | 9  |
| Figure 9. Flowchart summarizing the steps followed to self-assemble BDD to W for field emission testing. ....  | 15 |
| Figure 10. Fabrication process showing the self-assembly of BDD to W followed by a LiO termination step. ....  | 16 |
| Figure 11. Electrochemical etching station for W.....  | 18 |
| Figure 12. Cleaning mechanism uses short wavelength UV light to breakdown contaminants. Reference 83. ....   | 19 |
| Figure 13. Thermal oxidation results in non-stoichiometric oxides forming accompanied by a colour change. Reference 84. ....   | 20 |
| Figure 14. Retsch MM 200 Mixer Mill.....   | 21 |
| Figure 15. Branched structure of PEI. Reference 93.....  | 22 |
| Figure 16. The electrostatic potential present near a negatively charged surface of spherical shape as a function of distance. Reference 103.....  | 27 |
| Figure 17. 4-point probe setup configuration. Spacing between probes 1-4 is 10 mm and between 3.33 mm between probes. Reference 104. ....  | 28 |
| Figure 18. Electron extraction under a strong electric field. Reference 106.....   | 29 |

|   |    |
|---|----|
| Figure 19. Field emission setup. A) Turbo pump B) Turbo isolation valve C) Turbo lock gate D) Atmospheric valve E) Viewing window F) Anode G) Cathode H) Power supply leads to anode. ....  | 29 |
| Figure 20. Raman spectra unwashed ball milled BDD (7 hours) calibrated against a CVD diamond reference sample (phonon peak position $1331.92\text{ cm}^{-1}$ ). Intensity of each peak is normalised by dividing its maximum intensity by the maximum intensity of diamond at $1332\text{ cm}^{-1}$ . ....  | 30 |
| Figure 21. Raman spectra of acid washed ball milled BDD (7 hours) calibrated against a CVD diamond reference sample (phonon peak position $1331.92\text{ cm}^{-1}$ ). Intensity of each peak is normalised by dividing its maximum intensity by the maximum intensity of diamond at $1332\text{ cm}^{-1}$ . ....  | 31 |
| Figure 22 Buffered BDD suspension (pH=8.0) sonicated for 4 hours using an ultrasonic water bath. ...  | 32 |
| Figure 23. Correlation plot of sonicated BDD. ....  | 33 |
| Figure 24. (A) Nanodiamond suspension after sonication for 4 hours. (B) Nanodiamond suspension after sonication for 4 hours followed by centrifugation for 60 seconds. ....   | 34 |
| Figure 25. Size distribution by intensity (A) volume and number (B and C) represented as histograms.  | 35 |
| Figure 26. Identical samples of W were at treated at $500\text{ }^{\circ}\text{C}$ with LMW PEI (0.5%) + 0.5% BDD under optimized conditions. Left image shows nanodiamond which has only been sonicated. Right image shows nanodiamond which has been centrifuged after sonication. Both samples were left to electrostatically self-assemble for 30 minutes. Particle sizes are approximate. .... | 36 |
| Figure 27. Comparison of self assembly on the native oxide layer of W (A and B) versus a freshly deposited oxide layer (C and D). ....  | 37 |
| Figure 28. SEM images of samples with adequate nucleation density for FE-testing. ....  | 39 |
| Figure 29. Nucleation densities and fractional area coverage of samples seen in Figure 28 calculated using ImageJ v1.47. All areas sampled were $10\text{ }\mu\text{m} \times 10\text{ }\mu\text{m}$ in dimension. ....   | 40 |
| Figure 30. W surface cleaned with solvents and no other treatments (A). W surface treated with ozone (atomic oxygen) or thermally oxidised (B) or both. ....  | 40 |
| Figure 31. Zeta potential measurements of sonicated and centrifuged BDD suspension. ....  | 43 |
| Figure 32. Field emission of freestanding CVD polycrystalline BDD-H showing a curve of emission current density, versus electric field, E, over an average of 10 runs. The inset shows the corresponding Fowler-Nordheim plot and the sites of emission as seen on the phosphor screen. ....  | 44 |
| Figure 33. SEM image shows W+ $\Delta$ + $\text{O}_3$ + 5% HMW PEI + 0.5% BDD + OLi. ....   | 47 |
| Figure 34. 4-point probe measurements of self-assembled samples under various conditions. ....  | 48 |
| Figure 35. Resistance and sheet resistance values of self-assembled samples under different conditions. All samples of W were a $1 \times 1\text{ cm}$ square with a thickness value of $0.15\text{ mm}$ . All samples containing BDD have been annealed. ....  | 49 |

|  |    |
|--|----|
| Figure 36. Raman spectra of lithiated sample seen in Figure 33 calibrated against a CVD diamond reference sample (phonon peak position $1331.92\text{ cm}^{-1}$ )..... | 50 |
| Figure 37. $\text{WO}_3$ Raman bands. Adapted from reference 129. ....   | 51 |

## Abstract

The chief aim of the project is to produce a field emitting device which is capable of operating at low voltages and produce a highly uniform stable emission current density ( $>10 \text{ mA cm}^{-2}$ ) using a relatively inexpensive, undemanding and reproducible fabrication technique. Field emitting arrays (FEAs) have numerous applications in micro vacuum electronics. An assortment of materials have been used to create field emitters including metal tips, carbon nanotubes (CNTs) and doped/undoped diamond with modifications to their surfaces to induce negative electron affinity (NEA) i.e. lowering the effective work function of the surface. This ultimately leads to a lower turn on voltage being required to extract electrons from the surface under an electric field. The combination of a p-type of material with a highly stable negative electron affinity (NEA) surface is present in the form of hydrogen terminated BDD (BDD-H) with a NEA value of  $-1.0 \text{ eV}$ . However it has been shown when single crystal C(100) BDD is terminated with a LiO group, a more negative NEA value is obtained due to Li theoretically existing in a shallow donor state. The project aims to investigate polycrystalline boron doped diamond (BDD) whose surface has been coated with oxygen-lithium (R-OLi) groups on tungsten metal (W). This device is the first of its kind.

The fabrication method chosen to assemble (BDD) to metal (W) was electrostatic self-assembly (ESA). The technique relies on the complementary attractions between oppositely charged surfaces to form thermodynamically stable interfacial layers. The enhancement of the metal surface oxide was found to be vital for self-assembly to occur. A finding previously unreported in literature.

Due to limited resources a 0.5% w/v stock of BDD ( $<300\text{nm}$  in diameter) was prepared in pH 8 buffer deemed to be ideal for stabilizing BDD in solution. Using an optimized self-assembly procedure, a particle coverage of  $\sim 40\%$  ( $112 \pm 25 \mu\text{m}^{-1}$ ) was achieved. It is expected repeating the self-assembly procedure will increase the nucleation density further. The assembled BDD sample was annealed under vacuum to lock diamond to the metal surface thereby making an electrical contact via an interfacial carbide layer followed by termination with OLi. The BDD sample was taken for field emission testing. For comparative purposes, BDD-H (CVD film) was tested as a reference marker which resulted in a turn on field of  $18.5 \text{ V}\mu\text{m}^{-1}$  with a maximum emission current density of  $2.5 \mu\text{Acm}^{-2}$  being observed at  $27 \text{ V}\mu\text{m}^{-1}$ . It was expected the BDD sample would give a higher emission current density at a similar turn on field due to the better nucleation density achieved using ESA as opposed to a CVD film. Upon testing, no field emission was observed from the self-assembled sample due to a drastic loss in surface diamond coverage estimated to be below 1%. The experimental data strongly link the annealing conditions not being optimized and the surface roughness of the metal as being important factors in the loss of diamond amongst a myriad of other interesting problems.



## 1

# Introduction

## 1.1 Diamond

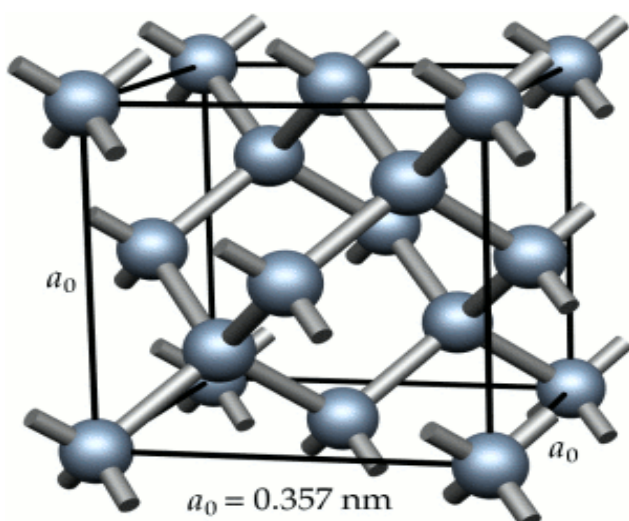


Figure 1. Crystal structure of diamond where an infinite arrangement of  $sp^3$  hybridised carbon atoms exist to give a tetrahedral lattice. Reference 1.

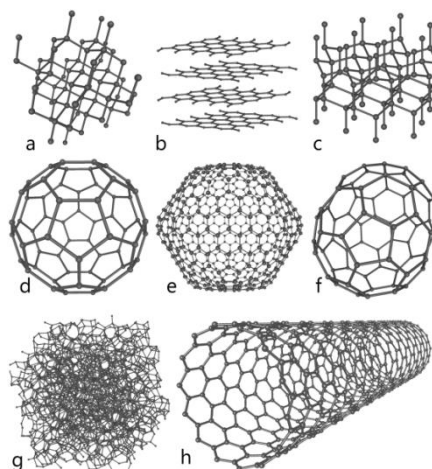


Figure 2. Eight allotropes of carbon. " a) Diamond, b) Graphite, c) Lonsdaleite, d) C60 (Buckminsterfullerene or buckyball), e) C540, f) C70, g) Amorphous carbon, and h) single-walled carbon nanotube, or buckytube." Reference 2.

Of the many allotropes of carbon that exist (Figure 2) diamond has proven to be the standout candidate in terms of the abundance of superlative properties it has, some which will be discussed in depth. The fields of research it has managed to branch out into include the medical<sup>3</sup>, energy, and micro vacuum electronics sector. The diamond structure takes on a conventional face-centered cubic

(FFC) unit cell with each carbon atom sharing 4 electrons with its closet neighbour forming a network of covalent bonds with half of the tetrahedral holes filled<sup>4</sup> (Figure 1). This arrangement leads to diamond being ranked as one of the hardest materials with a hardness index of 10 on the Mohs scale<sup>5</sup> making it ideal for use in cutting tools . Other properties which also stem from this structure have been listed in Figure 3<sup>6</sup>.

| Property   | Description                             |
|--|---|
| Extreme mechanical hardness                              | ~ 90 GPa                                |
| Highest bulk modulus                                     | $1.2 \times 10^{12}$ N/m <sup>2</sup>   |
| Lowest compressibility                                   | $8.3 \times 10^{-13}$ m <sup>2</sup> /N |
| Lowest thermal expansion coefficient at RT <sup>a)</sup> | $0.8 \times 10^{-6}$ K <sup>-1</sup>    |
| Highest thermal conductivity at RT                       | 24 W/(cm K)                             |
| Good electrical insulator                                | $R \simeq 10^{16}$ Ω cm                 |
| Semiconductor if doped                                   | $R \simeq 10-10^6$ Ω cm                 |
| Wide bandgap   | 5.47 eV at RT                           |
| Broad optical transparency                               | from deep UV to far IR                  |
| Biologically compatible                                  | nontoxic and tissue equivalent          |
| Low electron affinity                                    | even negative in some cases             |
| Very low coefficient of friction                         | ~ 0.001 in water                        |
| High resistant to wear and chemical corrosion            |   |

a) RT stands for room temperature.

**Figure 3. Extreme properties of diamond. Reference 6.**

Diamond is found and produced synthetically using various techniques. Natural diamond can be classified into 4 categories. Type I diamonds contain nitrogen as their main impurity and are the more common forms of diamond found naturally. More specifically, over 98% of the natural diamond found takes the form of type Ia diamond with a significant amount of nitrogen present<sup>7</sup>. The nitrogen present tends to cluster and aggregate in the lattice. Type Ib diamond also contains nitrogen however unlike type Ia diamond, nitrogen atoms are dispersed throughout the lattice. This less common form (<0.1%) is rare but most common synthetic diamonds take this form. In contrast, type IIa and IIb diamond contain negligible amounts of nitrogen. Type IIa are effectively free of any impurities leading to the highest thermal conductivity of any natural diamond. Type IIb contain small amounts of boron (major impurity) and are extremely rare. They are also natural semiconductors. The types have been tabulated in Figure 4.

|   | Type IA             | Type IB          | Type IIA           | Type IIB                    |
|---|---------------------|------------------|--------------------|-----------------------------|
| <b>Main impurity:</b>                         | <b>nitrogen</b>     | <b>nitrogen</b>  | <b>-</b>           | <b>boron</b>                |
| <b>Nitrogen concentration (p.p.m.):</b>       | <b>500-5000</b>     | <b>5-500</b>     | <b>&lt;100</b>     | <b>&lt;100</b>              |
| <b>Typical color:</b>                         | <b>white/yellow</b> | <b>yellow</b>    | <b>brown/white</b> | <b>blue/gray</b>            |
| <b>Electrical conductivity:</b>               | <b>insulator</b>    | <b>insulator</b> | <b>insulator</b>   | <b>p-type semiconductor</b> |
| <b>Thermal conductivity at 320K (W/m K)*:</b> | <b>530-1760</b>     | <b>1750</b>      | <b>1900</b>        | <b>1950</b>                 |
| <b>Electron Spin Resonance:</b>               | <b>no</b>           | <b>yes</b>       | <b>no</b>          | <b>no</b>                   |

\* Thermal conductivity data from Burgemeister [1978].

Figure 4. Classification of diamond types. Reference 8.

The conversion of graphite to diamond presents a large activation energy barrier resulting in the formation of metastable diamond (kinetically stable, thermodynamically unstable)<sup>9</sup>. Once formed, diamond cannot go back to graphite under standard conditions. Conditions where extreme temperatures and pressures exist are found deep in the earth's mantle where over millions of years carbonaceous deposits crystallise into diamonds eventually being brought to the surface through volcanoes<sup>10</sup>. Synthetic diamond was discovered in the early 1950's with Bundy et al. being the first group to synthetically create diamond by subjecting graphite in steel vessels to high pressure and high temperature (HPHT) conditions<sup>11</sup>. Although the technique is successful, the diamond produced is often of poor quality and controlling the diamond size can be problematic. An alternative technique known as chemical vapour deposition which is cheaper and easier to operate than HPHT came about through the work of<sup>12,13</sup> Matsumoto et al. Essentially, gas source mixtures of CH<sub>4</sub>/H<sub>2</sub> are fed into a chamber under low pressure conditions which come into contact with a heated source such as a hot filament wire (usually tungsten) at 2000 °C which provides the activation energy needed for the gases to react. Ultimately, the decomposition leads to a thin solid film of diamond being formed on the substrate. Dopants can also be introduced as gases alongside the feed mixture for diamond in a process known as in-situ doping. The concentration of the dopant can be controlled by varying its concentration in the gas phase. The technique allows a high degree of control over the film thickness and morphology such that high purity single and polycrystalline films of diamond can be grown with minimal defects and impurities. The thin films produced are quite versatile. They can be used whole or be crushed to form grits and be used in suspension for coatings on non-diamond surfaces.

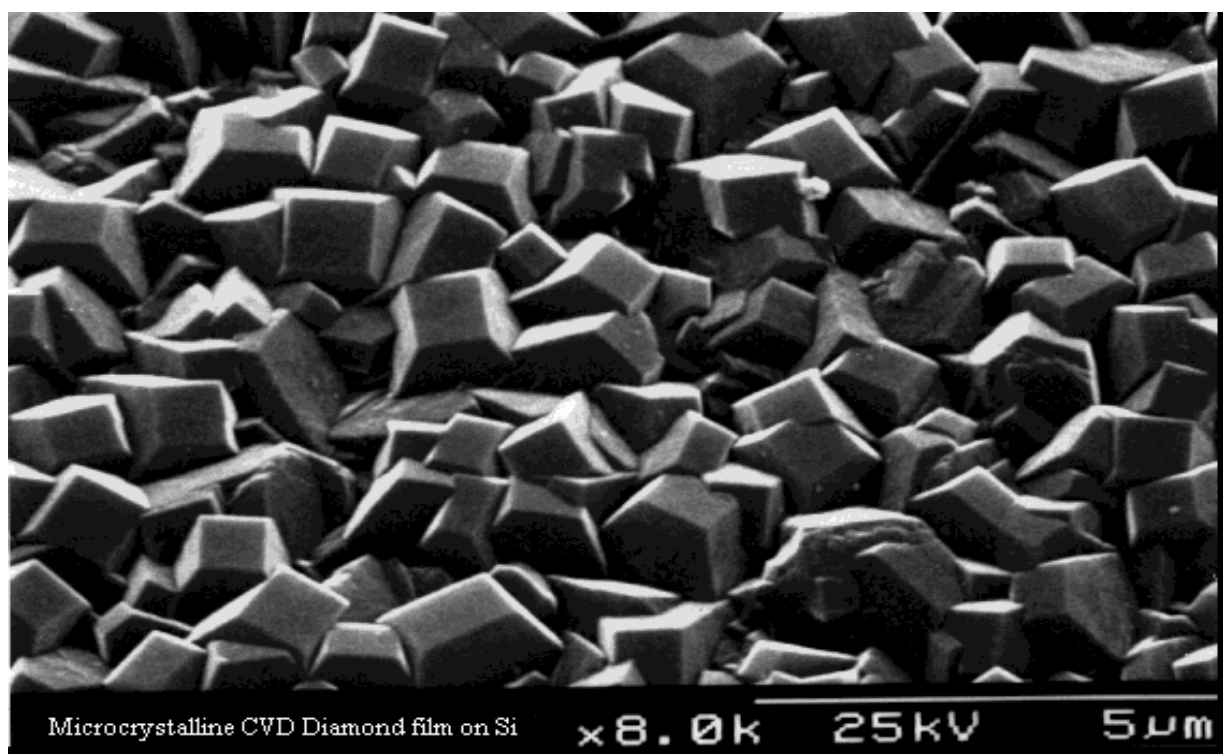


Figure 5. SEM Image of polycrystalline diamond film grown via HFCVD. Reference 14.

## 1.2 Doping Diamond

Amongst its list of extreme properties, a few select properties of diamond make it an ideal candidate to be used as a semiconductor for applications involving electronics, such as high power and frequency devices operating at high temperatures. Namely these are; a wide band gap, extremely high electric field breakdown, high carrier mobility, high saturated current velocity and the highest thermal conductivity of all materials<sup>15</sup>. The large band gap of diamond ( $5.5 \text{ eV}$ )<sup>16</sup> gives it excellent insulating properties with an electrical resistivity value exceeding  $(10^{15} \Omega\text{cm})$ <sup>17</sup> at room temperature. The large band gap makes conduction of electrons an energetically unfavourable process as a large energy is required to excite them to a conduction band. The band gap can be manipulated by the introduction of chemical impurities (dopants) thereby changing the electrical properties of diamond to that of a non-degenerate or extrinsic semiconductor. The chief aim of doping diamond is to create a low work function material which is applicable in fields requiring electron emission.

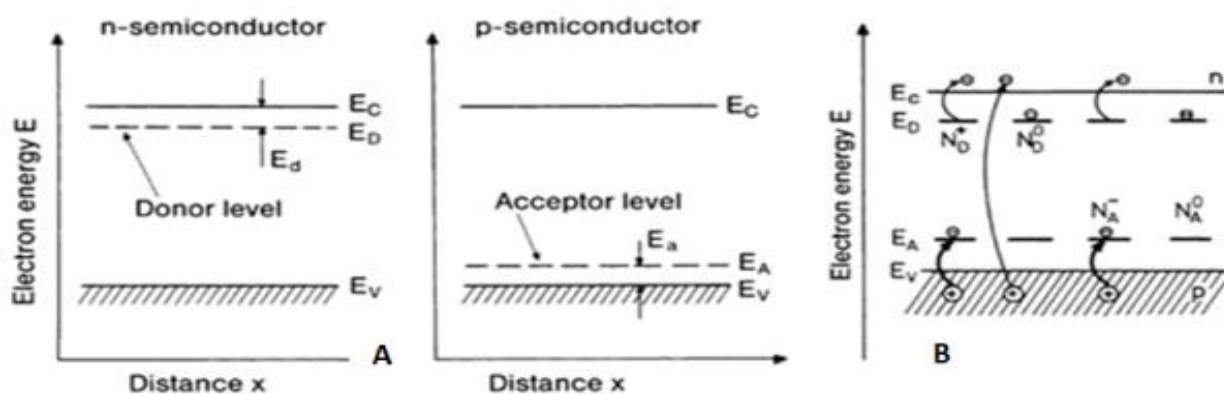


Figure 6. (A) Position of ground state levels of donors and acceptors relative to the conduction band minimum  $E_C$  and the valence band maximum  $E_V$ .  $E_A$  and  $E_D$  are the ionization energies of the acceptors and donors. (B) Upon ionization, electrons from valence band are excited to the acceptor level leaving behind a positively charged hole (p-type semiconductor) whereas electrons residing in impurity bands near the conduction band are excited in to it (n-type semiconductor). Reference 18.

The most common and reproducible form of doped diamond available is boron doped diamond (BDD). Typically, BDD is grown on substrates such as Si or  $\text{SiO}_2$  wafers via chemical vapour deposition.<sup>18</sup> Figure 6 shows the generic description of a p-type semiconductor i.e. BDD. The introduction of the dopant results in boron (B) being embedded tetrahedral in diamond lattice<sup>19</sup>. Since B has three valence electrons in its outer shell, it accepts an electron from the  $sp^3$  hybridised lattice resulting in the formation of a hole in the valence band and gaining a negative charge in the process. The holes are the majority charge carriers in p-type semiconductors. Boron is a shallow acceptor with an activation energy of  $(0.37 \text{ eV})$ <sup>16</sup> above the valence band with a dopant concentration typically at  $(10^{17} - 10^{21} \text{ cm}^{-3})$ <sup>20,21</sup>.

Conversely, n-type conductivity arises from incorporating a donor atom such as phosphorus (P) or nitrogen (N). Taking P as an example, it has 5 valence electrons present in its outer shell. When incorporated into the diamond lattice, the fifth valence electron plays no part in bonding and is thus a 'free' electron. As electrons are the majority charge carriers in n-type semiconductors, a large enough concentration of dopants results in an impurity band formation near the conduction band. Upon ionization, electrons are excited from the impurity band into the conduction band.

Potential n-type dopants in diamond which have been investigated include substitutional dopants  $\text{P}^{22,23}$ ,  $\text{N}^{24,25}$  and interstitial dopants  $\text{Li}^{26-28}$  and  $\text{Na}^{27,29}$  as well as many other group V elements. It may seem advantageous at first having an excess of electrons near the conduction band however that is not entirely true. When considering the dopant it is just as important to consider the energy level along with the solubility and the mode of incorporation. Nitrogen is readily incorporated via in-diffusion into the diamond lattice with a formation energy of  $(-3.4 \text{ eV})$  with an activation energy,  $E_a$  of  $(1.7 \text{ eV})$ <sup>22</sup>. The  $E_a$  classifies this as a deep donor meaning the number of electrons present in the conduction band at room temperature make conductivity of the doped film negligible. Calculations

performed by <sup>29</sup>Kajihara et al. show using in diffusion to introduce shallow dopants, Na-doped diamond is 0.3 eV below the conduction band along with P-doped diamond at 0.2 eV. However the formation energies show large positive values indicating solubility issues of these dopants in diamond and thus in-diffusion being an unfavourable process<sup>29</sup>. Studies report the activation energy of P-doped diamond to be in the region of (0.43-0.6 eV)<sup>22,30</sup> below the conduction band at dopant concentrations of ( $5 \times 10^{-18} \text{ cm}^{-3}$ )<sup>31</sup>.

Perhaps the most interesting of potential n-type dopants is Li. Theoretical calculations put it at (0.1 eV)<sup>29</sup> below the conduction band minimum, the shallowest of all n-type dopants. Various methods of incorporating Li into the diamond lattice to achieve n-type conductivity have been extensively tried to introduce Li into bulk diamond. So far, only limited success has been with no concrete method available yet to produce high quality Li-doped diamond let alone n-type diamond films.

Studies using ion implantation<sup>32-34</sup> have been carried out. The technique relies on brute force to implant Li into bulk diamond. As a result, this has been known to cause severe damage to the lattice which in return leads to an increase in conductivity due to the presence of an increase in defects. This may seem advantageous but the increased conductivity is due to the lattice defects and not the chemical dopant<sup>35</sup>. The damage can be repaired through annealing at high temperatures but this in turn is also problematic as Li is highly mobile at raised temperatures causing the formation of electrically inactive clusters<sup>36</sup>. Yilmaz et al. have shown using DFT calculations, Li atoms occupying interstitial tetrahedral positions in the diamond lattice form clusters with adjacent neighbours resulting in favourable formations energies of 1.88 eV (2 atom cluster) and 3.09 eV (3 atom cluster)<sup>37</sup>. Lithium concentrations of ( $1 \times 10^{19} \text{ cm}^{-3}$ ) using in-diffusion have been reported however no n-type conductivity was observed due to cluster formation<sup>38</sup>. The high mobility of Li has been linked to the formation of these clusters<sup>39</sup>. Othman et al. have suggested reducing the mobility of Li through introducing  $\text{NH}_3$  or  $\text{N}_2$  into the lattice to trap Li and thus create a co-doped material<sup>36</sup>. The work showed a less invasive way of introducing Li into diamond at a concentration of ( $5 \times 10^{19} \text{ cm}^{-3}$ ) along with a better understanding of how Li migrates throughout diamond structure. It also provides a new concept in slowing the mobility of Li with much future work to be carried out surrounding this idea.

The solubility of alkali metals such as Li and Na in diamond still remains a problem. The challenge in fabricating n-type diamond films is the introduction of a high enough concentration of dopants in the diamond lattice without damaging the structure but also ensuring the dopants remain electrically active<sup>28</sup>. Introduction of n-type dopants into bulk diamond is one way of reducing the work function of the material and hence pinning the Fermi level closer to the conduction band.

### 1.3 Negative Electron Affinity (NEA)

As electrons are being moved from the valence band to the conduction band, to leave the surface completely they must overcome the surface work function. This is known as the electron affinity,  $\chi$ . The electron affinity is the difference between the conduction band minimum (lowest electron energy state) and the vacuum level whereas the work function is defined as the difference between the Fermi and vacuum level<sup>20</sup>. The electron affinity plays a vital part in electron emission since electrons are required to escape the conduction band to go into vacuum. The surface of diamond is quite versatile such that it can be manipulated to lower the surface work function thereby contributing to the overall enhancement of electron emission. The electron affinity is independent of the Fermi level and as such is not affected by doping. The introduction of different functional groups on the diamond surfaces have been extensively investigated, primarily H and O terminated diamond. For the purposes of this project, surface terminations of BDD will be discussed.

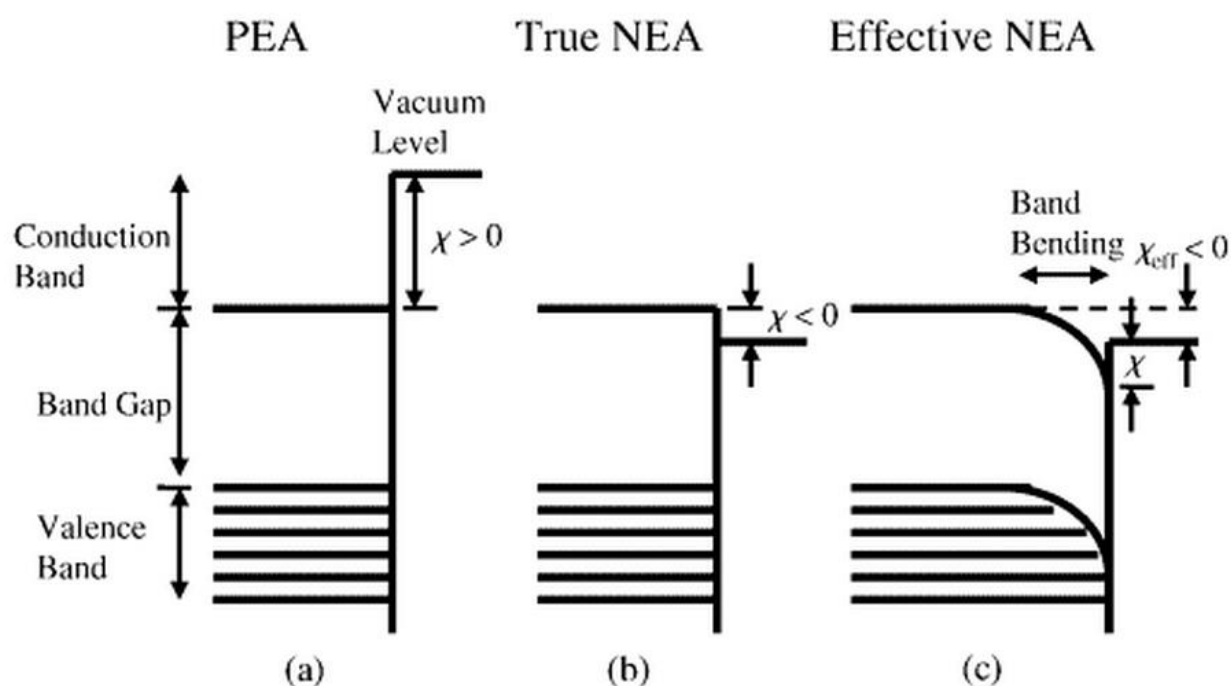


Figure 7. Band gap diagram of (A) positive electron affinity (PEA), (B) true NEA and (C) effective NEA. Reference 40.

<sup>40</sup>The electron affinity can be split into three categories PEA, true NEA and effective NEA. A PEA surface shows a barrier to electron emission with energy equal to the electron affinity and the conduction band minimum below the vacuum level i.e. oxygen terminated BDD<sup>41</sup>. A true NEA surface shows the conduction band minimum residing above the vacuum level highlighting electrons can escape into vacuum without any barrier to emission i.e. a cold cathode. A property unique to H-terminated

diamond. Under standard conditions, films of BDD grown using CVD will result in a surface naturally terminated with hydrogen. Treating the surface with hydrogen plasma to saturate the diamond surface is commonly used to terminate dangling bonds<sup>42</sup>. The termination leads to heteropolar bond formation. With carbon being the more electronegative atom when compared to hydrogen, the hydrogenation of the surface leads to BDD acquiring true NEA. Experimental NEA values in the range of (-1.0 eV) to (-1.3 eV) have been reported<sup>24,43</sup>. However a limitation must also be considered when associating this label to diamond. Only a negligible density of electrons is present in the conduction band of p-type diamond which will eventually be exhausted making it impractical to use this true NEA surface in any electronic devices<sup>44</sup>. Besides optical excitation, the only other way to introduce electrons into the conduction band would be through n-type doping along with a true NEA surface.

Effective NEA can be characterised by the introduction of alkali metals such as Cs or Li onto oxygenated diamond surfaces. This is seen by, steep downwards band bending due to the Fermi level being pinned somewhere between the diamond and metal<sup>45</sup>. The conduction band edge also exists in two regions, above and below the vacuum level. Some barrier to electron emission occurs as not all electrons in the conduction band can escape.

Numerous options exist to terminate the diamond surface with oxygen. Wet chemical oxidation treatments involving mixtures of hot concentrated acids<sup>46-48</sup>, thermal oxidation in oxygenated environments<sup>49</sup>, oxygen plasma treatments<sup>50</sup> and ozonolysis<sup>51</sup>. High resolution XPS (x-ray photoelectron spectroscopy) is typically used to identify such surface terminations through probing the electronic structures of the polycrystalline BDD powders and films. The affinity value also depends on how the oxygen bridges to the carbon atoms present on the surface e.g. ether, ketone or hydroxyl position. For example, DFT calculations performed by Petrini et al. for diamond C(100) show oxygenating the diamond surface is more energetically favourable than hydrogenating it (assuming 100% coverage). Exchange of H with ketone or ether groups is preferred over hydroxyl groups<sup>52</sup>.

Alkali metals have been suggested as promising alternatives to produce a diamond surface with not only a larger NEA value than BDD-H but also a lower work-function. Küttel et al. report an NEA value of -0.85 eV on BDD C(100) that has been coated with a CsO layer<sup>42</sup>. However cesiated surfaces are liable to degradation due to weak Cs-O bonds making them impractical due to poor surface resilience<sup>53</sup>. More recently, lithium on oxygenated diamond C(100) has been proposed as a promising candidate to produce a more stable NEA. Martin has performed *ab initio* calculations of Li adsorption energies on two common oxygenated diamond surfaces C(100) and C(111). The results shows on the C(100) surface an adsorption energy of (4.7 eV) with an NEA value of (-4.5 eV) is achieved. Similarly the C(111)

surface shows an adsorption energy of (4.37 eV) with an NEA value of (-3.97 eV)<sup>45</sup>. The work has led the development of a coating procedure which has been described in section 2.1. Initial work by Martin shows for BDD C(100) surface an experimental NEA value of (-2.1 eV) was achieved<sup>45</sup>. The project aims to achieve a similar result however with a polycrystalline film which has not been attempted before.

## 1.4 Field Emission

Before a brief review is discussed on the applications of functionalized diamond in applications which require the use of electron emission, a brief background will be provided on field emission and the factors that govern its success. Reported in 1928 by Sir Ralph Fowler and Lothar Nordheim<sup>54</sup>, field emission can be described as the emission of electrons by a bulk solid or bulk crystalline material when placed under an intense electrical field of high strength,  $F$ . Contrary to thermionic emission where thermal energy is given to electrons to overcome the potential energy barrier (work function,  $\phi_b$ ) of the metal, field emission uses a strong electric field to effectively thin the potential energy barrier thereby allowing electrons to tunnel through the potential barrier. This effect is known as quantum mechanical tunnelling.

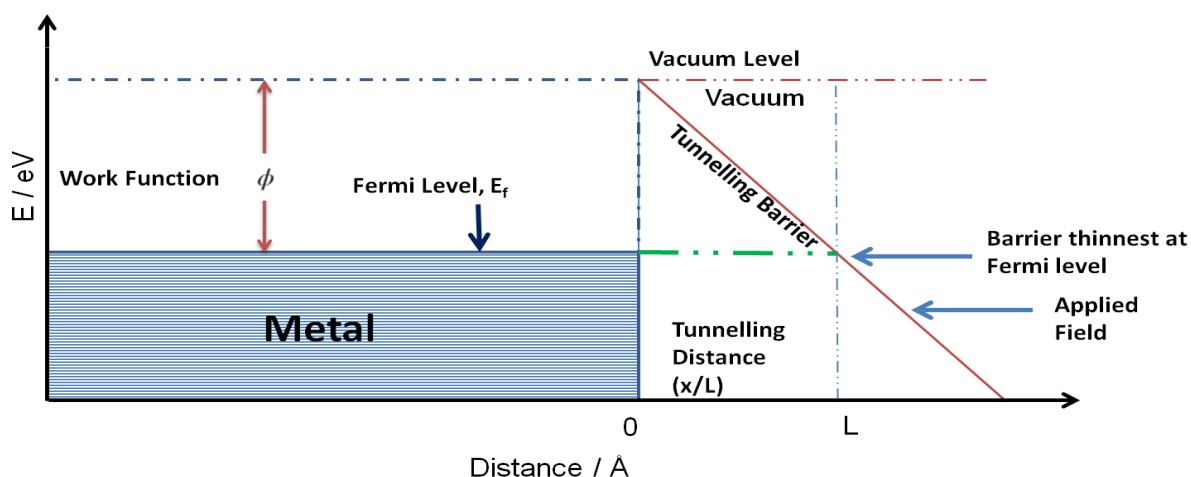


Figure 8. Simplified field emission model showing the quantum mechanical tunnelling of electrons (dashed green line) under a high electric field (solid red line). Adapted from reference 55.

The probability of an electron tunnelling through a potential barrier under an externally applied field is given in equation 1.1 which is derived from the time independent Schrödinger equation where  $F$ , is the applied electric field equal to the barrier height over the tunnelling distance ( $\phi_b/L$ ). The barrier height and width is thus a function of  $F$ . The larger the field applied, the thinner the barrier becomes at which

point electrons can escape into vacuum. For metals this is typically on the order of  $(10^9 \text{ Vm}^{-1})$ <sup>56</sup>. Given this information equation 1.2 yields the tunnelling probability which shares an exponential relationship with the barrier height to the power of 3/2 over  $\epsilon$ <sup>57</sup>. From this relationship, the tunnelling current can be derived to give the tunnelling current  $J_n$  (equation 1.2).

$$\Theta = \exp\left(-\frac{4\sqrt{2qm^*}\phi_B^{\frac{3}{2}}}{3\hbar F}\right) \quad \mathbf{1.1}$$

$$J_n = qv_R n \Theta \quad \mathbf{1.2}$$

The early model of field emission or elementary FN theory took on a number of assumptions strictly based for metal, some of which need to be relaxed in order to find exact estimates to emitting surfaces which are not purely metal. Assumptions include as stated by Forbes<sup>58</sup>; the distribution of electron energy in the metal follow Fermi-Dirac statistics, the metal is at T=0 K where all energy states are fully occupied up to the Fermi level  $E_f$ . The surface is smooth and planar with a constant uniform electric field applied across it.

A more generalized form of the FN equation which assumes pure field emission behavior relates current density from an emitter  $J_n$  ( $\text{Acm}^{-2}$ ) to the emitter work function  $\phi$  (eV) under an applied electric field  $F$  ( $\text{Vcm}^{-1}$ ) as given by equation 1.3<sup>58,59</sup>.

$$J_n = \frac{\lambda a}{\phi} F^2 \exp\left\{-\frac{\mu b \phi^{\frac{3}{2}}}{F}\right\} \quad \mathbf{1.3}$$

$$\ln\left(\frac{J_n}{F^2}\right) = \ln\left(\frac{\lambda a}{\phi}\right) - \frac{\mu b \phi^{\frac{3}{2}}}{F} \quad \mathbf{1.4}$$

Where  $a = 1.541 \times 10^{-6} \text{ A eV V}^{-2}$ ,  $b = 6.830 \times 10^9 \text{ eV}^{-3/2} \text{ Vm}^{-1}$ ,  $J_n$  is the emission current density,  $\phi$  is the work function or electron affinity of the semiconducting material,  $\lambda$  and  $\mu$  are generalized correction factors.

A more useful form of the FN equation is given in equation 1.4 where a plot of  $\ln\left(\frac{J}{F^2}\right)$  versus  $\frac{1}{F}$  yields a straight line. This is known as the FN plot and the gradient of the line plotted can be used to calculate  $\phi$ .

Along with modifying the diamond surface to induce NEA, the geometry of the emitter is also very important as it can enhance field emission and is hence appropriately known as the field enhancement factor. It is usually defined as the ratio between the local electric field at tip of the emission site and the applied macroscopic field, as described by equation 1.5<sup>60</sup>.

$$F_{local} = \beta F_{applied} \quad \mathbf{1.5}$$

The properties of an ideal field emitter can be limited to but not strictly the following physical properties which are usually reported in literature. The turn on field ( $E_{to}$ ), the electric field required to produce  $10 \mu\text{Acm}^{-2}$  and the threshold electric field ( $E_{th}$ ), the field required to produce  $10 \text{mAcm}^{-2}$ , are values typically used as a benchmark for emitting arrays used in field emission displays<sup>60,61</sup>. The values are also in units representing current emission over a defined area. The lower the electric field, (typically between  $10\text{-}100 \text{V}\mu\text{m}^{-1}$ ), the more beneficial it is to the longevity of the emitter<sup>62</sup>. Usually stability testing is carried out over prolonged periods of times (1000s of hours) to check for uniform current density.

Gomer has studied the shapes of metal field emitters noting the best emitters are usually very sharp with a very small radius of curvature which results in the local electric field being enhanced as it concentrates at the tip (emission site) allowing electrons to escape readily into vacuum as the potential barrier is thinned<sup>63</sup>. The emission of electrons under an electric field depends on the bulk properties and/or surface morphology of diamond.

## 1.5 Applications

The creation of low work function materials with an NEA surface has many uses particularly in applications such as field emission displays. Using an inkjet seeding technique Furket et al. produced lithiated diamond field emitters in the form of dot arrays ( $30 \mu\text{m}$ ) on Cr-coated glass which showed low bulk resistivity ( $0.139 \Omega\text{cm}$ ) with a threshold voltage of ( $15 \text{V}\mu\text{m}^{-1}$ ) and an emission current density of ( $7 \times 10^{-4} \text{mAcm}^{-2}$ )<sup>64</sup>. Elsewhere, Fox et al. have developed a coating procedure whereby a thin film (monolayer) of Li is deposited on oxygenated diamond, which exhibits an NEA value of ( $-3.0 \text{eV}$ )<sup>65</sup>. The patented procedure is currently being tested for use as dynodes in photomultiplier tubes and space-borne sensors<sup>66</sup>.

More recently, lithiated nanoparticles have been demonstrated as potential alternatives to photovoltaic cells which are used to capture solar energy. As well as being able to produce energies of

(1-2 Wcm<sup>-2</sup>) at temperatures well below what conventional materials use to convert thermionic energy (typically metals), the material is also capable of achieving an emission current density surpassing 10 Acm<sup>-2</sup> at a relatively low electric field of (2 Vμm<sup>-1</sup>)<sup>67</sup>. Achieving low turn on fields with high stable emission current density has been shown for single tip emitters such as carbon nanotubes (CNTs) and single crystal BDD where turn on fields as low as 1 Vμm<sup>-1</sup> have been reported however the current challenge lies in making, a field of identical emitters with all the favourable properties mentioned so far that aim to lower the overall work function of the material<sup>62</sup>. For comparative purposes, untreated nanodiamond (10-100 nm in diameter) results in no electron emission at an applied electric field of 100 Vμm<sup>-1</sup> resulting in significant electrical arcing<sup>68</sup>.

## 1.6 Why Electrostatic Self-Assembly (ESA)

The concept of using layer-by-layer (LbL) electrostatic self-assembly to fabricate thin films of materials was first demonstrated by Iler in 1966<sup>69</sup>. Following a period of inactivity, the technique resurfaced almost 3 decades following work carried out by Decher and Hong<sup>70</sup>. Since then this relatively simple yet versatile and inexpensive technique has branched into many notable areas of thin film fabrication which incorporate polyelectrolytes, proteins, metal and semiconducting substrates. Originally, the technique aimed in creating in multilayers through depositing alternative layers of oppositely charged polyelectrolytes which spontaneously undergo adsorption via electrostatic attraction on flat solid substrates<sup>71</sup>. Although electrostatic attraction acts as the fundamental driving force behind forming ordered functional structures, secondary interactions such as hydrophobicity, hydrogen bonding and van der Waals forces have also been linked in controlling the thickness of the film and hence play a part in micromanaging and balancing the attractive and repulsive forces in the system<sup>72</sup>.

Common techniques to fabricate field emitter arrays (FEA) include complex, time consuming and costly photolithographic (e-beam lithography) and etching techniques which can pose problems especially when trying to deposit thin layers of uniformly distributed diamond on the submicron scale.

Consultation of literature shows field emission tests are typically carried out using CVD films of diamond. As discussed previously, very low turn on fields have been acquired using this technique of fabricating field emitters however there also lies a problem in the scalability of using CVD films as field emitters i.e. upscaling to dimensions required for electronic devices. Before diamond films are deposited using CVD, the substrate must be prepared for growth through polishing the surface typically with nanodiamond. This process is known as seeding and consequently provides sites for

diamond growth during CVD. For micron sized samples, growth times are slow and typically range on the order of 0.5 to several  $\mu\text{m h}^{-1}$ . The surface morphology and diamond film quality will also vary. The slower the growth rate, the better the quality of the film which in turn, depends on the uniformity of seeding. For small substrates this process may be successful however when up scaling to larger sizes, it becomes impractical to use due to time, cost and the reproducibility of the film. The inherent advantage of ESA is scalability and reproducibility of the technique. By using diamond particulates (<300nm in diameter) suspended in dilute aqueous solutions, larger surface areas of substrates can be coated in multiples batches and be left to assemble for a few hours. The nucleation density of diamond present can be varied through multiple coatings. A higher density is ideal as it provides a larger surface area for electron emission. Challenges with a technique like ESA are being able to achieve a high nucleation density and a monolayer of diamond on the surface.

For the purposes of this project, BDD was chosen along with a cationic polymer PEI, to form a thin monolayer on W whose native oxide layer gives it a negative charge. An intermediate layer is needed upon which diamond can adsorb to. Any direct interaction between BDD and the metal is too weak to sustain a film type layer. Following successful assembly since W is a carbide forming metal, upon annealing carbide bond formation between metal and diamond takes place thus establishing an electrical contact. Characterisation studies involving zeta potentials (section 2.10, 3.9) of both W and BDD show a pH window of 8 where the fabrication of a thermodynamically stable device is possible. The procedure has been outlined in more detail in section 2.1. Systems using dilute aqueous polymer on flat, smooth surfaces have seen relative success particularly when assembling nanodiamond on Si or  $\text{SiO}_2$  wafers<sup>73,74</sup>. One of the main advantages and also disadvantages of using this system is that there are many variables that must be controlled and optimized to achieve the desired effect. These factors have been discussed in depth, later on in the project.

## 1.7 Purpose of Study

This investigation aims to produce a method to fabricate a monolayer of boron doped diamond on W terminated with oxygen lithium groups to ultimately produce a low work function surface, which is capable of emitting electrons under an electric field. The fabricated device will be an analogue of the device filed in patent US20120244281 A1 as it incorporates a p-type semiconductor, namely, polycrystalline boron doped diamond. The surface of diamond is quite versatile and can be functionalized to induce negative electron affinity (NEA) whereby electrons residing in the acceptor levels above the valence band maximum can be excited into the conduction band which lies above the

vacuum level and thus can enter vacuum (upon an electric field being applied) without coming across a large energy barrier i.e. cold cathode. In practice, such devices can be incorporated into arrays for the use in micro vacuum electronic such as field emitter displays (FEDs) and scanning electron microscopes (SEMs) both of which use an electric field to extract electrons from the surface. Analogues of the device proposed have seen use in thermionic solar energy converters in the form of dynodes and other micro vacuum electronic devices.

The device will be assessed for its turn on field and emission current density in a custom made field emission kit under vacuum conditions ( $10^{-6}$  Torr). It will be compared against a reference sample of free standing industrial grade polycrystalline H-terminated (BDD). Present problems which have plagued field emitter arrays from further progression are; uniform current emission over large surface areas and emission current stability, both of which depend on the properties of the emitter. Inherently, any perturbations in the size and shape of the emitter can have profound effects on the emission current observed i.e. change in work function. In summary, fabricating devices which are highly uniform in their geometry and density as well as possessing low work functions is the motivation behind the current research taking place in field emission. The drive to create inexpensive low power energy efficient devices will see many different areas of research heavily investing in research and development. The micro vacuum electronics sector is seeing huge growth both commercially and scientifically, with the semiconductor industry currently worth €300 billion<sup>75</sup>.

## 2

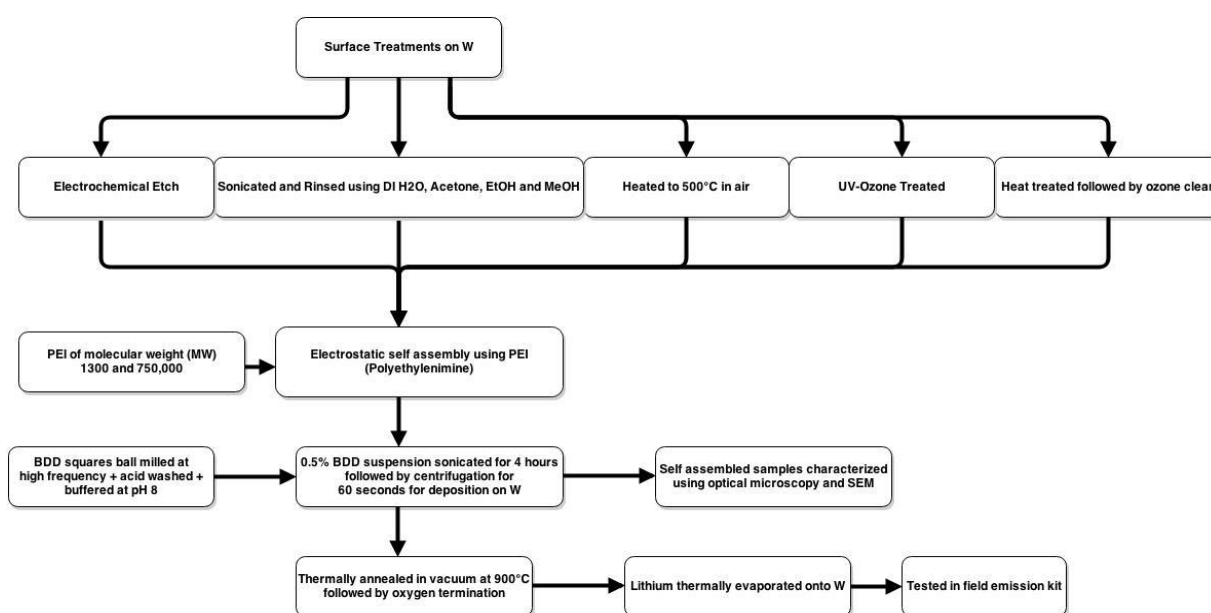
E  
xperimental

Figure 9. Flowchart summarizing the steps followed to self-assemble BDD to W for field emission testing.

The self-assembly route of this experimental was constructed due the failure of an optimized method developed by Dr. Fox and E.Tofts for the self-assembly of undoped nanodiamond on Si substrates<sup>27</sup>. The method was not transferable when tried with BDD on W. Before any lithium coatings could be applied to diamond, it was important to have a W surface with sufficient diamond coverage. The failure provided an opportunity to develop a completely novel method to electrostatically self-assemble BDD to W.

## 2.1 Optimized Self-Assembly Procedure

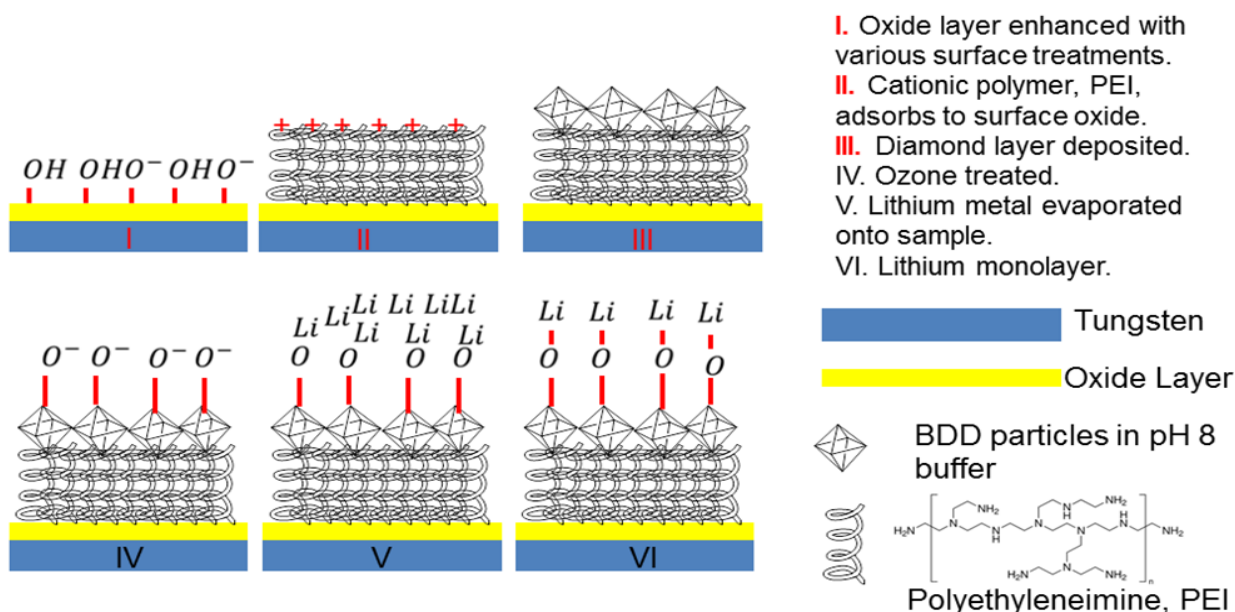


Figure 10. Fabrication process showing the self-assembly of BDD to W followed by a LiO termination step.

Figure 10 shows the optimized route of self-assembly which was constructed to give the best possible nucleation density of BDD on W. The steps which have been highlighted in red are the main focus of this project and will be explored in depth in the results and discussion. Although the process has been simplified into six steps, there are many variables present, all of which could not be controlled and optimized.

(Step I) Following the cleaning steps outlined in section 2.2, the tungsten oxide layer was enhanced using heat treatment (heated at 500 °C) and/or UVO cleaning (ozone treatment). (Step II) The negatively charged W was immersed in an aqueous solution of PEI (high or low molecular weight) thereby enabling the electrostatic attachment of PEI to W. (Step III) The PEI coated substrate was immersed in a centrifuged suspension of BDD for 30 minutes. It was then washed and dried with ethanol and water. Re-immersion of PEI coated W in BDD suspension can be applied to increase nucleation density of diamond present on the surface. The sample was then thermally annealed under vacuum conditions at 900 °C to consolidate the diamond layer. (Step IV) The BDD surface was terminated with negatively charged oxygen groups using the UVO cleaner for 30 minutes<sup>76</sup>. (Steps V and VI) Lithium metal was thermally evaporated onto the oxygen terminated surface using physical vapour deposition followed by a wash step using IPA and DI water to remove excess lithium from the surface to achieve a thin monolayer coating<sup>76</sup>.

## 2.2 Surface Treatments

As electrostatic self-assembly is the preferred method to deposit a thin uniform layer of diamond onto the surface, it is essential the surface is treated in a manner which minimizes contaminants such as chemisorbed organic and inorganic species. The following type of treatments suggested also clean the metal surface at various depths.

### 2.2.1 Cleaning W Using Wet Chemistry

W being a refractory metal is resistant to air and oxygen as well as most chemicals at room temperature. Cleaning W involves utilises some of the following chemicals as reported by the CRC handbook of metal etchants<sup>77</sup>; concentrated H<sub>2</sub>SO<sub>4</sub> acid at hot temperatures, chromic acid, mixtures containing KNO<sub>3</sub> and HF and formic acid and hydrogen peroxide. Due to the nature of these chemicals, the metal is usually attacked albeit very slowly. As a result, there is a high possibility in multilayer films of polymer being formed as the surface morphology is uneven.

A more subtle and non-invasive technique has been successfully demonstrated by Tofts who extensively investigated the correlation between cleaning the surface of Si with different solvents and the nucleation density of nanodiamond. Tofts recommended the following method to achieve the best nucleation density, "Using nitrile gloves and plastic tweezers to minimise damage, rinse a single Si substrate (1 cm<sup>2</sup>) with deionised water, acetone, ethanol and methanol sequentially, drying with N<sub>2</sub> between each rinse"<sup>78</sup>. Tofts deemed the method sufficient enough to remove any organic and oily residues such as fingerprints. Each and every W substrate was treated with this method followed by a final rinse with water before being dried. This step acts as a pre-cleaning step prior to any further treatment.

### 2.2.2 Electrochemical Etch

Electrochemical etching has seen success in scanning tunnelling microscopy (STM) and spectroscopy (STS) where fine 'needle like' W tips which are a few atoms thick are used to image surfaces at the atomic level as well as map local density of electrons. Provided the tip is placed close enough to the surface usually a few nanometres, quantum tunnelling of electrons can occur across a potential

barrier. Tip purity is essential and so with an oxide layer being present on the tip can perturb the junction between the surface and the tip thus increasing the barrier to tunnelling and introducing resistance<sup>79,80</sup>. Hockett et al. proposed using concentrated HF acid to dissolve the oxide layer while leaving the metal surface intact<sup>79</sup>. Due to safety reasons this was not possible to do with W so another approach was used.

The electrochemical etch was used to provide a fresh bare W surface which was pure of any chemisorbed and metallic species as well the oxide. In theory, this will provide the cleanest surface as the cleaning is occurring at an atomic level. The surface when re-exposed to air would form its native oxide layer known to be roughly 10 Å thick<sup>81</sup>. 30% (w/v) KOH was used as an etchant for removing tungsten oxide<sup>77</sup>. A simple circuit similar to the one created by Ibe et al. was used as an electrochemical etching station<sup>80</sup>. A stainless steel rod acted as the cathode and the W square as the anode with a battery pack attached. A potential difference of 4.83 V measured using a Fluke multimeter was applied to the metal for approximately 1 minute. This was deemed sufficient enough for the dissolution of W to tungstate ions. The process is summarized by the following equations.

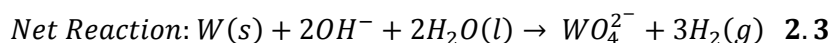
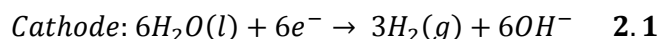


Figure 11. Electrochemical etching station for W.

### 2.2.3 UV-Ozone Treatment of W

J.R.Vig carried out an extensive study on treating metal with UV/Ozone lamps as a means to produce near 'atomically clean substrates'<sup>82</sup>. The study stresses the importance of pre cleaning the metal to remove the majority of surface contaminants before any further treatment can occur. Vig showed using a mercury arc lamp, the metal is exposed to high energy short wavelength light (90% at 253.7 nm) for very short durations (<2 minutes). The wavelength is sufficient for the dissociation of ozone to produce atomic oxygen and hydrocarbons followed by desorption of contaminants as CO<sub>2</sub> and H<sub>2</sub>O. The surface was tested for its hydrophobicity using a simple test where steam was run over the surface and as it condensed a thin, uniform and continuous film of water was observed. Any contaminants would appear in the form of a break in the film. The study also showed prolonged exposure to short wavelengths results in the metal corroding. As the process is being carried out in the presence of air, volatiles such as NO<sub>x</sub> and SO<sub>x</sub> can combine with residual water to form the acid forms of the oxides. However most importantly, as atomic oxygen is a product of the dissociation of O<sub>3</sub>, the powerful oxidizing agent is capable of enhancing the oxide layer at durations exceeding 10 minutes. This change in the surface chemistry proves to be highly influential to the self-assembly process as discussed in section 3.6.

A UVO-Cleaner<sup>®</sup> 42-220A (Jelight Co.Ltd) was primarily used to clean the surface of W but due to a treatment time of 30 minutes it also oxidised the surface.

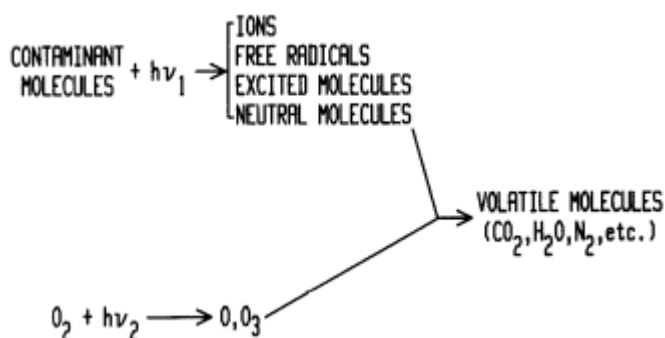


Figure 12. Cleaning mechanism uses short wavelength UV light to breakdown contaminants. Reference 83.

## 2.2.4 Heat Treatment of W

A Paragon SC2 Kiln with an Orton Sentry digital programmer was used to heat treat W in air at 500 °C. Thermally treating W was used as an alternative method to clean the surface of W of any contaminants as mentioned previously. Thermally treating W leads to the thermal oxidation of W which is accompanied by a colour change as observed by Ivanov et al. and Bonnet et al. at temperatures exceeding 400 °C and well into the 1000 °C mark<sup>84,85</sup>. A colour change during the treatment was observed confirming the presence of an oxide (see appendix).

| Stoichiometric formula                       | O/W ratio | Color          |
|--|-----------|----------------|
| WO <sub>3</sub> ( $\alpha$ )                 | 3.00      | Yellow         |
| W <sub>20</sub> O <sub>58</sub> ( $\beta$ )  | 2.90      | Blue-violet    |
| W <sub>18</sub> O <sub>49</sub> ( $\gamma$ ) | 2.72      | Reddish-violet |
| WO <sub>2</sub> ( $\delta$ )                 | 2.00      | Brown          |

Figure 13. Thermal oxidation results in non-stoichiometric oxides forming accompanied by a colour change. Reference 84.

The oxidation state of W is difficult to define as it has been modified through the mentioned treatments which oxidise it. Naturally occurring oxide forms are WO<sub>3</sub> (yellow crystalline powder) and the rarer form WO<sub>2</sub>. Mixed valence species of tungsten oxides are also possible since the metal possesses many stable oxidation states particularly in the region of +4 to +6 with various non-stoichiometric oxides such as W<sub>20</sub>O<sub>58</sub>, W<sub>18</sub>O<sub>49</sub> known to exist<sup>86,87,85</sup>. For clarity purposes, tungsten will be mentioned as W throughout the project even though it strictly exists as an oxide.

## 2.3 Ball-Milling Boron-Doped Diamond Squares

Three free standing polycrystalline industrial grade BDD squares were ordered from Element Six (E6). A Retsch MM 200 Mixer Mill (Retsch GmbH and Co., Haan, Germany) was used to mill the BDD squares to a fine polycrystalline powder in the targeted region of  $\leq 300$  nm using stainless steel balls. The mixer mill uses the high energy motion of the balls to grind diamond to smaller sizes through friction and

pulverisation while the canister is repeatedly oscillating in a horizontal motion. The squares were milled at 20 Hz for several hours.



Figure 14. Retsch MM 200 Mixer Mill.

The obvious disadvantages to this method include cross contamination from the balls to the material being milled and no size control leading to a non-uniform distribution of diamond. To minimize contamination, the balls were always washed with solvents; ethanol, methanol and acetone. They were then sonicated with DI water for approximately 5 minutes to further remove any contaminants. Similarly, the same processes were carried out with the stainless steel canisters. Once dried, the BDD squares were loaded into the canisters and milled for several hours. The now, fine powder was carefully extracted from the canister and was taken to be acid washed.

## 2.4 Acid Washing Diamond

An assortment of various mixtures of acids exist for washing diamond including aqua regia, chromic acids and nitric acids all intending to leave the surface pristine of any contaminants and the surface of diamond terminated with oxygen<sup>88,89</sup>. BDD powder was boiled under reflux at 220 °C in concentrated  $\text{KNO}_3$  with  $\text{H}_2\text{SO}_4$  to remove any non-diamond carbon, diamond like carbon and residual graphitic content<sup>90,91</sup>. UV-Raman analysis was later used to confirm the quality of the BDD (section 3.1).

The reaction has been described by equations 2.4 and 2.5.



As the diamond was suspended in a strongly acidic solution, it was neutralised with DI water until a solution of pH 5-6 was reached. A 0.1 M buffer containing  $KH_2PO_4$  and KOH was prepared and added to the BDD solution to achieve a pH of approximately 8. The pH of the medium was adjusted by adding small amounts KOH. This type of treatment also leads to the surface of diamond being oxidised<sup>76,92</sup>. The oxidised diamond particles are predicted to suspend much better in basic solutions, forming agglomerate free suspensions in which each particle can acquire a negative charge. This facilitates single particles of BDD linking to the positive ends of the PEI molecules to form a particle layer of diamond on the surface of W. Due to the amount of raw materials only a 1% w/v BDD solution could be prepared which was used as stock. This was then diluted to various other concentrations.

## 2.5 Polymer Molecular Weight

The polymer chosen for self-assembly was PEI (polyethyleneimine) at molecular weights,  $M_w$ , 1300 and 750,000 in aqueous solutions (50 wt. % in  $H_2O$ ). The branched chain polymer undergoes solvation effects in aqueous solution thus all nitrogen atoms gain a positive charge as a lone pair of electrons are available for H-bonding. The surface of W also carries a negative charge in aqueous solution (see section 3.6) therefore through strong electrostatic attractions; the cationic polymer is able to form an hydrogen bond with the surface.

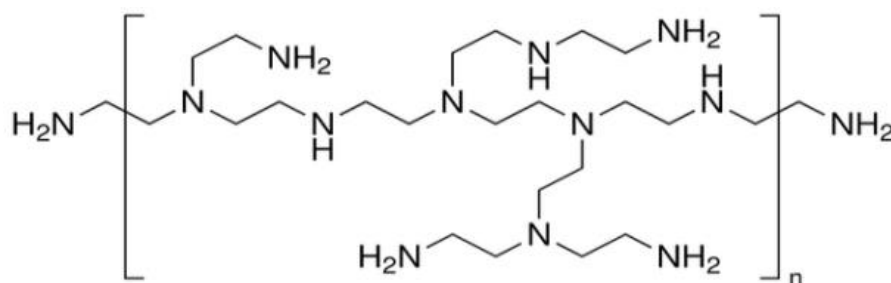


Figure 15. Branched structure of PEI. Reference 93.

## 2.6 Raman Spectroscopy

Raman spectroscopy is a non-destructive technique which involves using a monochromatic light source such as UV, visible or near infrared to illuminate a sample with photons of energy,  $E$ . The sample will interact with the photons to typically give two types of scattering. Rayleigh scattering (elastic scattering) is the result of emission of a photon with energy (frequency and wavelength) identical to that being emitted by the laser source. Large fractions of photons incident on the sample are typically scattered in this way and are optically filtered out. However a small remainder will undergo inelastic scattering where the sample will emit photons of energy lower (Stokes scattering) or higher (anti-Stokes scattering) than the photons from the laser source (Rayleigh photons). The energy (frequency) differences of these photons at their respective vibrational states can be measured to give Raman spectra. Much like IR spectroscopy, Raman spectroscopy can provide a fingerprint region with Raman shifts unique to each material. The peaks and bands observed can provide information on the vibrational modes of the sample.

A Renishaw RM2000 NUV micro-Raman spectrometer was used equipped with Peltier cooled CCD array. The excitation source was a 325 nm line from a Kimmon He-Cd laser which was focused on the sample using a 40x UV microscope lens in a spot roughly 2  $\mu\text{m}$  in diameter. The maximum output of the laser at 100% is 4 mW. The spectrum was recorded in backscattering geometry at 25 °C. The spectral resolution of the spectrometer is a 4  $\text{cm}^{-1}$  using a 3600 l/mm grating. The spectrometer was calibrated using a CVD bulk diamond reference sample (phonon peak position 1332.3  $\text{cm}^{-1}$ ).

## 2.7 Optical Microscopy and SEM

Once assembled, the samples were screened through a set of two microscopes to confirm whether or not the self-assembly was successful to an extent using various different surface treatments as explained previously. This would be done through the following; an optical microscope (Zeiss Axiolab) which provided magnification up to x100 was used to assess the distribution of BDD across the surface of W before being taken to the scanning electron microscopy (SEM) for further analysis.

Following on from optical microscopy, the JEOL JSM 6330F, an ultra-high vacuum (SEM) equipped with a field emission gun (FEG-SEM) was used to further probe the self-assembled samples. Properties explored included; surface morphology, crystal structure and orientations, nucleation density, particle

size, uniformity and surface coverage. An accelerating voltage of 10 kV with an electron beam current of 12.5  $\mu\text{A}$  was used.

The SEM uses a beam of highly energetic electrons between the ranges of (0.5 – 30 kV) which is focused on to the sample using lenses. The incident electron beam on the sample causes a number of electrons of varying energy to be emitted back from the surface, primarily secondary electrons. An Everhardt-Thornley detector captures the corresponding electrons whose energies are converted for viewing on a cathode ray tube (CRT) screen. The SEM is capable of magnifications of up to x500,000 at resolutions below <10 nm.

## 2.8 Vacuum Thermal-Annealing

W is an ideal material for the annealing of diamond to its surface. It belongs in a class of metals known as refractory metals which quite readily form carbide bonds under conditions such as high temperature. BDD deposited on the surface simply held through electrostatic attractions is unlikely to be conductive especially since the conduction model being used to explain the emission of electrons from the sample is a triple junction model between the metal diamond and the vacuum. A conductive layer in the form of carbide bonds is needed to be able to form a junction between the substrate and the diamond. It also aids in relieving some stress between the diamond and W interface<sup>94</sup>. The PEI essentially acts like a scaffold layer holding the BDD particles in place prior to annealing. At this stage, the polymer decomposes as the melting point of PEI is 250 °C<sup>95</sup>.

Experiments carried out by Goeting et al. suggested films of BDD which were deposited on W substrates using a hot filament reactor were thermally stable at annealing temperatures of approximately 1200 °C in vacuum and 700 °C in air<sup>96</sup>. Finding the right temperature to anneal BDD to W was done through subjecting the samples to a variety of annealing times and temperatures. Through trial and error, the following sets of conditions described indicate the best conditions for annealing diamond at this moment in time.

Once samples were screened optically, they were then vacuum annealed under high vacuum conditions at 900 °C for 2-3 minutes. The purpose of this was to remove any contaminants through intense heating and secondly to consolidate the diamond layer on to the metal surface by creating an interfacial carbide layer. The resistivity of WC is known to be relatively low ( $2 \times 10^{-7} \Omega\text{m}$ )<sup>97,98</sup> making it an ideal material for electrostatic self-assembly.

## 2.9 Dynamic Light Scattering (DLS)

An important aspect of the self-assembly process was to attain a size distribution of the particle sizes. For reasons stated previously small grains are ideal for the purpose of field emission as they provide a larger area for electron emission. Although SEM images can be used with specialist software to approximate particle sizes, it only accounts for fractional areas typically 10-100  $\mu\text{m}^2$  in area. The only way to obtain a representative value would be taking multiple images over a series of sites which is time consuming. DLS is a routine technique used in measuring particle sizes in solution; it is relatively easy to use but most importantly also a rapid way of attaining particle size information. DLS measurements were taken with a Malvern Zetasizer S90 over a series of runs at 25 °C.

The concept behind DLS is as follows. A small particle being illuminated by a laser source will typically scatter light in all directions resulting in a bright spot being observed should it be viewed optically. If this system is replaced for many particles, a stationary 'speckle' pattern is observed whereby both bright and dark spots are observed due to constructive/destructive wave interference. If the system is now modelled as many particles in a suspension, the particles are no longer stationary hence neither is the pattern. As the particles undergo Brownian motion (the random movement of particles in suspension as a result of collisions with solvent molecules), large particles will move slower than smaller particles causing fluctuations seen in the intensity of the bright and dark spots i.e. scattered light. If the intensity in fluctuations were to be plotted as a function of time, it would show smaller particles fluctuate more rapidly than large ones. It is this inherent property of the system, the rate of intensity fluctuation which is measured<sup>99</sup>. The size and speed of the particles is related through equation 2.6 the Stokes-Einstein equation and can be used to calculate  $D_H$ , the hydrodynamic diameter.

$$D_H = \frac{kT}{3\pi\eta D_t} \quad 2.6$$

Where  $D_H$  is the hydrodynamic diameter,  $k$  the Boltzmann's constant,  $T$  is the temperature,  $\eta$  is the dynamic viscosity and  $D_t$  is the translational diffusion coefficient. Particles are generally non-spherical, dynamic and undergo solvation effects. In reality, the size value being reported takes into account hydration and size effects (hydrodynamic) which incorporates diffusional properties of the particle<sup>100</sup>. A small error is thus associated with the actual size of the particle. The equation is accurate in modelling a hard sphere.

A typical DLS system involves a quartz cuvette containing the suspension being illuminated by a laser source. The scattered light is recorded and measured by a detector placed perpendicular to the cell. The more concentrated the solution is, the more the light is scattered. Information sourced from the detector is passed to a digital correlator which calculates the rate at which the scattering signal is fluctuating in conjunction with computer software which derives size information of the particles and gives a size distribution by intensity<sup>101</sup>.

## 2.10 Zeta potential measurements

The diamond particles being used in experiments have undergone wet chemical oxidation i.e. acid washed and have been suspended in a buffer solution of pH 8. In theory, the particle surface is negatively charged. Stabilising the solution through electrostatic repulsions (buffer solution) was chosen as opposed to steric repulsion due to the attractive option of being able to tweak the ion concentration to maximise repulsion and hence the stability of the system. This also means the system solely relies on the negative surface charge of the diamond to keep the suspension in a dispersive state (repulsive interactions dominating). Although using a pH probe confirms the pH of the solution, measuring the zeta potential can be used in understanding the stability of the dispersed particles in suspension as well as the surface charge. The magnitude of the zeta potential can be used to understand the stability of a suspension as it is a measure of magnitude of the attractive and repulsive forces. The general boundary used to dictate the stability (particles in a disperse state) of a suspension is any value above  $\pm 25$  mV. A value between  $\pm 40$  and 60 mV indicates good stability with higher values indicating excellent stability<sup>102</sup>.

The zeta potential ( $\zeta$ ) cannot be measured directly but rather it is a relationship derived from measuring the velocity of particles in a suspension (electrophoretic mobility) when in a d.c. electric field. The larger the charge on the particle, the faster the particle travels. The charge of the particle in solution does not explicitly exist as a negative charge as it counterbalanced by ions of the opposite charge.

Figure 16 describes the electrostatic potential present on the particle surface as a function of distance (nm). Assuming the particle is negatively charged and spherical in shape, the graph shows the potential near the surface varies in two ways. At first, a linear decrease is observed in the potential signifying the junction between the surface and the surrounding counter ions which are bound to the surface (Stern layer). As we move away from the surface, the stern layer spreads out into the bulk of the solution

where the line between the charge present on the surface and the surrounding solution becomes blurred. As the applied electric field pulls the particle and the counter ions in opposite directions; naturally, some counter ions will move with the particle (Stern layer) thus the charge measured is the 'nett' charge. The point at which this is measured is shown in Figure 16 as a dotted line i.e. the boundary between the stern and diffuse layer more formally known as the slipping plane. The electrophoretic mobility of the particles is related to the zeta potential and can be used to calculate a value<sup>103</sup>.

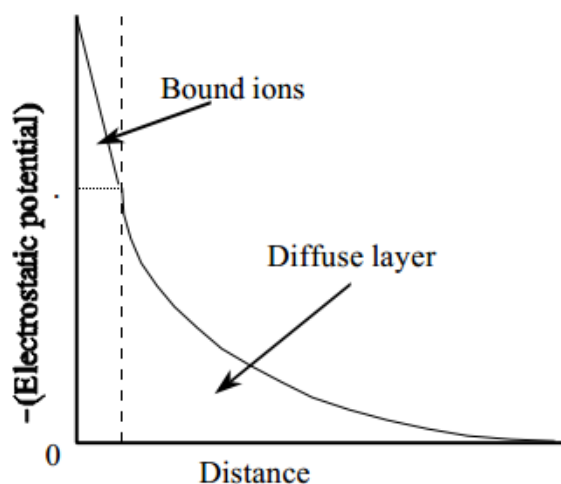


Figure 16. The electrostatic potential present near a negatively charged surface of spherical shape as a function of distance. Reference 103.

Zeta measurements were taken with a Malvern Zetasizer Nano Z over a series of 5 runs with 75 measurements taken per run to maximise reproducibility at 25 °C.

### 2.11 4-Point Probe Measurements

A 4-point probe was used to investigate whether the various fabrication steps affected the resistance values of self-assembled BDD particles on W. The 4-point probe separates the contacts that are used to deliver current and measure voltage as opposed to a 2-point probe which uses the same contacts. Current is sent through the two outer probes and the voltage is measured through the two inner probes as seen in Figure 17. The outcome is a voltage drop (voltage lost due to internal impedance of wires) along with negligible measurement error in the voltage sensing probes as current no longer flows through these probes.

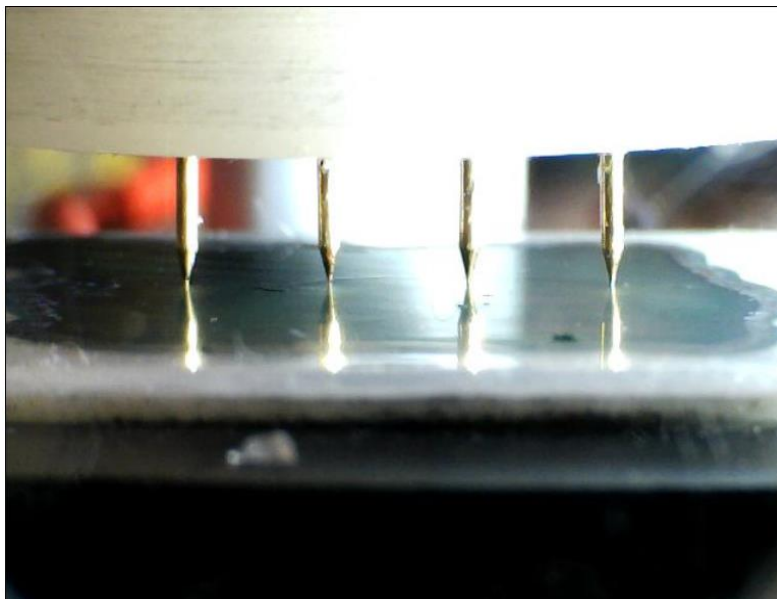


Figure 17. 4-point probe setup configuration. Spacing between probes 1-4 is 10 mm and between 3.33 mm between probes. Reference 104.

A Keithley digital source meter (model 2401) was used to source current from 0 A to 1.055 A (compliance limit). The current was swept across the sample and the resultant voltage was measured. The sheet resistance of the material was calculated from the value of resistance derived by Ohms law depicted in equation 2.6.

$$R = \frac{\rho W}{Lt} = R_s \frac{W}{L} \quad 2.6$$

Where R is resistance ( $\Omega$ ),  $\rho$  is resistivity ( $\Omega\text{m}$ ) and  $R_s$  is sheet resistance ( $\Omega\text{sq}^{-1}$ ). Since  $W=L$  the resistance is equal to sheet resistance.

## 2.12 Field-Emission setup

The sample acted as the cathode, and a phosphor screen (Ce-YAG) coated with a thin layer of SnO acted as the anode. The effective area, A ( $0.0757\text{ cm}^2$ ) was the area of the sample which was exposed to the phosphor screen. A Brandenburg power supply unit applied voltage between 0 – 3.5 kV across the sample. The overall distance, d between the cathode and anode was  $674\text{ }\mu\text{m}$ . Applying the electric field causes the extraction of electrons from the cathode. This has been described in Figure 18. Before any measurements were plotted, the sample was conditioned over a series of runs by burning off any adsorbed contaminants which may have been introduced during the assembly stage as they can influence the work function of the material and potentially damage to the emitter surface<sup>105</sup>.

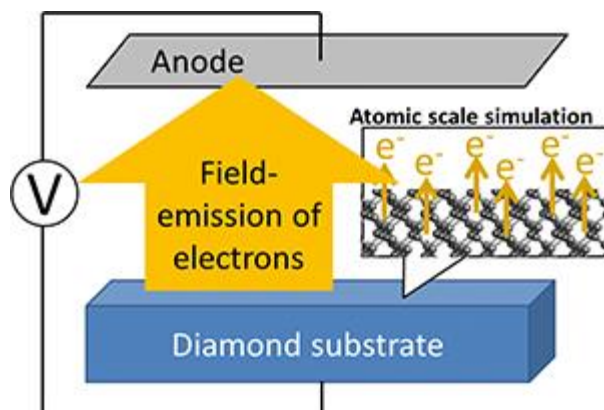


Figure 18. Electron extraction under a strong electric field. Reference 106.

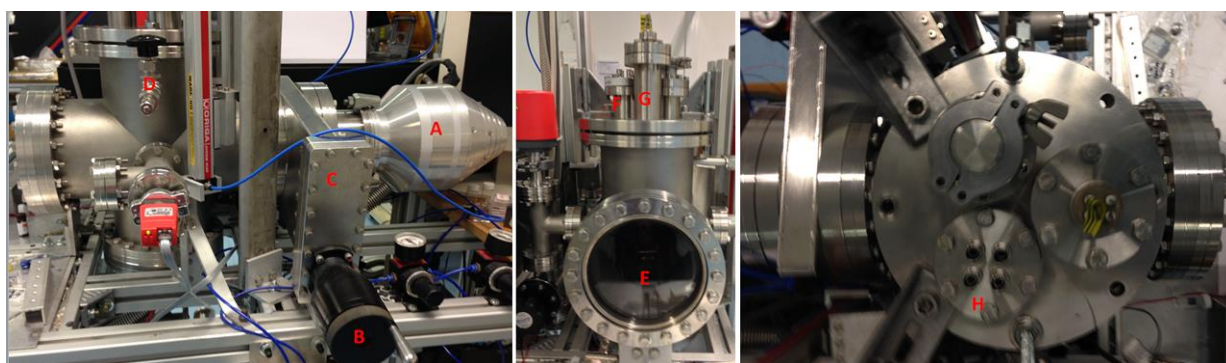


Figure 19. Field emission setup. A) Turbo pump B) Turbo isolation valve C) Turbo lock gate D) Atmospheric valve E) Viewing window F) Anode G) Cathode H) Power supply leads to anode.

## 3

# R

esults and 

# D

iscussion

## 3.1 UV-Raman analysis

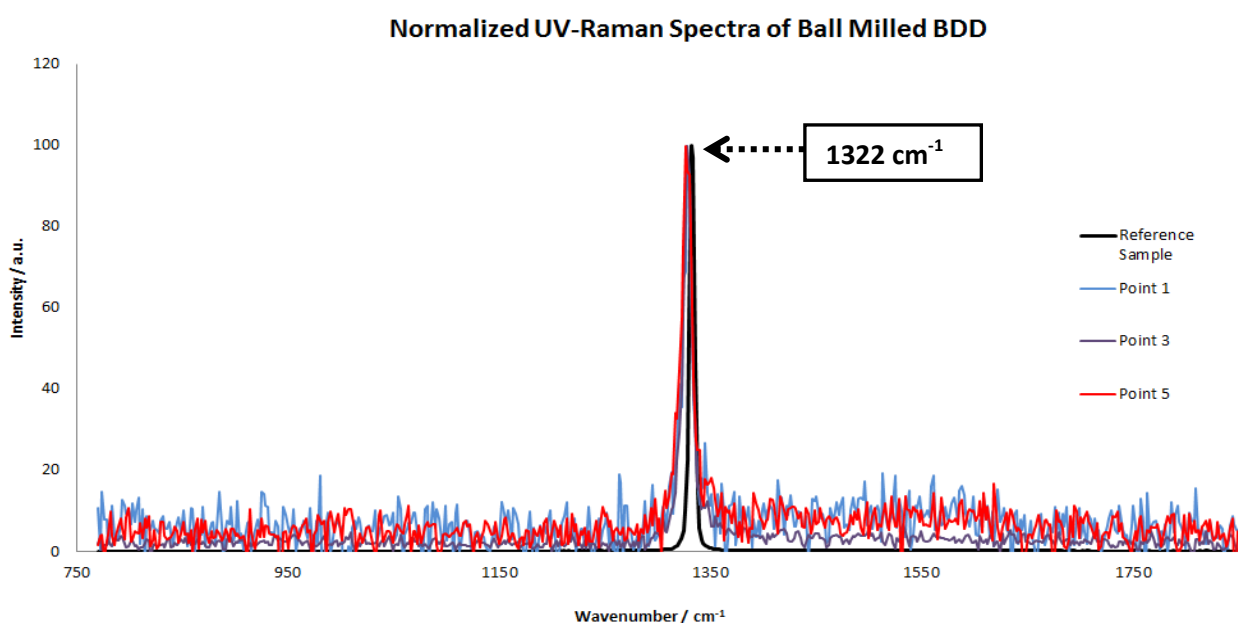
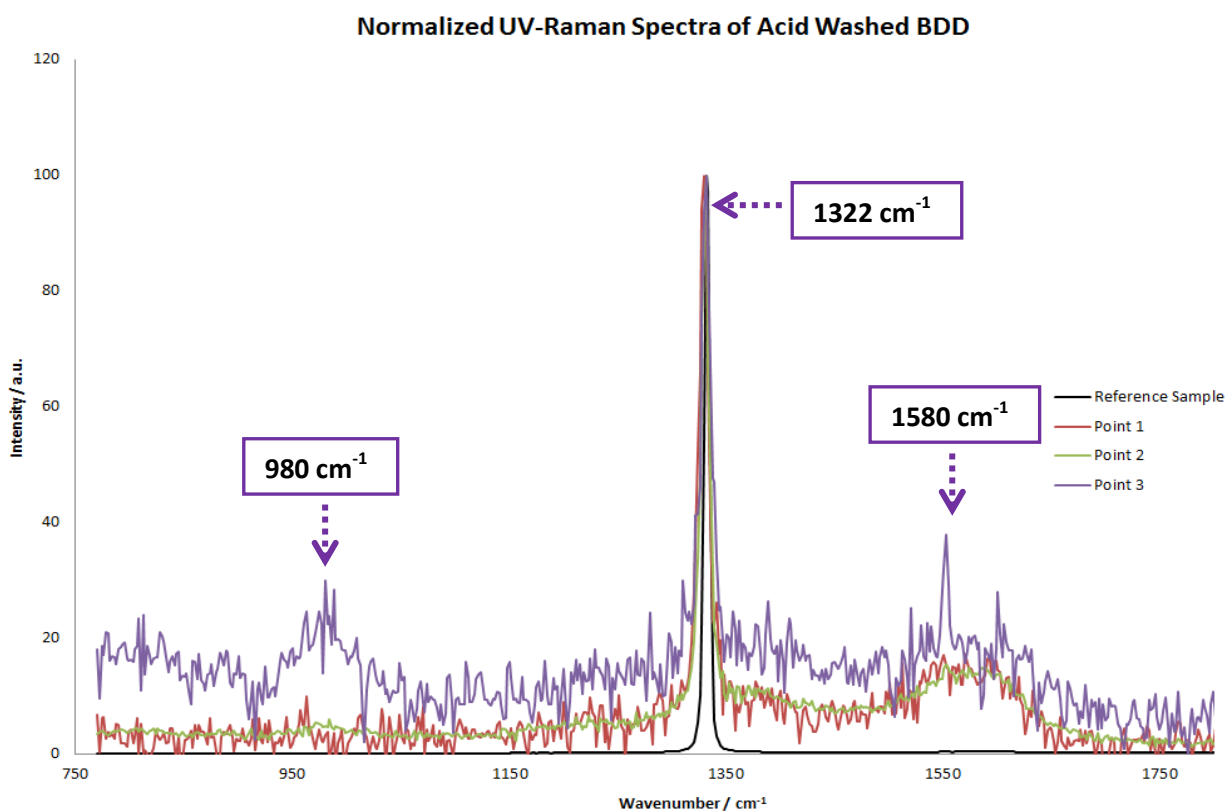


Figure 20. Raman spectra unwashed ball milled BDD (7 hours) calibrated against a CVD diamond reference sample (phonon peak position  $1331.92 \text{ cm}^{-1}$ ). Intensity of each peak is normalised by dividing its maximum intensity by the maximum intensity of diamond at  $1332 \text{ cm}^{-1}$ .

Multiple Raman measurements were taken of ball milled BDD of which a selection has been shown as points in Figure 20. Narrow sharp bands were detected at point 1 at  $1328.1 \text{ cm}^{-1}$ , point 3 at  $1328.1 \text{ cm}^{-1}$  and point 5 at  $1326.19 \text{ cm}^{-1}$ . The average value of all measurements combined is

$1328.1\text{ cm}^{-1}$ . The first order peaks are well fitted with a Lorentzian line shape. All three bands are broader and have shifted downfield from the reference diamond peak by  $3.82\text{ cm}^{-1}$  (points 1 and 3) and  $5.73\text{ cm}^{-1}$  (point 5). The widening and shifting of BDD peaks to lower wavenumbers with respect to the reference peak have been reported in literature<sup>107,108</sup>. Wang et al. explained the shift in peak positions can be attributed towards tensile stress present in grain boundaries. A Raman shift by  $3\text{ cm}^{-1}$  can equate to 1 GPa in tensile stress<sup>108</sup>. It should be noted; the shifts can vary and are dependent on the grade of diamond as well as how they are processed, milled and grinded. The reference sample used was bulk CVD single crystal diamond as opposed to BDD and as such the shifts observed may differ if BDD was used.



**Figure 21.** Raman spectra of acid washed ball milled BDD (7 hours) calibrated against a CVD diamond reference sample (phonon peak position  $1331.92\text{ cm}^{-1}$ ). Intensity of each peak is normalised by dividing its maximum intensity by the maximum intensity of diamond at  $1332\text{ cm}^{-1}$ .

The milled BDD was acid washed to remove non-diamond impurities from the surface. A series of narrow sharp bands were detected at point 1 at  $1329.87\text{ cm}^{-1}$ , point 2 at  $1331.78\text{ cm}^{-1}$  and point 3 at  $1331.78\text{ cm}^{-1}$  and  $980.8\text{ cm}^{-1}$ . A smaller shift and an increase in broadening were noticed in the diamond peaks of the samples with respect to the reference sample. Different facets or edges will give rise to different signals and can explain the decrease in shifts from the reference sample as well as

reasons explained previously for unwashed diamond. The diamond peaks are also asymmetric due to Fano interference (interference between discrete energy states with a continuum of energy states in the same structure). A small G-band appears around the  $1580\text{ cm}^{-1}$  region due to  $\text{sp}^2$  carbon impurities residing within the grain boundaries. Point 3 is a more intense signal due to the measurement time being slightly longer as compared to the rest. The broad peak at  $980.8\text{ cm}^{-1}$  may be due to a more intense background noise due to a longer run time.

### 3.2 Characterizing and optimizing the nominal particle size distribution of diamond

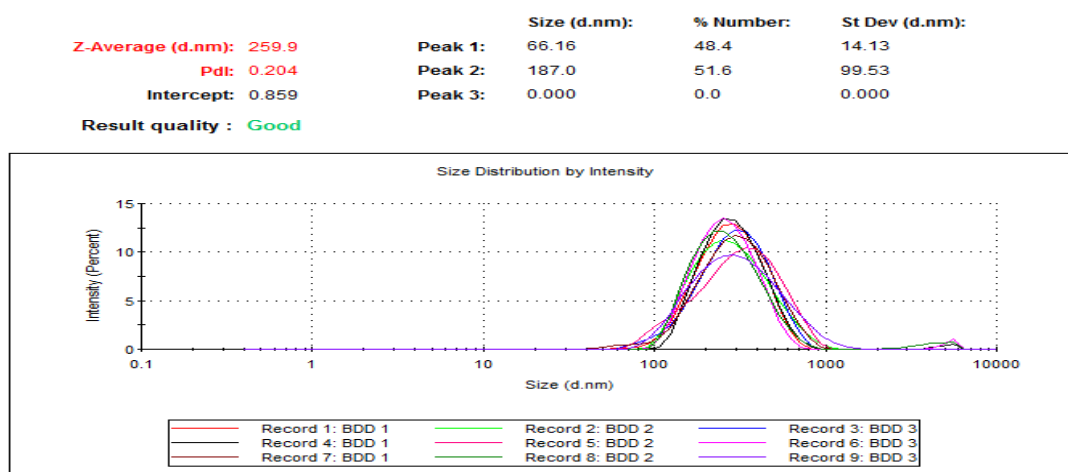
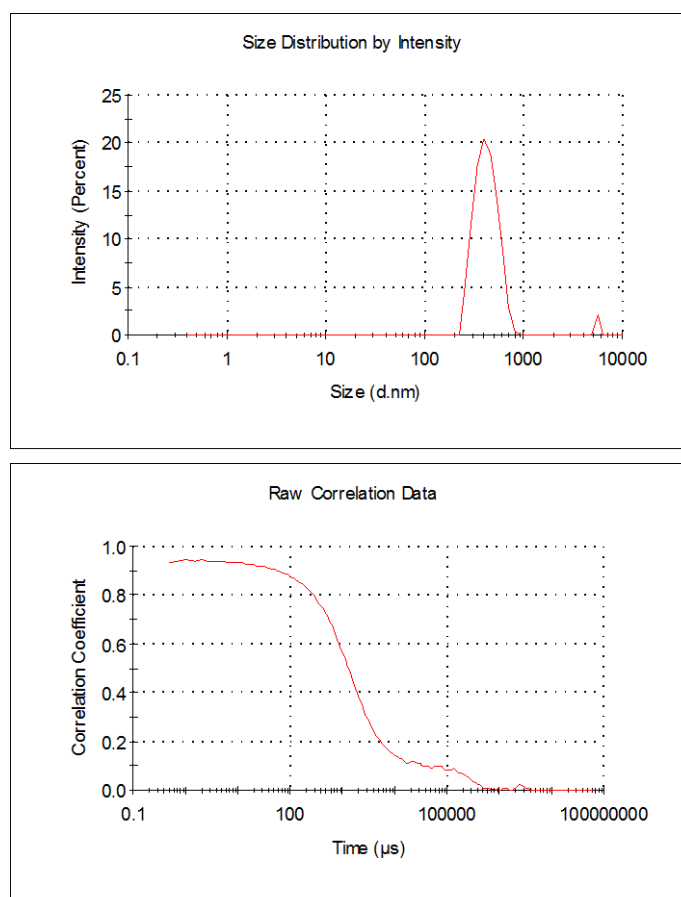


Figure 22 Buffered BDD suspension (pH=8.0) sonicated for 4 hours using an ultrasonic water bath.

Before any self-assembly took place, the acid washed BDD was sonicated to break up any agglomerated clusters. A series of DLS runs were trialled with the sonicated BDD suspension to characterise the size of the BDD particles which produced some very peculiar results. Figure 22 shows the particles had an average size 260 nm however a closer look reveals a bimodal distribution. The results indicate there are still some agglomerates and large particles present, indicating an unstable suspension. The presence of large particles or aggregates can heavily influence the particle distribution and hence the average size due to the way the scattering intensity is calculated<sup>109</sup>. Size distribution by intensity is a good indicator for the presence of large particles and clearly the shape of the curves over multiple repeat measurements confirm a very polydisperse sample. Converting to volume distributions using Mie theory gives a more realistic spread of sizes as it is indicative of how much light a particle of specific diameter  $d$ , scatters and gives the composition of the sample as a volume to mass ratio. The corresponding number and volume distributions showed quite a wide range of particles beyond  $1\text{ }\mu\text{m}$

being present (see appendix). More importantly, the volume distribution also confirmed a large fraction of the sample tested being in the sub-micron region. The results were repeated with similar behaviour being reported each time (see appendix).

The bimodal and non-uniform distributions seen in the DLS data seen in Figure 22 explained by understanding the correlation plot recorded for the sonicated sample as seen in Figure 23. The correlation plot is essentially the plot of the intensity in fluctuations of light scattering as a function of time<sup>110</sup>. It can be evaluated to gauge the quality of the sample. Typically large unstable particles will give irregularities in the fluctuation signal as particles start to agglomerate and sediment to the bottom of the cuvette. This signal is converted to the exponential decay function below. The shape of the decaying exponential function identifies key components which are used to identify the z-average diameter. The plot below shows fluctuations in the baseline, in what should be a smooth decaying signal indicating aggregation as well as a long decay time highlighting the particles are no longer moving in random Brownian motion and hence precipitating out of solution<sup>110</sup>.



**Figure 23. Correlation plot of sonicated BDD.**

### 3.3 Optimizing the Size of BDD Particles

Clearly the suspension needed to be optimized in order to attain reliable DLS data. In other words, large particles had to be removed from the sample using a relatively non-invasive technique. Centrifugation is used commercially in industry to optimize and control the size of detonated diamond to produce relatively mono disperse suspensions<sup>111</sup>. The samples were sonicated for 4 hours followed by centrifuging for 60 seconds before being tested using DLS. Figure 24 shows the result of this process. The bed of nanodiamond has mostly disappeared indicating the removal of large unstable particles as a result of centrifugal force. The discoloration of the suspension and decrease in opacity also suggest the diamond weight concentration has decreased due to a significant number of large particles precipitating.

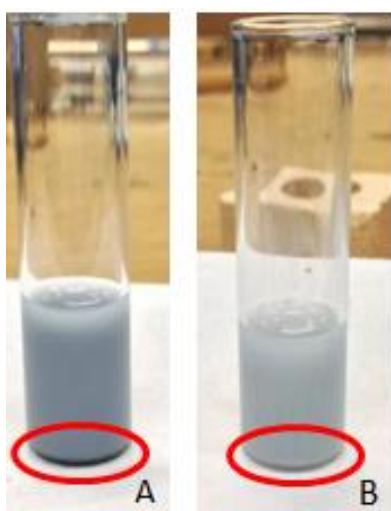


**Figure 24. (A) Nanodiamond suspension after sonication for 4 hours. (B) Nanodiamond suspension after sonication for 4 hours followed by centrifugation for 60 seconds.**

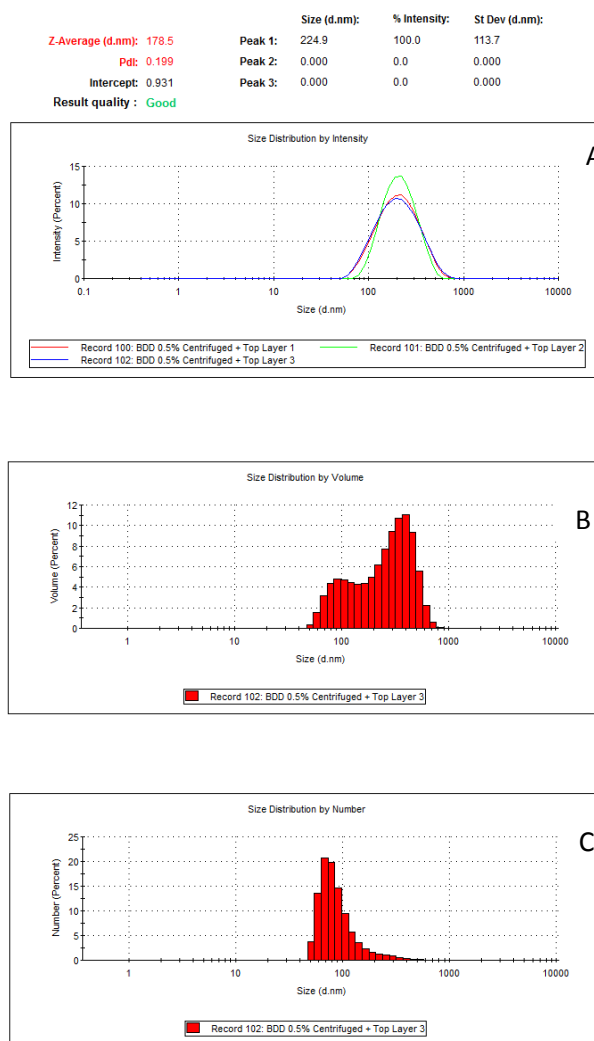


(Figure 25). The DLS data for the centrifuged sample show a much smaller distribution width and are well fitted to a Gaussian distribution indicating the problems observed in the sonicated samples have somewhat been eradicated. The frequency curves were converted to volume and number distributions in the form of histograms to give a more detailed size distribution. Across an average of the three runs, the number distribution showed 58.4% of the total particles measured, to below 100 nm, 41.6% between 100 nm and 500 nm and 0.1% above 500 nm. The volume distribution show, the total volume comes from 10.3% of particles below 100 nm, 84.0% between 100 and 500 nm and 5.6% above 500 nm. Therefore as a total, particles between 100 nm and 500 nm occupy a much larger mass or volume.

The shape of the histograms still suggest at least two to three classes of particle sizes still exist. Controlling the size distribution is a challenging process and questions the laboratory setup of milling and centrifuging to obtain the best quality samples of BDD. Typically an industrial process as described by Boudou et al. uses 250 g of raw material (detonated microdiamond) followed by jet milling under

high pressure, ball milling (24 hours) and multiple centrifuging steps to purify and optimize the size of diamond to obtain a concentrated solution > 10% w/v of ultrananodiamond with a mean diameter of less than 10 nm<sup>111</sup>. This is in contrast to the 1% stock which was used in this project and as the results suggests, was mainly composed large particles. This concentration was further diluted after centrifugation.

### 3.4 Centrifuged vs. Non-Centrifuged Samples

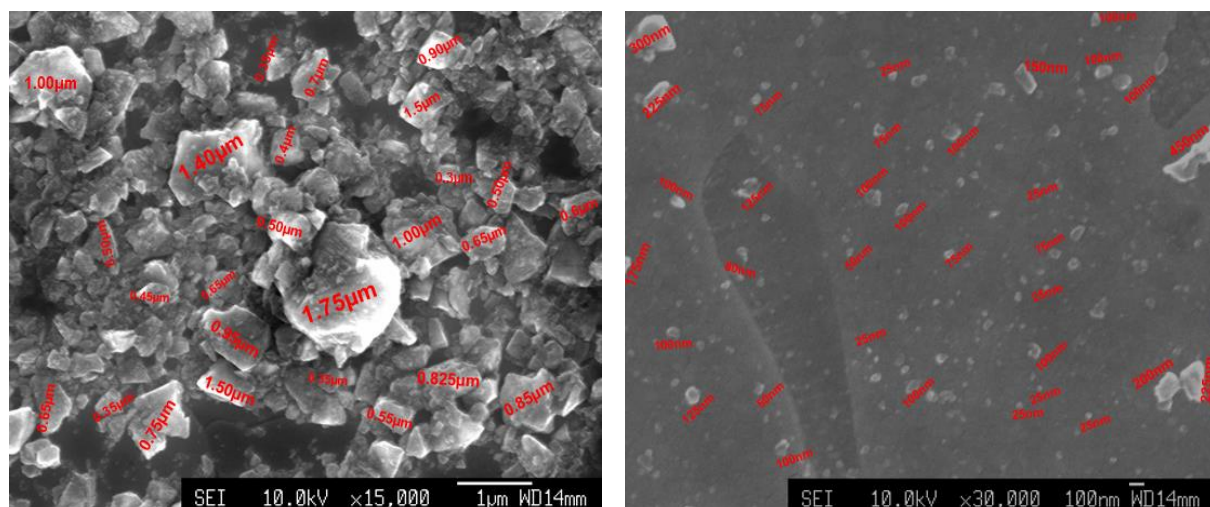


Figure 26. Identical samples of W were treated at 500 °C with LMW PEI (0.5%) + 0.5% BDD under optimized conditions. Left image shows nanodiamond which has only been sonicated. Right image shows nanodiamond which has been centrifuged after sonication. Both samples were left to electrostatically self-assemble for 30 minutes. Particle sizes are approximate.

The DLS data indicated centrifuging the BDD suspension aids in controlling the particle size and was thus used as part of the optimization procedure in self-assembly. The true effects of centrifuging the samples can be seen during self-assembly where typically 5-10 ml of suspension is dropped on the PEI coated surface of W. The differences in the nominal particle sizes between both samples are quite remarkable. Without any centrifuging, the particle sizes range from approximately 0.35 μm to 1.75 μm. Combining sonication (4 hours) and centrifuging (60 seconds) steps and using the supernatant for self-assembly results in a much smaller and uniform distribution, with a range of 0.425 μm.

A closer inspection of the centrifuged sample also shows speck like diamond particles which were below 100 nm but due to poor resolution it is hard to distinguish their true dimensions even at x40,000 magnification. It is clear centrifugation reduced the agglomeration of diamond particles which had been an issue in previous self-assembled samples however it did not completely eradicate it from the

surface as seen in section 3.7. It should also be noted, there has been a marked decrease in particle size and the nucleation density, indicating that more than one diamond coating is needed as the nanodiamond weight concentration is no longer at 0.5% w/v after centrifuging.

### 3.5 Self-Assembling BDD to W

The section will review some of the variables that were investigated to find the best possible conditions that gave the highest surface coverage of diamond.

### 3.6 Importance of the Oxide Layer

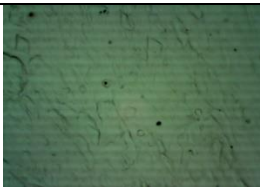
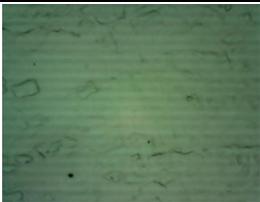
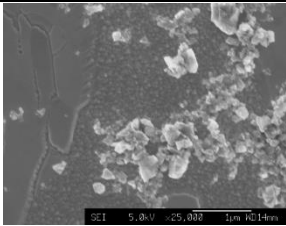
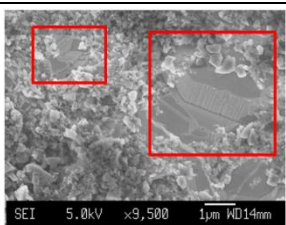
| Sample Type  | Optical Microscope at x10 magnification   | FE-SEM   |
|--|---|--|
| W cleaned with solvent + 0.5% LMW PEI + 0.5% BDD (A) |   |  |
| W with solvent + 0.5% HMW PEI + 0.5% BDD (B)         |  |  |
| W etched + 0.5% LMW PEI + 0.5% BDD (C)               |  |  |
| W etched + 0.5% HMW PEI + 0.5% BDD (D)               |  |  |

Figure 27. Comparison of self assembly on the native oxide layer of W (A and B) versus a freshly deposited oxide layer (C and D).

To begin, substrates of W which had been washed with solvents as described in section 2.2 were dipped in PEI of LMW or HMW, followed by a coating of nanodiamond. At x10 magnification the samples showed very little if any coverage of diamond after being rinsed with ethanol and water to remove excess PEI. The samples had failed to self-assemble possibly due to no PEI adhering to the W substrate.

Further investigation of this finding led to the examination into the surface chemistry of W. It is well known, W like many other refractory metals has a native oxide layer protecting it from corrosion. Naturally, it is also expected the surface carries a charge known as the surface charge which is the electric charge present at the surface or interface when in solution. The electric charge is also subject to change with solutions of different pH. Atoms such as R-OH which can be protonated/deprotonated also have the ability to leave the surface charged. The pH at which the surface has no net electric charge (isoelectric point, IEP) for W is in the region of 0.2-0.5<sup>112,113</sup>. Solutions of pH above this region will result in the surface gaining a net negative charge and positive for below this. The zeta potential measurements for WO<sub>3</sub> in media ranging from pH 2-12 show a value of below -40 mV indicating the surface should have a negative charge<sup>114</sup>. Therefore in theory, the aqueous solution of PEI should have adsorbed to the surface of W but clearly this was not the case.

The observation led to the oxide layer being removed as described in section 2.2.2 to ascertain whether the adsorption of PEI truly depended on the oxide layer. The surface was etched followed by exposure to air and dipped in PEI. An immediate improvement was seen as self-assembly had occurred as seen in SEM images (C and D) in Figure 27. The samples show multi-layers of PEI entangled with diamond forming amorphous like layers in regions where bare W metal is exposed i.e. regions where no PEI has been deposited. This can be seen as bare patches both under an optical microscope and through SEM (highlighted in red) due to no oxide layer present and hence no diamond. Clearly the oxide layer plays an integral part in PEI being adsorbed however further information was required to explain why this was.

### 3.7 Enhancing the Surface Oxide and the Effect of PEI Molecular Weights

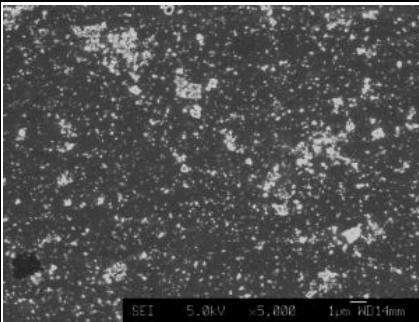
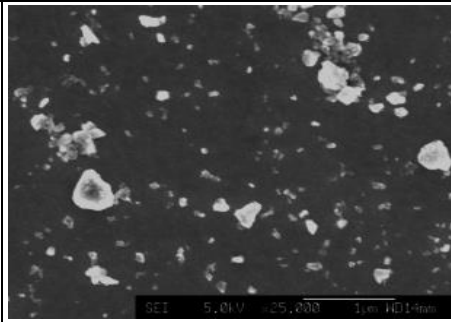
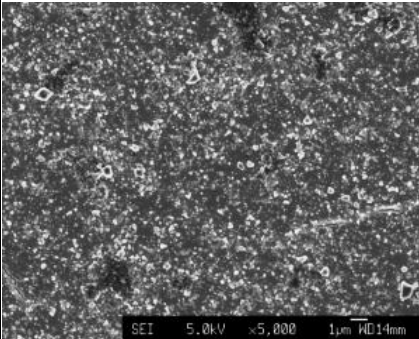
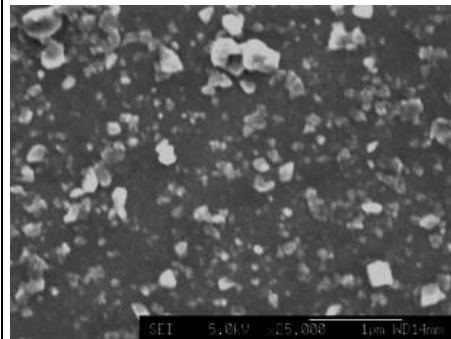
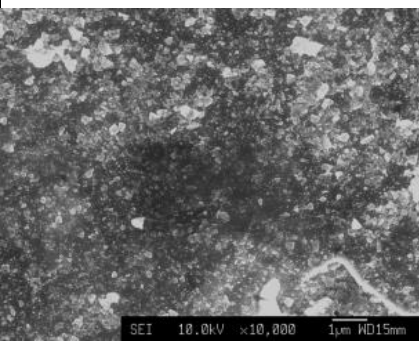
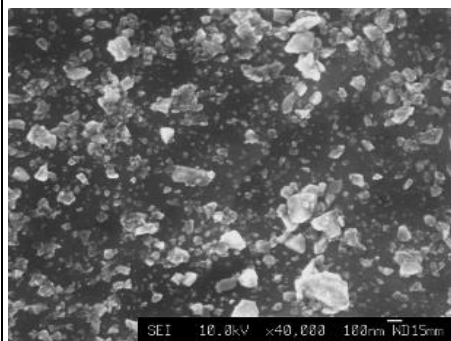
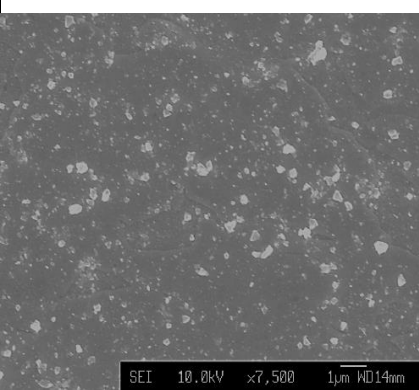
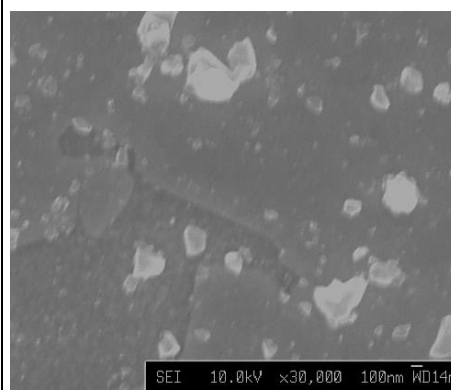
| Sample Type  | FE-SEM Images   |  |
|--|---|--|
| <b>W + <math>\Delta</math> + O<sub>3</sub></b><br><b>0.5% HMW</b><br><b>PEI + 0.5%</b><br><b>BDD (A)</b> |    |    |
| <b>W + <math>\Delta</math> + O<sub>3</sub> +</b><br><b>5% HMW PEI</b><br><b>+ 0.5% BDD (B)</b>           |   |   |
| <b>W+ O<sub>3</sub> + 0.5%</b><br><b>LMW PEI +</b><br><b>0.5% BDD (C)</b>                                |  |  |
| <b>W+ O<sub>3</sub> + 5%</b><br><b>LMW PEI +</b><br><b>0.5% BDD (D)</b>                                  |  |  |

Figure 28. SEM images of samples with adequate nucleation density for FE-testing.

| Sample Type   | Nucleation Density / Particles $\mu\text{m}^{-2}$ | Area Coverage / % |
|---|---|-------------------|
| W + $\Delta$ + O <sub>3</sub> + 0.5% HMW PEI + 0.5% BDD (A) | $9 \pm 5$   | 12.60             |
| W + $\Delta$ + O <sub>3</sub> + 5% HMW PEI + 0.5% BDD (B)   | $17 \pm 5$  | 18.80             |
| W + O <sub>3</sub> + 0.5% LMW PEI + 0.5% BDD (C)            | $112 \pm 25$                                      | 39.73             |
| W + O <sub>3</sub> + 5% LMW PEI + 0.5% BDD (D)              | $15 \pm 5$  | 7.40              |

Figure 29. Nucleation densities and fractional area coverage of samples seen in Figure 28 calculated using ImageJ v1.47. All areas sampled were  $10 \mu\text{m} \times 10 \mu\text{m}$  in dimension.

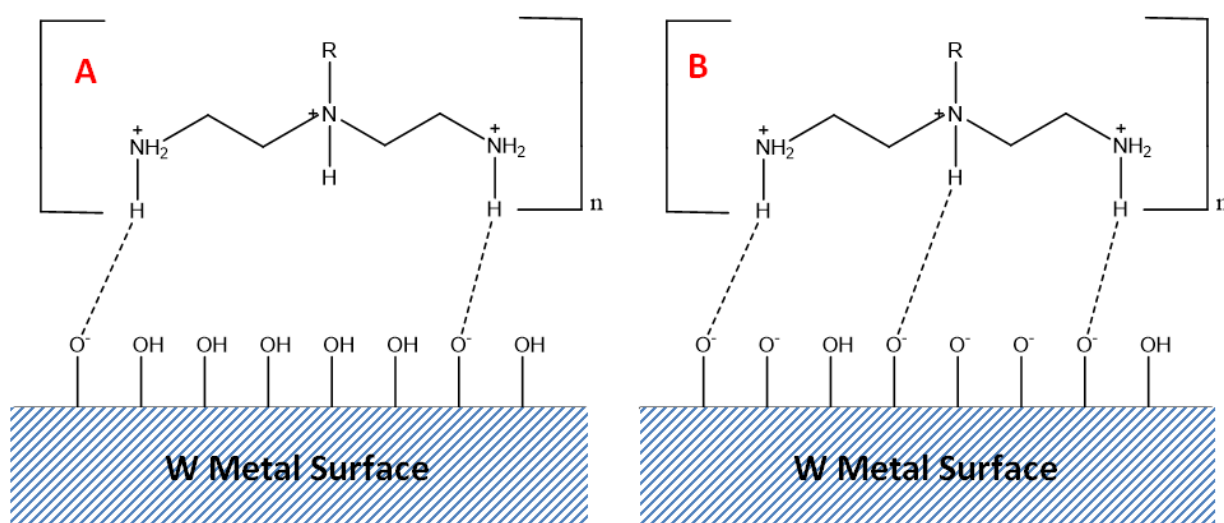


Figure 30. W surface cleaned with solvents and no other treatments (A). W surface treated with ozone (atomic oxygen) or thermally oxidised (B) or both.

Before the nucleation densities between the various samples are discussed first let's consider why self-assembly was successful on treated surfaces of W (Figure 28). The model seen in Figure 30 shows a simple model comparing the electrostatic attraction between treated and untreated surfaces of W to PEI, using properties specific to this system.

The untreated surface of W is known to be inert to most chemicals, a recurring theme for most carbide forming materials. The oxide layer will have a higher ratio of OH groups to  $\text{O}^-$  to maintain its inertness. Due to this, electrostatic attraction between PEI and the surface could prove to be difficult as most of the 'active sites' for hydrogen exchange are blocked. The electronegativity of oxygen makes it difficult for hydrogen exchange to occur between it and the nitrogen bearing hydrogen groups. Repeating this over a large surface area, the lack of attractions between the surface and the polymer would result it in being washed off.

Alternatively, treating the surface with the UV/Ozone cleaner essentially attacks the surface with atomic oxygen depositing more  $\text{O}^-$  groups. In other words, the surface is packed more densely with  $\text{O}^-$

groups than OH groups making it more polar and thus the surface has a higher charge density. As the substrate is immersed in the aqueous solution of PEI, the now highly polarized surface makes it easier for electrostatic attractions in the form of hydrogen bonding to take place. The negatively charged O group is able to distort the electron cloud of hydrogen pulling it closer towards itself eventually forming a layer of PEI when the process is repeated over a larger surface area.

The model is still very basic and other conditions such as pH, pKa and zeta potentials of the surface and PEI solution need to be considered to fully understand the mechanism. In summary, the model is a lot more complex than previously thought.

### 3.8 Effect of PEI Molecular Weight on Nucleation Density

Assuming the BDD observed is electrostatically bound to PEI and the excess has been washed off, Figure 28 (A and B) shows two distinct types of nanodiamond layers when using HMW polymer during the self-assembly procedure. (A) Shows an 'islands of diamonds' type layer whereas B shows a continuous film type layer. This difference can be related to the molecular weight of the PEI. HMW polymer will typically have many long chains and a high degree of branching present in its structure in aqueous solution, allowing an infinite number of conformations to take form on the surface of W. The increased branching present in HMW polymer also allows a large surface area to be present to capture any nanodiamond, which could be a reason why 5% HMW PEI shows a higher nucleation density than 0.5% HMW PEI. There are also disadvantages of using a polymer of such HMW. The HMW samples show areas where no BDD is present. Tofts has suggested this is due to HMW polymers having a high tendency to entangle because of their long chain lengths and as a result, there will be electrostatic repulsion present between polymers that are firmly bound to the W surface and free polymer which is not<sup>78</sup>. During washing steps, unbound polymer may be washed away leaving a patchy surface. The entanglement may also cause the surface for self-assembly to be uneven making it difficult to form a monolayer.

Image C in Figure 28 was the result of repeating the self-assembly of immersing LMW PEI coated W in BDD twice with a wash step being applied between each immersion. Although there is a respectable coverage of nanodiamond present on the surface (39%), there is also some agglomeration present. This has been explained in section 3.9. Using LMW in theory provides better packing of the polymer on the surface due to short chain lengths. Berret et al have reported LMW surfactants have a tendency to 'stick' together to form micelle type structures in water to reduce the area of the surfactant in contact

with water thus leading to the reduction in the free energy of the system<sup>115</sup>. Similarly, this can be translated to the system being used in this project, where “tightly linked, dense layers” of PEI can form on the surface of W<sup>78</sup>. A denser layer of PEI provides a larger surface area for assembly to take place.

Reproducing the samples proved to be difficult as seen in the SEM images (see appendix). With this in mind, the difference in coverage cannot directly be linked to the molecular weight of PEI but rather a combination of factors which are discussed further.

It is difficult to rule out which molecular weight gave the best nucleation density as they were taken at different magnifications and conditions. It is difficult to identify which surface treatment gave the best surface coverage as not all permutations of assembly conditions could be tried.

To be able to make credible comparisons between the different molecular weights of PEI, the following assumptions should be taken into account. All the nanodiamond present on the surface has occurred as a result of electrostatic self-assembly and not sedimentation. Any uncharged nanodiamond has been washed off the surface and the percentage weight concentration of nanodiamond is constant throughout the self-assembly. The concentration of nanodiamond has already been shown in section 3.3 to be decreasing throughout the fabrication process, which could be a key factor in the reduced nucleation density of the self-assembled samples. The other factor which could be causing the sparse layers is the lack of negatively charged nanodiamond present on the PEI coated surface of W. The washing step of the fabrication procedure has been optimized to remove any unbound nanodiamond on the surface. This factor has been further explored in the section 3.9.

### **3.9 Assessing the Stability of the Diamond Suspension Using Zeta Potentials**

The most obvious measures to disperse and stabilise BDD in solution were taken. The diamond had been acid washed with the surface expected to gain a negative charge through surface terminations involving OH and COOH functional groups. These are known to exist when acid washing with HNO<sub>3</sub>/H<sub>2</sub>SO<sub>4</sub><sup>116</sup>. The nanodiamond was also suspended in pH 8 buffer to aid in maximising repulsion to form an agglomerate free suspension, yet some sedimentation still occurred after sonication. This was the first clue which highlighted not all the particles may have a negative charge in addition to being quite large as well. The SEM images of self-assembled samples showing non-uniformly distributed diamond on W (Figure 28) also reinforced this observation. Looking back at the DLS spectra (Figure 25) and the SEM images (Figure 28) it is inherently clear not all particles acquired a negative charge due to

their very large sizes. To test this hypothesis, the zeta potential of the centrifuged BDD suspension was measured.

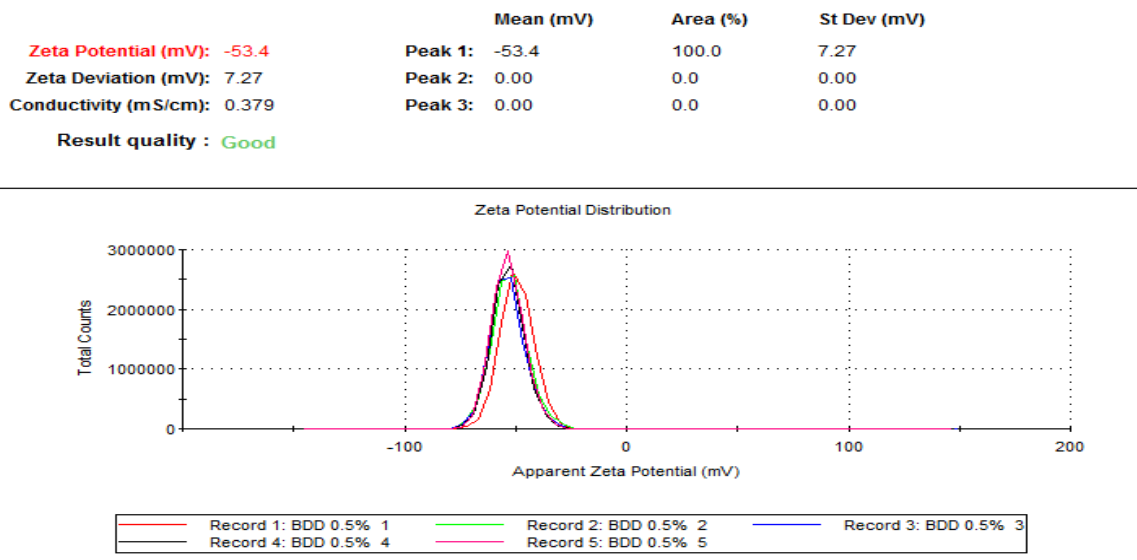


**Figure 31. Zeta potential measurements of sonicated and centrifuged BDD suspension.**

The zeta potential value of -53.4 mV over a series of repeats indicated the diamond particles in the buffered solution had acquired a negatively charged surface to be sufficiently stable in solution and not agglomerate. It should be noted; the value quoted is the mean value and is not representative of all the particles present.

The following conclusions were drawn from all the data gathered from the various experiments carried out. Due to the wide distribution of particle sizes and their unsymmetrical shapes a considerable fraction of diamond is washed of the surface due to a lack of surface charge. The surfaces of these particles are not necessarily smooth and as such not all of the surface can be terminated with OH groups or other surface bound oxygen groups. Furthermore, work by Chang et al using Density Functional Tight Binding (DFTB), has shown negatively charged (111)<sup>-</sup> and near-neutral (111)<sup>0</sup> diamond facets can electrostatically interact via incoherent interfacial coulombic Interaction (IICI) to form thermodynamically stable, randomly ordered small clusters of nanodiamond 100-200 nm in size<sup>117</sup>. As the BDD is polycrystalline, the particle facet interactions cannot be ruled out and should be considered in explaining the sedimentation of diamond seen in Figure 24 and the weakly bound clusters seen in some samples in Figure 28.

The data provided so far shows a handful of samples which were of a high quality and standard to be taken for lithiation and eventually field emission. The self-assembly procedure of BDD to W is a

complex procedure with many variables needing to be controlled. The experimental findings observed are open to discussion. It has also provided a deeper understanding into the various parameters which need to be optimized in order to achieve a sample with a good coverage of nanodiamond on the surface.

### 3.10 Field Emission

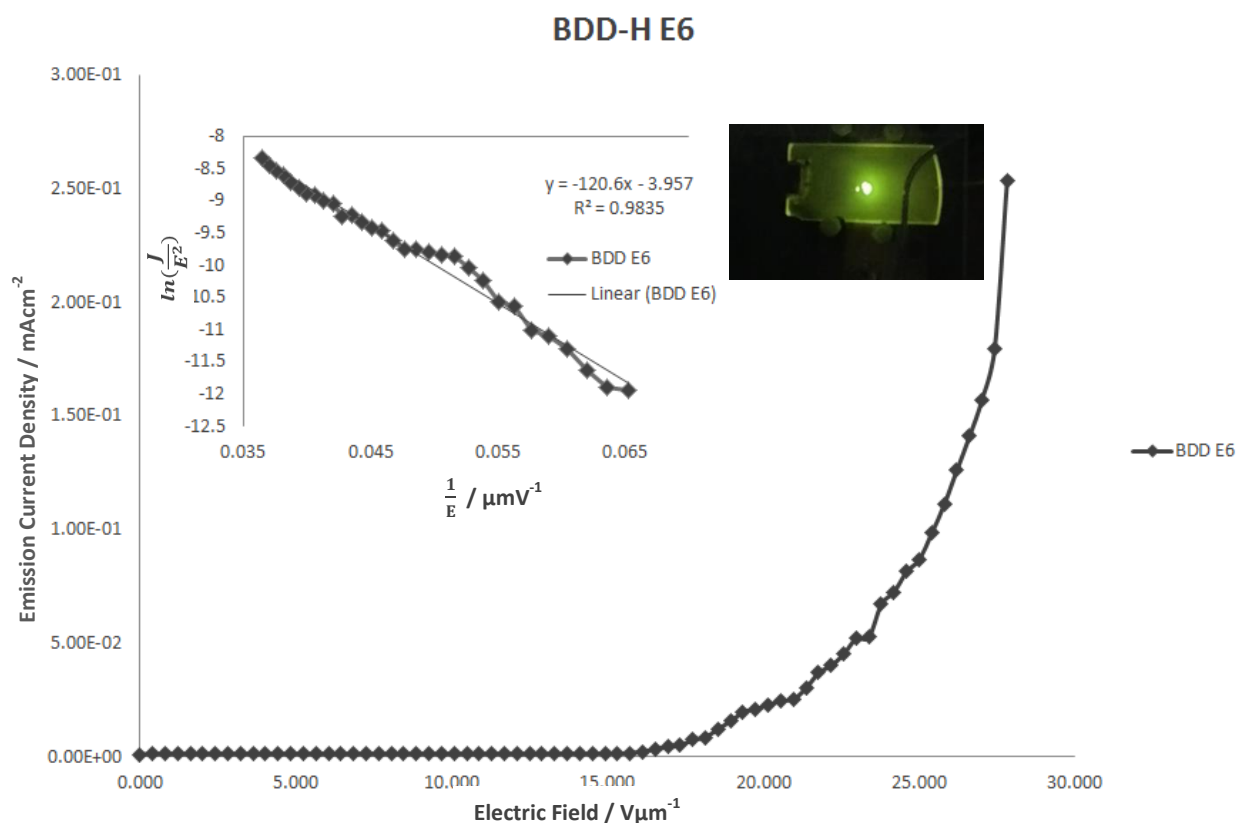


**Figure 32.** Field emission of freestanding CVD polycrystalline BDD-H showing a curve of emission current density, versus electric field,  $E$ , over an average of 10 runs. The inset shows the corresponding Fowler-Nordheim plot and the sites of emission as seen on the phosphor screen.

The following results are for the reference sample to which the self-assembled samples will be compared to. The exponential relationship of emission current density against varying electric field is characteristic of the behaviour typically observed in H-terminated BDD films. The graph of  $\ln\left(\frac{J}{E^2}\right)$  versus  $\frac{1}{E}$  shows the turn on field of H-terminated BDD to be at a value of  $18.5 \text{ V}\mu\text{m}^{-1}$ . The threshold field could not be determined due to the electric field being turned off at 3 kV to prevent any damage to the sample as it was also being used a reference sample for other devices. Maximum current density of  $2.5 \mu\text{Acm}^{-2}$  is achieved at  $27 \text{ V}\mu\text{m}^{-1}$ . The turn on field compares well with literature values. Zhu et al. reported turn on values of  $16 \text{ V}\mu\text{m}^{-1}$  and  $21 \text{ V}\mu\text{m}^{-1}$  for boron doped CVD films with dopant

concentrations between ( $10^{19}$  -  $10^{20}$   $\text{cm}^{-3}$ ) similar, to that of the reference sample tested which is approximated to be at ( $10^{20}$   $\text{cm}^{-3}$ )<sup>118</sup>. Geis et al have reported values in the region of 20-50  $\text{V}\mu\text{m}^{-1}$  at dopant concentrations of ( $10^{19}$   $\text{cm}^{-3}$ )<sup>119</sup>.

The perturbations seen in the turn on fields between different polycrystalline BDD films can be explained by studying the dopant concentrations and the grain size/boundaries of BDD, factors known to have a strong influence<sup>105</sup>. Koinkar et al showed heavily doped B CVD films resulted in the increase in electrical conductivity of the film with a turn on field of 0.80  $\text{V}\mu\text{m}^{-1}$  when compared to lighter doped films, possibly due to the formation of an impurity band above the valence band maximum<sup>105</sup>. They also suggested the grain size also has an effect in enhancing the field emission behaviour. Wu et al has extensively studied the effects of grain size for field emission. A polycrystalline film deposited will contain a non-uniform distribution of grain sizes present on the surface leading to grain boundaries lined with conductive graphitic pathways (typically present in CVD BDD films). It is beneficial to make the grains as small as possible as not only do they provide more pathways for conduction hence large areas of grain boundaries but also provide a large surface area for electron emission<sup>120</sup>. It is suggested in their theoretical model, the graphitic channels act as the starting point for conduction which fills the voids between closely packed grains. As the electric field is ramped, electrons are able to tunnel through the graphite/diamond interface followed by electron tunnelling through the edges of neighbouring grains<sup>120</sup>. Smaller grain sizes are a significant factor in lowering the turn on field of the material as well as improving the current density of the material<sup>121,122</sup>.

The fluctuations in current seen in Figure 32 of the BDD films can be explained by understanding the surface morphology. A polycrystalline film will have a rough non-uniform surface with facets of nanodiamond protruding from the surface at various different angles and heights. The sharpest and tallest points on the surface will be the first to emit electrons as they will benefit from a large field enhancement factor. Such features of an emitter will result the in electric field localizing at points (edges/facets) and as a result, the barrier for quantum tunnelling is thinned allowing electrons to escape into vacuum. Non-uniformity in the surface prevents stable field emission being observed due a number of reasons. Koinkar et al have observed 'spikes' in the current density for B doped CVD films during stability testing, when the film was subjected high electric fields for prolonged periods of time. Much like CNTs, the polycrystalline diamond can also be exposed to ion bombardment or adsorption of gas atoms and molecules even under vacuum conditions which can cause detrimental damage to the emitter surface causing a change in its electrical properties i.e. workfunction<sup>68,105</sup>. Typically emission sites with ideal features are the first to undergo this process. At this point the current jumps

to the next favourable emission site. This breakdown is characterised visually as flickering observed on the phosphor screen.

The obvious solution to uniform current emission is to make the nanodiamond particles as identical as possible in shape height size etc. however as the project has shown this is no trivial matter and controlling the geometry of the nanoparticles is a challenge in itself. It was expected the fabrication procedure would minimize some of the problems discussed above and a smooth I-V curve could be obtained for the self-assembled BDD sample. For example, repeatedly milling and centrifuging the polycrystalline BDD can result in smaller more uniform grain sizes, a much greater surface area for emission and potentially mitigate the flickering seen in Figure 32 due to geometry of the particle sizes being fairly similar.

All 4 samples in seen in Figure 28 were tested however no field emission was observed. At an applied electric field of  $50 \text{ V}\mu\text{m}^{-1}$ , electrical arcing was observed. As no literature value is quoted for LiO terminated BDD on W, it is speculated the field emission behaviour should be similar to that seen of H-terminated BDD (Figure 32). This is due to both BDD-H and BDD-OLi being p-type semiconductors with a NEA surface. Assuming the field emission kit was in perfect working order, efforts were focused on characterizing the failed samples.

### 3.11 Post-Field Emission Analysis

#### 3.11.1 Surface Conductivity

Without any field emission data for lithiated samples it is quite hard to make comparisons to the reference sample. Sample B in Figure 28 was chosen due to it being the sample with the best fractional coverage and uniformity. It should be noted between the self-assembly step of depositing BDD onto PEI coated W, no further SEM images were taken of this sample until it had been lithiated.

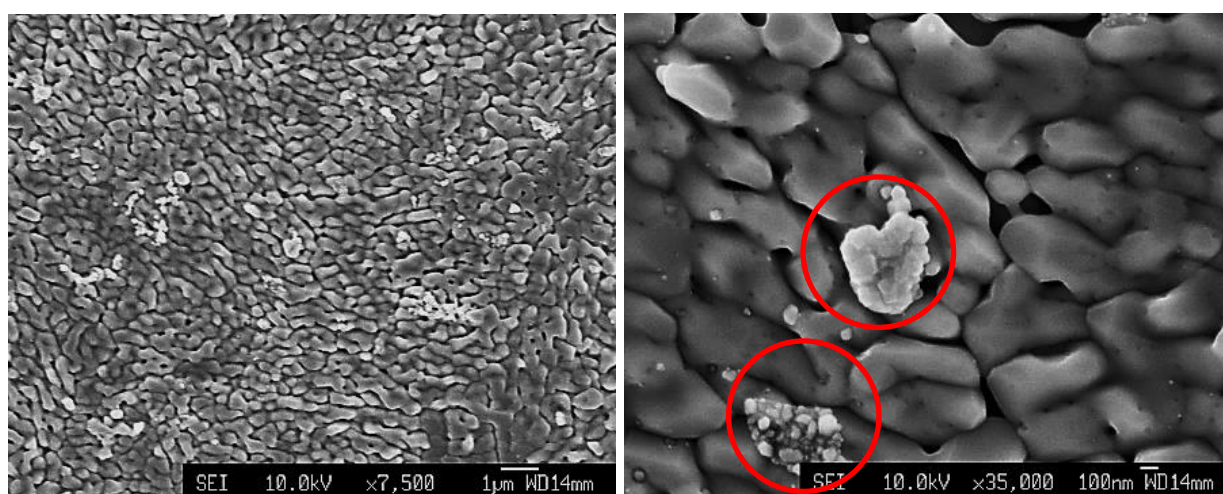


Figure 33. SEM image shows W +  $\Delta$  + O<sub>3</sub> + 5% HMW PEI + 0.5% BDD + OLi

The difference in surface morphology after the surface had been annealed and lithiated was quite surprising. The surface seen in (Figure 28.B) had now been mostly been stripped of its nanodiamond layer leaving only a rough amorphous type layer behind which is speculated to be W (Figure 33). An optical microscope image of pristine W shows a similar pattern to that seen above (see appendix). The optical image of the lithiated sample was also in agreement with the SEM image. Other optical images of lithiated samples have been provided in the appendix.

After meticulously scanning the surface over multiple points, the image seen in Figure 33 was obtained. The coverage of what is expected to be diamond on the surface is most likely to be below 1%, even at x35,000 magnification the surface is very sparsely populated with only a few grains (circled) and specks being observed. The grains are also more rounded indicating the nanodiamond which has remained on the surface after vacuum annealing and lithiation, has had its facets destroyed which significantly impacts its ability to emit electrons. A sparse layer is a likely explanation as to why no field emission was observed. The large voids surrounding the diamond particles also suggest that

any diamond that has remained on the surface is most likely debris. The washing step is optimized to remove any unbound particles from the surface and after drying following coverage is observed. The SEM image provides two reasons that could possibly cause the loss in nanodiamond on the surface. The diamond is not completely consolidated to the metal as a result of the annealing conditions not being optimized. The other reason is the surface roughness of the metal. Smoother surfaces have larger overlap volumes than rougher surfaces and are thus more likely to assemble<sup>123</sup>.

More information on the properties of the samples is needed before any concrete judgements could be made as to what is causing the further loss of diamond on the samples. The loss of diamond cannot be said for all the other samples in Figure 28 as they have not been imaged using SEM after being annealed. It is clear, using a finite amount of feedstock material has led to numerous challenges being developed and highlighted just how complex the procedure is.

### 3.11.2 4-Point Probe Measurements

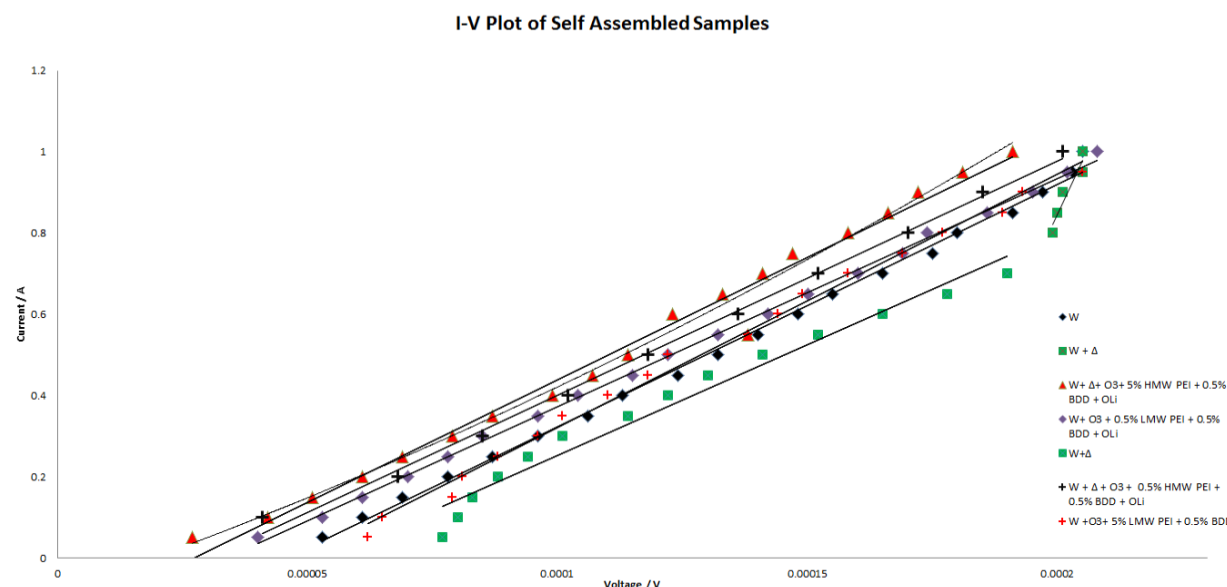


Figure 34. 4-point probe measurements of self-assembled samples under various conditions.

| Sample   | Resistance / mΩ | Resistivity / μΩ.m | Sheet Resistance / mΩ.sq <sup>-1</sup> | R <sup>2</sup> Value |
|--|-----------------|--------------------|--|----------------------|
| W  | 0.1680          | 0.0252             | 0.1680                                 | 0.9972               |
| W+Δ  | 0.1840          | 0.0276             | 0.1840                                 | 0.9708               |
| W+Δ+O <sub>3</sub> +0.5% HMW PEI +0.5% BDD + OLi | 0.1730          | 0.0260             | 0.1730                                 | 0.9968               |
| W+Δ+O <sub>3</sub> +5% HMW PEI +0.5% BDD + OLi   | 0.1660          | 0.0249             | 0.1660                                 | 0.9862               |
| W+O <sub>3</sub> +0.5% LMW PEI +0.5% BDD + OLi   | 0.1780          | 0.0267             | 0.1780                                 | 0.9991               |
| W+O <sub>3</sub> +5% LMW PEI +0.5% BDD           | 0.1600          | 0.0240             | 0.1600                                 | 0.9945               |

**Figure 35. Resistance and sheet resistance values of self-assembled samples under different conditions. All samples of W were a 1x1 cm square with a thickness value of 0.15 mm. All samples containing BDD have been annealed.**

The aim of surface conductivity measurements was to assess the diamond coverage present on the W. If the surface was mainly metallic due to the loss of nanodiamond, which so far previous results have suggested, then ohmic like behaviour should be observed in the I-V plots. A 4-point probe setup as described in section 2.11 was used to measure the resistivity of a range of samples given in Figure 34. The samples in Figure 28 were tested and compared against a reference sample of a W square which had been cleaned using only solvents. The current was varied and the resultant voltage was measured. The I-V plots have been given in Figure 35. The electrical resistivity of W is reported to be on the order of  $(10^{-8} \Omega\text{m})$ <sup>124</sup> at 25 °C which is in agreement with the value obtained from the reference sample. The values calculated are approximate figures and were simply used to compare resistivity values of W against W with BDD present on the surface.

The results of the lithiated samples showed resistivity values on the same order as the reference sample with very marginal differences seen indicating the majority of the surface was bare metal. In theory, if there was sufficient coverage present, then large increases in resistivity values should have been observed as boron doped diamond is a p-type semiconductor and PEI is known an insulator<sup>125</sup>.

W with only boron doped diamond present reported a resistance value  $1.6 \times 10^{-4} \Omega$ . May et al. have reported resistance values of microcrystalline and faceted nanocrystalline BDD CVD films of varying boron content ( $10^{19}$ - $10^{21} \text{ cm}^{-3}$ ) in the range of (9 to 3800  $\Omega$ )<sup>107</sup>. The results seen for this sample do not correlate with literature, further confirming the presence of a non-diamond surface.

The resistivity of W which had been thermally treated (W + Δ) and thus oxidised showed no significant increase with a value of  $1.84 \times 10^{-3} \Omega$ . The value was calculated for the linear part of the curve. This was as expected as tungsten oxide is conductive and is said to be an n-type semiconductor<sup>126</sup>. The curve shape however suggests it may have been an anomalous result as it shows a decrease in resistance as voltage increases. Repeat measurements are needed.

There is a strong possibility the lack of coverage of nanodiamond on the surface resulted in only the oxide layer of W being in contact with the probes leading to the ohmic behaviour seen. Such is the

setup of the instrument; the samples could only be measured in one spot. The measurements taken also assume the coating of the diamond on W is uniform across the square ( $1 \times 1 \text{ cm}^2$ ) which was not entirely true as seen in Figure 28. As a result, the same sample will not always give the same resistance reading when measured. Using a much larger surface area for measurements ( $5 \times 5 \text{ cm}^2$ ), increasing the nucleation density of nanodiamond and taking multiple readings in different spots of the sample to measure resistivity would improve the credibility of the results.

In conclusion, the results provide some insight into the surface of W however there also limitations which need to be considered when interpreting the data. Further work needs to be carried out with a range of samples at different stages in the fabrication procedure to determine which steps are responsible stripping the W layer of BDD.

### 3.12 Characterising the Lithiated sample using UV-Raman

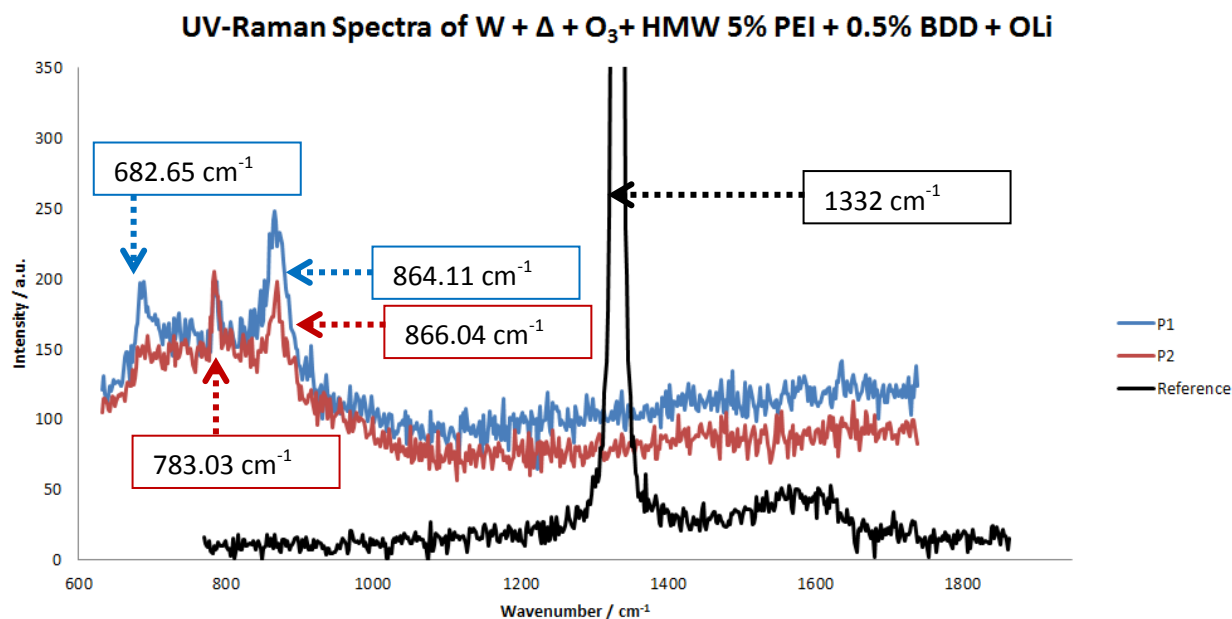


Figure 36. Raman spectra of lithiated sample seen in Figure 33 calibrated against a CVD diamond reference sample (phonon peak position  $1331.92 \text{ cm}^{-1}$ ).

Raman spectroscopy was used as the final technique to confirm if any nanodiamond was present on W. If so, a diamond peak surrounding  $1332 \text{ cm}^{-1}$  should be observed. It should be noted, techniques like IR spectrometry and XPS are typically used in identifying Li.

Multiple measurements were taken with the following points chosen as they gave the best signal to noise (S/N) ratio. A series of narrow sharp bands were detected at  $682.65 \text{ cm}^{-1}$  and  $864.11 \text{ cm}^{-1}$  at point 1 (P1) and at point 2 (P2) at  $783.03 \text{ cm}^{-1}$  and  $866.04 \text{ cm}^{-1}$ .<sup>127</sup> No diamond peak was observed at

1332  $\text{cm}^{-1}$  or single crystal graphite<sup>128</sup> at 1575  $\text{cm}^{-1}$  or other amorphous forms of graphite at 1355  $\text{cm}^{-1}$ . This was in agreement with the resistivity data as well as the SEM image of the lithiated sample previously seen in Figure 33 which showed very little coverage of nanodiamond. As the diamond coverage was not uniform it could be possible in actual fact the sample was mainly non-diamond and what was being detected was tungsten oxide. Unfortunately, no peaks could directly be linked to the stretches seen in Figure 37 below.

| Raman ( $\text{cm}^{-1}$ ) | Raman Groups & Assignment                                 |
|----------------------------|---|
| 949                        | $\nu_s$ (W=O ter.)  |
| 806                        | $\nu_a$ (W-O-W)   |
| 695                        | $\nu$ ( $\text{W}_2\text{O}_6$ & $\text{W}_3\text{O}_8$ ) |
| 518                        | O-Lattice   |
| 316                        | $\nu$ ( $\text{WO}_3$ )                                   |
| 256                        | $\nu$ (O-W-O)   |
|                            | $\delta$ (O-W-O)  |
| 194                        | W-W   |
| 131                        | ---   |

Figure 37.  $\text{WO}_3$  Raman bands. Adapted from reference 129.

Of the peaks described P2 is the closest in relation to the anti-symmetric W-O-W stretch. As described before, W exists as an oxide of which there are many. The oxide layer has been modified throughout the fabrication procedure which makes it extremely difficult to know what state the oxide resides in.

Spectra of other diamond samples have been given in the appendix which also shows no diamond is present. They also show peaks in similar regions as seen in Figure 36. One non-lithiated sample which had only been annealed also failed to show any conclusive results. More samples covering a wider range of the various fabrication steps need to be assessed using UV-Raman to accurately identify at what stage in the fabrication steps nanodiamond is being lost from the sample.

### 3.13 Summary

Based on the data gathered so far from the experiments that took place after field emission testing and assuming the FE kit was in perfect working order, it is strongly believed the during the annealing treatment and/or lithiation treatment most of the diamond was stripped of W leaving only the metallic W exposed. The surface roughness of W further exacerbates this problem due to the lack of overlap between diamond and metal. As annealing BDD to W via self-assembly has not been trialled before the

annealing conditions used, were based on trying different temperatures for different time durations to lock diamond down to W but more importantly also retain a fairly good nucleation density. The annealing step has not been optimized yet and the results seen so far suggest the nanodiamond being stripped off W is possibly due to excessive heating or being washed away as a result of weak carbide bonds between metal and BDD. Ultimately, no field emission was observed due to a lack of diamond coverage.

Varying annealing times with temperature could be a significant factor in understanding why there is variable diamond coverage in post annealed samples. Mrabet et al. extensively studied and depicted the phase changes of tungsten carbide (WC) to (W) using XRD analysis at annealing temperatures of 600–1100 °C under vacuum conditions.<sup>130</sup> A similar experimental setup could explain the temperature region at which W-C bonds deform to form metallic W and thus by process of elimination indicate what temperatures are not ideal for annealing. The data could be further complemented by SEM images of the surface as it is cycled through various temperatures.

# 4

## C Conclusion

---

The project came across a new discovery in the self-assembly of BDD to W. Treating the metal with heat or ozone or both enhances its oxide layer leading to successful self-assembly, previously not reported in literature. A rudimentary model has been depicted in Figure 30 which shows how treating the surface with atomic oxygen changes the surface chemistry by making the surface more polar thus making electrostatic attractions between the positive ends of PEI to the surface a more facile process. The fabrication procedure is the first of its kind and shows strong potential in becoming a transferable process for the self-assembly of diamond on other carbide forming materials such as molybdenum, Mo.

The project showed controlling the size and distribution of BDD is a challenge and trying to obtain uniformity is difficult to obtain using lab based equipment. Through the use of DLS and zeta potential measurements on BDD suspensions, it was shown multiple coatings of nanodiamond increased the surface coverage to a respectable 40% using a weakly concentrated diamond stock due to limited materials. It is very likely, through repeating milling and centrifuging steps a more uniformly disturbed and even coverage of nanodiamond can be achieved.

It is only fair to test the samples on the field emission kit once it is made sure there is sufficient nanodiamond present on the surface and the fabricated device has been fully characterised of its individual layers using the techniques represented in this project along with a few suggestions made in the future work section. This will allow a standard order of procedure to be developed and also no doubt reduce the number of speculations surrounding the fabrication procedure.

Overall, the project has provided a detailed platform on the electrostatic self-assembly of BDD to W, a previously untested form of assembly. The NEA effect of the BDD surface as a result of LiO termination still remains to be investigated however numerous advances and suggestions have been made to achieve the best possible nucleation density using self-assembly methods predominantly designed and optimized for Si or SiO<sub>2</sub> surfaces. The discussions proposed can most definitely form the basis of another project.

# 5

## Future Work

---

For starters, the diamond suspension stock was continuously being centrifuged to attain smaller sized nanodiamond particles (<300 nm) which was shared with another student. Over time, this meant the supply of BDD below <150 nm was close to being fully exhausted (see appendix) where hardly any coverage was being observed. Centrifuging the stock also meant the suspension was no longer at a concentration of 0.5% (w/v) but at a much lower value. Samples were also not made in batches but often in pairs as the conditions were continually being optimized. Improvements to this part of the fabrication step would be to have a very concentrated stock of BDD (10%) as opposed to 1% and centrifuging 20-30 ml of this stock which can be used for self-assembly. Alternatively, detonated diamond could be ordered and be doped with boron though in diffusion using a carrier gas such as  $B_2H_6$ . The particle size distribution of detonated diamond is much narrower which could be further optimized and controlled using sonication and centrifugation. The fabrication procedure could then be applied to this material.

Not all the fabrication steps where the surface of diamond was functionalized such as the lithiation step could be characterized in the given time frame. A detailed profile bearing information on the chemical composition of the sample is essential in confirming the reproducibility of such a complex fabrication assembly which is composed of multiple layers. For example, the experiments did not prove whether the surface was truly terminated with lithium oxygen groups. X-ray photoelectron spectroscopy (XPS) is a highly sensitive technique (ppm level detection) which is used to analyse the surface chemistry of thin films and layers (5-10 nm thick) and could be used to confirm the presence of

Li. The technique uses x-ray beams to irradiate the sample with high energy photons which result in core electrons of elements with atomic number above 3 leaving the surface and being detected. It is useful, not only for elemental analysis but also identifying how uniform the surface is of elementary composition.

The chosen route to stabilize nanodiamond in this project was electrostatic stabilization however another route, namely, steric stabilization also exists and remained largely unexplored in this project. Early stages of the project saw failed attempts of trying to encapsulate H-terminated BDD with PSS (polystyrenesulfonate) an anionic polymer, to form a stable suspension. It was then decided to move to a slightly simpler form of stabilization (electrostatic stabilization) as this would reduce the number of variables needed to be controlled and optimized i.e. polymer choice, pH, concentration etc. A simple experiment to identify which route gives the best stable suspension could be established using zeta potential measurements. Comparing and contrasting zeta potential values of BDD suspensions in aqueous media (pH 1-14) of both stabilisation routes would identify the pH regions where maximum stability is attained as well as the isoelectric point.

The saturation point of nucleation density could also be measured using SEM and possibly AFM as the BDD suspension used was only left to assemble to PEI on W for 30 minutes before being washed. Both routes of stabilization could also be compared. The experiment would involve creating duplicate samples of PEI on W followed by immersion in the BDD suspension for set time intervals i.e. 15 minutes. At each time interval the self-assembled sample would be removed and imaged using SEM. An experiment like this would identify the shortest time needed to self-assemble BDD to W which gives the best nucleation density. Eventually a saturation point would occur where increasing deposition time will have no effect on the nucleation density. The sample must also not be left to dry out as deposition through gravitational effects would otherwise be occurring. Height profiling using AFM could also show how smooth the surface is.

The surface roughness of W was suggested to be one of the reasons why a lack of surface coverage was observed. Previous self-assembly methods which have employed smooth surfaces such as Si or SiO<sub>2</sub> have seen particle densities magnitudes above what was seen in this project. Perhaps trialling a smoother surface such as bright tungsten with the optimized self-assembly procedure may result in an improvement.

## References

1. Diamond Unit Cell, [http://www.e6.com/wps/wcm/connect/E6\\_Content\\_EN/Home/The+power+of+supermaterials/Synthetic+diamonds+extreme+properties/](http://www.e6.com/wps/wcm/connect/E6_Content_EN/Home/The+power+of+supermaterials/Synthetic+diamonds+extreme+properties/), .
2. Eight Allotropes of Carbon, [http://upload.wikimedia.org/wikipedia/commons/f/f8/Eight\\_Allotropes\\_of\\_Carbon.png](http://upload.wikimedia.org/wikipedia/commons/f/f8/Eight_Allotropes_of_Carbon.png), .
3. M. Turner, Nat. News, 2011.
4. Joshi, Engineering Physics, Tata McGraw-Hill Education, 2010.
5. A. Richardson, Minerals, Capstone, 2001.
6. P. W. May, Endeavour, 1995, **19**, 101–106.
7. I. A. Dobrinets, V. G. Vins, and A. M. Zaitsev, HPHT-Treated Diamonds: Diamonds Forever, Springer Science & Business, 2013.
8. M. A. Prelas, G. Popovici, and L. K. Bigelow, Handbook of Industrial Diamonds and Diamond Films, CRC Press, 1997.
9. F.P. Bundy, The P,T Phase and Reaction diagram for elemental Carbon, 1979; J. Geophys. Res. 85 (B12) (1980) 6930., .
10. F. P. Bundy, H. T. Hall, H. M. Strong, and R. H. Wentorf, Nature, 1955, **176**, 51–55.
11. F. P. Bundy, H. T. Hall, H. M. Strong, and R. H. Wentorf, Nature, 1955, **176**, 51–55.
12. S. Matsumoto, Y. Sato, M. Tsutsumi, and N. Setaka, J. Mater. Sci., 1982, **17**, 3106., .
13. S. Matsumoto, Y. Sato, M. Kamo, and N. Setaka, Jpn. J. Appl. Phys. Part 2 - Lett., 1982, **21**, L183., .
14. CVD Diamond Film, <http://www.chm.bris.ac.uk/pt/diamond/image/cvdtop.gif>, .
15. M. Gabrysch, Electronic Properties Diamond, Ph.D. thesis (Uppsala University, Uppsala, Sweden, 2008), .
16. A. Kraft, Int. J. Electrochem. Sci., 2 (2007), pp. 355–385, .
17. M.A. Prelas, G.Popovici, L.K. Bigelow, Handbook of Industrial Diamonds and Diamond Films, CRC Press, 1997, .
18. H. Ibach and Lüth, Solid-state physics an introduction to principles of materials science, Springer, Berlin; New York, 2009.
19. S. Heyer, W. Janssen, S. Turner, Y.-G. Lu, W. S. Yeap, J. Verbeeck, K. Haenen, and A. Krueger, ACS Nano, 2014, 140416143010008.
20. L.S.Pan, D.R.Kania (1995). Diamond: Electronic Properties and Applications. New York: Kluwer Academic Publishers. 472., .
21. S. Karna and Y. Vohra, J. Mater. Sci. Res., 2013, **3**.
22. S. Koizumi, T. Teraji, and H. Kanda, Diam. Relat. Mater., 2000, **9**, 935–940.
23. K. Haenen, K. Meykens, M. Nesládek, G. Knuyt, L. M. Stals, T. Teraji, S. Koizumi, and E. Gheeraert, Diam. Relat. Mater., 2000, **9**, 952–955.
24. L. Diederich, O. Küttel, P. Ruffieux, T. Pillo, P. Aebi, and L. Schlapbach, Surf. Sci., 1998, **417**, 41–52.
25. V. Baranauskas, B. B. Li, A. Peterlevitz, M. C. Tosin, and S. F. Durrant, J. Appl. Phys., 1999, **85**, 7455–7458.
26. K. Okumura, J. Mort, and M. Machonkin, Appl. Phys. Lett., 1990, **57**, 1907–1909.
27. E. Lombardi, A. Mainwood, and K. Osuch, Phys. Rev. B, 2007, **76**.
28. M. Z. Othman, P. W. May, N. A. Fox, and P. J. Heard, Diam. Relat. Mater., 2014, **44**, 1–7.
29. S. Kajihara, A. Antonelli, J. Bernholc, and R. Car, Phys. Rev. Lett., 1991, **66**, 2010–2013.
30. S. Curat, H. Ye, O. Gaudin, R. B. Jackman, and S. Koizumi, J. Appl. Phys., 2005, **98**, 073701–073701–6.
31. F. A. M. Koeck, R. J. Nemanich, A. Lazea, and K. Haenen, Diam. Relat. Mater., 2009, **18**, 789–791.
32. R. Kalish, Appl. Surf. Sci., 1997, **117-118**, 558–569.
33. M. Restle, K. Bharuth-Ram, H. Quintel, C. Ronning, H. Hofsäss, S. G. Jahn, ISOLDE-Collaboration, and U. Wahl, Appl. Phys. Lett., 1995, **66**, 2733.

34. S. Praver, C. Uzan-Saguy, G. Braunstein, and R. Kalish, *Appl. Phys. Lett.*, 1993, **63**, 2502.
35. C. Nebel and J. Ristein, *Thin-Film Diamond I: (part of the Semiconductors and Semimetals Series)*, Academic Press, 2003.
36. M. Z. Othman, P. W. May, N. A. Fox, and P. J. Heard, *Diam. Relat. Mater.*, 2014, **44**, 1–7.
37. H. Yilmaz, B. R. Weiner, and G. Morell, *Diam. Relat. Mater.*, 2007, **16**, 840–844.
38. J. te Nijenhuis, G. Z. Cao, P. C. H. J. Smits, W. J. P. van Enkevort, L. J. Giling, P. F. A. Alkemade, M. Nesládek, and Z. Remeš, *Diam. Relat. Mater.*, 1997, **6**, 1726–1732.
39. G. Popovici, T. Sung, S. Khasawinah, M. A. Prelas, and R. G. Wilson, *J. Appl. Phys.*, 1995, **77**, 5625–5629.
40. W. Zhu, *Vacuum Microelectronics*, John Wiley & Sons, 2004.
41. C. Saby and P. Muret, *Diam. Relat. Mater.*, 2002, **11**, 851–855.
42. O. M. Küttel, O. Gröning, E. Schaller, L. Diederich, P. Gröning, and L. Schlapbach, *Diam. Relat. Mater.*, 1996, **5**, 807–811.
43. J. B. Cui, J. Ristein, and L. Ley, *Phys. Rev. Lett.*, 1998, **81**, 429–432.
44. J. F. Prins, *Semicond. Sci. Technol.*, 2003, **18**, S125.
45. T. Martin, *Lithium-oxygen termination as a negative electron affinity surface on diamond: a computational and photoemission study*, PhD thesis, University of Bristol, (201), .
46. R. S. Sussmann, *CVD diamond for electronic devices and sensors*, J. Wiley, Chichester, U.K., 2009.
47. S.-G. Ri, C. E. Nebel, D. Takeuchi, B. Rezek, N. Tokuda, S. Yamasaki, and H. Okushi, *Diam. Relat. Mater.*, 2006, **15**, 692–697.
48. F. Maier, J. Ristein, and L. Ley, *Phys. Rev. B*, 2001, **64**.
49. T. Ando, K. Yamamoto, M. Ishii, M. Kamo, and Y. Sato, *J. Chem. Soc. Faraday Trans.*, 1993, **89**, 3635.
50. H. Notsu, I. Yagi, T. Tatsuma, D. A. Tryk, and A. Fujishima, *Electrochem. Solid-State Lett.*, 1999, **2**, 522–524.
51. C. K. Fink and S. J. Jenkins, *J. Phys. Condens. Matter*, 2009, **21**, 264010.
52. D. Petrini and K. Larsson, *J. Phys. Chem. C*, 2007, **111**, 795–801.
53. K. M. O'Donnell, T. L. Martin, N. A. Fox, and D. Cherns, *MRS Proc.*, 2011, **1282**.
54. R.H. Fowler and L.W. Nordheim, 'Electron Emission in Intense Electric Fields,' *Proc. Roy. Soc. (London)*, vol. A119, pp. 173-181, 1928, .
55. Y. Cheng, O. Zhou, *C. R. Physique 4* (2003), .
56. R. G. Forbes and J. H. B. Deane, *Proc. R. Soc. Math. Phys. Eng. Sci.*, 2011, **467**, 2927–2947.
57. B. Van Zeghbroeck, *Principles of Semiconductor Devices*, University of Colorado, 2004, .
58. R. G. Forbes, *J. Vac. Sci. Technol. B Microelectron. Nanometer Struct.*, 1999, **17**, 526.
59. T. Vecchione, *Gallium Arsenide Photo-field Emission*, ProQuest, 2009.
60. Y. Gogotsi and V. Presser, *Carbon Nanomaterials*, Second Edition, CRC Press, 2013.
61. Z. L. Wang and C. Hui, Eds., *Electron microscopy of nanotubes*, Kluwer Academic Publishers, Boston, 2003.
62. W.-P. Kang, A. Wisitsora-at, J. L. Davidson, and D. V. Kerns, *IEEE Electron Device Lett.*, 1998, **19**, 379–381.
63. Gomer, Robert. *Field emission and field ionization*. Vol. 34. Cambridge, MA: Harvard University Press, 1961., .
64. S. A. Furkert, A. Wotherspoon, D. Cherns, N. A. Fox, G. M. Fuge, P. J. Heard, and S. P. Lansley, *Appl. Phys. Lett.*, 2007, **90**, 242109.
65. N. Fox, T. L. Martin, and K. M. O'Donnell, 2013.
66. J.S. Lapington, P.W. May, N.A. Fox, J. Howorth, JA. Milnes, 'Diamond dynodes create new breed of photon detectors', *Laser Focus World* (Sept 2008), .
67. Lithiated Nanoparticles, [http://www.bitworks-engineering.co.uk/Welcome\\_files/nano4energy2010.pdf](http://www.bitworks-engineering.co.uk/Welcome_files/nano4energy2010.pdf), .
68. W. Zhu, *Science*, 1998, **282**, 1471–1473.
69. R. K. Iler, *J. Colloid Interface Sci.*, 1966, **21**, 569–594.
70. Decher, G.; Hong, J. D. *Makromol. Chem. Macromol. Symp.* 1991, 46, 321., .
71. F. Caruso, H. Lichtenfeld, M. Giersig, and H. Möhwald, *J. Am. Chem. Soc.*, 1998, **120**, 8523–8524.

72. H. Ahrens, K. Büscher, D. Eck, S. Förster, C. Luap, G. Papastavrou, J. Schmitt, R. Steitz, and C. a. Helm, *Macromol. Symp.*, 2004, **211**, 93–106.
73. E.R.Tofts, Electrostatic Self-Assembly of Nanodiamond Nucleation Layers used in the production of X-Ray Refractive Lenses. Masters thesis, University of Bristol, (2013), .
74. J. Hees, A. Kriele, and O. A. Williams, *Chem. Phys. Lett.*, 2011, **509**, 12–15.
75. F. Rossi, *Theory of semiconductor quantum devices microscopic modeling and simulation strategies*, Springer, Berlin; London, 2010.
76. T.Martin, Lithium-oxygen termination as a negative electron affinity surface on diamond: a computational and photoemission study, PhD thesis, University of Bristol, (201), .
77. P.Walker, W.H.Tarn, *CRC Handbook of Metal Etchants*, CRC Press, 1990, .
78. E.R.Tofts, Electrostatic Self-Assembly of Nanodiamond Nucleation Layers used in the production of X-Ray Refractive Lenses. Masters thesis, University of Bristol, (2013), .
79. L. A. Hockett and S. E. Creager, *Rev. Sci. Instrum.*, 1993, **64**, 263.
80. J. P. Ibe, *J. Vac. Sci. Technol. Vac. Surf. Films*, 1990, **8**, 3570.
81. T. F. Baumann, J. Biener, Y. M. Wang, S. O. Kucheyev, E. J. Nelson, J. H. Satcher,, J. W. Elam, M. J. Pellin, and A. V. Hamza, *Chem. Mater.*, 2006, **18**, 6106–6108.
82. J. R. Vig, *J. Vac. Sci. Technol. Vac. Surf. Films*, 1985, **3**, 1027.
83. <http://www.jelight.com/uv-ozone-cleaning.html>, .
84. V.Y.Ivanov et al., *High Temperature Oxidation protection of Tungsten*, 1968, pg.22, .
85. J. P. Bonnet, J. Nowotny, M. Onillon, and I. Sikora, *Oxid. Met.*, 1979, **13**, 273–282.
86. A.C.Jones, M.L.Hitchman, *Chemical Vapour Deposition, Precursors, Processes and Applications*, pg.464, .
87. Spier, Henri Louis. 1962. *Influence of chemical additions on the reduction of tungsten oxides*. Eindhoven: Philips Research Laboratories., .
88. B. D. Thoms, M. S. Owens, J. E. Butler, and C. Spiro, *Appl. Phys. Lett.*, 1994, **65**, 2957.
89. P. K. Baumann, T. P. Humphreys, and R. J. Nemanich, *MRS Proc.*, 2011, **339**.
90. V. Pichot, M. Comet, E. Fousson, C. Baras, A. Senger, F. Le Normand, and D. Spitzer, *Diam. Relat. Mater.*, 2008, **17**, 13–22.
91. C. Popov, W. Kulisch, S. Bliznakov, G. Ceccone, D. Gilliland, L. Sirghi, and F. Rossi, *Diam. Relat. Mater.*, 2008, **17**, 1229–1234.
92. P. E. Pehrsson and T. W. Mercer, *Surf. Sci.*, 2000, **460**, 49–66.
93. Sigma-Aldrich, *Specification Sheet*, 482595 (2007), .
94. P. W. May, *Philos. Trans. R. Soc. Math. Phys. Eng. Sci.*, 2000, **358**, 473–495.
95. Boiling Point of PEI, CAS No. 9002-98-6, [http://www.chemicalbook.com/ChemicalProductProperty\\_US\\_CB9162514.aspx](http://www.chemicalbook.com/ChemicalProductProperty_US_CB9162514.aspx), .
96. Goeting, CH, Marken, F, Gutierrez-Sosa, A et al., (1999). Boron-doped diamond electrodes: Growth, surface characterisation and sono-electrochemical applications. *NEW DIAMOND AND FRONTIER CARBON TECHNOLOGY*, 9 (3), 207-228., .
97. H. O. Pierson, *Handbook of chemical vapor deposition (CVD): principles, technology, and applications*, Noyes Publications, Park Ridge, N.J., U.S.A, 1992.
98. Kittel, Charles (1995). *Introduction to Solid State Physics* (7 ed.). Wiley-India., .
99. DLS Manual, Chapter 14, <http://www.chem.uci.edu/~dmitryf/manuals/Size,%20molecular%20weight%20and%20zeta%20potential%20theory.pdf>, .
100. Hydrodynamic Radius, <http://www.silver-colloids.com/Papers/hydrodynamic-radius.pdf>, .
101. Zeta Nano Series Technical Note, MAK654-01, Malvern Instruments, UK, .
102. W. Yu and H. Xie, *J. Nanomater.*, 2012, **2012**, 1–17.
103. Zeta Potential Tutorial Sheet, <http://www.colloidal-dynamics.com/docs/CDEITut1.pdf>, .
104. Dr. Charl FJ Faul Research Group, *Manual for Four Probes Resistance Measurement Setup*, University of Bristol, .

105. P. M. Koinkar, R. V. Kashid, S. S. Patil, D. S. Joag, R. Murakami, and M. A. More, *IEEE Trans. Nanotechnol.*, 2013, **12**, 911–914.
106. Field Emission model, <http://cdn.phys.org/newman/gfx/news/2013/atomiclevels.png>, .
107. P. W. May, W. J. Ludlow, M. Hannaway, P. J. Heard, J. A. Smith, and K. N. Rosser, *Diam. Relat. Mater.*, 2008, **17**, 105–117.
108. W. L. Wang, M. C. Polo, G. Sánchez, J. Cifre, and J. Esteve, *J. Appl. Phys.*, 1996, **80**, 1846.
109. [http://mmrc.caltech.edu/PD\\_Expert/Malvern%20notes/Calculating%20volume%20distributions%20from%20DLS%20data.pdf](http://mmrc.caltech.edu/PD_Expert/Malvern%20notes/Calculating%20volume%20distributions%20from%20DLS%20data.pdf), .
110. DLS Technial Note, MAK656-01, Malvern Instruments, UK, .
111. J.-P. Boudou, P. A. Curmi, F. Jelezko, J. Wrachtrup, P. Aubert, M. Sennour, G. Balasubramanian, R. Reuter, A. Thorel, and E. Gaffet, *Nanotechnology*, 2009, **20**, 235602.
112. G. A. Parks, *Chem. Rev.*, 1965, **65**, 177–198.
113. R. Compton, *Electrode Kinetics: Reactions*, 1st Edn, pg.83, .
114. Y. Nishi and R. Doering, Eds., *Handbook of semiconductor manufacturing technology*, Marcel Dekker, New York, 2000.
115. J.-F. Berret, P. Herve, M. Morvan, K. Yokota, M. Destarac, J. Oberdisse, I. Grillo, and R. Schweins, *ArXivcond-Mat0501083*, 2005.
116. Y. Morita, T. Takimoto, H. Yamanaka, K. Kumekawa, S. Morino, S. Aonuma, T. Kimura, and N. Komatsu, *Small*, 2008, **4**, 2154–2157.
117. L.-Y. Chang, E. Ōsawa, and A. S. Barnard, *Nanoscale*, 2011, **3**, 958.
118. W. Zhu, G. P. Kochanski, S. Jin, and L. Seibles, *J. Appl. Phys.*, 1995, **78**, 2707.
119. M. W. Geis, J. C. Twichell, N. N. Efremow, K. Krohn, and T. M. Lyszczarz, *Appl. Phys. Lett.*, 1996, **68**, 2294.
120. K. Wu, E. G. Wang, Z. X. Cao, Z. L. Wang, and X. Jiang, *J. Appl. Phys.*, 2000, **88**, 2967.
121. D. Pradhan and I. N. Lin, *ACS Appl. Mater. Interfaces*, 2009, **1**, 1444–1450.
122. R. Cai, G. Chen, X. Song, G. Xing, Z. Feng, and D. He, *Chin. Sci. Bull.*, 2003, **48**, 1934–1937.
123. D. J. Kraft, R. Ni, F. Smallenburg, M. Hermes, K. Yoon, D. A. Weitz, A. van Blaaderen, J. Groenewold, M. Dijkstra, and W. K. Kegel, *Proc. Natl. Acad. Sci.*, 2012, **109**, 10787–10792.
124. D. C. Giancoli, *Physics: principles with applications*, Prentice Hall, Englewood Cliffs, N.J, 4th ed., 1995.
125. G. Herlem, B. Lakard, M. Herlem, and B. Fahys, *J. Electrochem. Soc.*, 2001, **148**, E435.
126. M. Gillet, R. Delamare, and E. Gillet, *Eur. Phys. J. D*, 2005, **34**, 291–294.
127. A. C. Ferrari and J. Robertson, *Philos. Trans. R. Soc. Math. Phys. Eng. Sci.*, 2004, **362**, 2477–2512.
128. F. Tuinstra, *J. Chem. Phys.*, 1970, **53**, 1126.
129. Díaz-Reyes, J.; Dorantes-García, V.; Pérez-Benítez, A.; Balderas-López, J. A.. 2008. Obtaining of films of tungsten trioxide (WO<sub>3</sub>) by resistive heating of a tungsten filament. *Superficies y vacío* 21: 12-17., .
130. S. E. Mrabet, M. D. Abad, C. López-Cartes, D. Martínez-Martínez, and J. C. Sánchez-López, *Plasma Process. Polym.*, 2009, **6**, S444–S449.

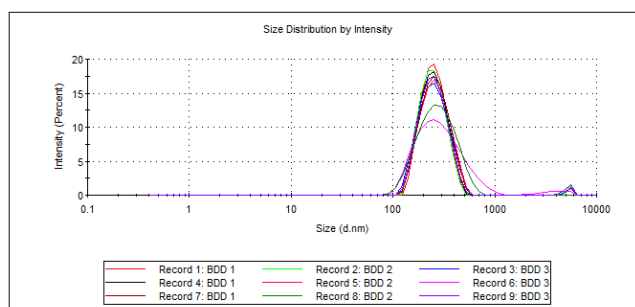
## Appendices

### 1. DLS data for unwashed BDD at different absorption coefficients.

|  |                                 |
|--|---------------------------------|
| Temperature (°C): 25.0                                 | Duration Used (s): 60           |
| Count Rate (kcps): 336.2                               | Measurement Position (mm): 3.00 |
| Cell Description: Disposable low volume cuvette (50... | Attenuator: 8                   |

|                                | Size (d.nm):         | % Number: | St Dev (d.nm): |
|--------------------------------|----------------------|-----------|----------------|
| <b>Z-Average (d.nm): 260.1</b> | <b>Peak 1:</b> 215.4 | 100.0     | 65.37          |
| <b>PdI: 0.219</b>              | <b>Peak 2:</b> 5405  | 0.0       | 649.8          |
| <b>Intercept: 0.872</b>        | <b>Peak 3:</b> 0.000 | 0.0       | 0.000          |

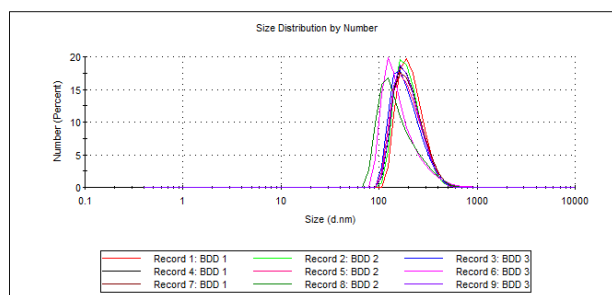
Result quality : **Good**



|  |                                 |
|--|---------------------------------|
| Temperature (°C): 25.0                                 | Duration Used (s): 60           |
| Count Rate (kcps): 336.2                               | Measurement Position (mm): 3.00 |
| Cell Description: Disposable low volume cuvette (50... | Attenuator: 8                   |

|                                | Size (d.nm):         | % Number: | St Dev (d.nm): |
|--------------------------------|----------------------|-----------|----------------|
| <b>Z-Average (d.nm): 260.1</b> | <b>Peak 1:</b> 215.4 | 100.0     | 65.37          |
| <b>PdI: 0.219</b>              | <b>Peak 2:</b> 5405  | 0.0       | 649.8          |
| <b>Intercept: 0.872</b>        | <b>Peak 3:</b> 0.000 | 0.0       | 0.000          |

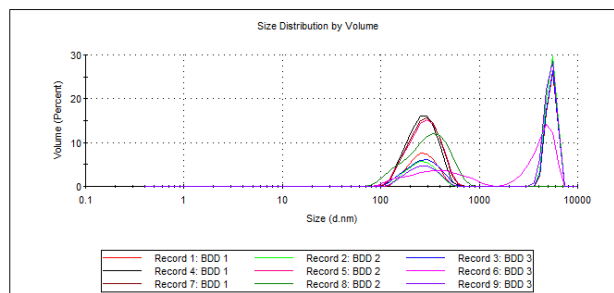
Result quality : **Good**



|  |                                 |
|--|---------------------------------|
| Temperature (°C): 25.0                                 | Duration Used (s): 60           |
| Count Rate (kcps): 336.2                               | Measurement Position (mm): 3.00 |
| Cell Description: Disposable low volume cuvette (50... | Attenuator: 8                   |

|                                | Size (d.nm):         | % Number: | St Dev (d.nm): |
|--------------------------------|----------------------|-----------|----------------|
| <b>Z-Average (d.nm): 260.1</b> | <b>Peak 1:</b> 215.4 | 100.0     | 65.37          |
| <b>PdI: 0.219</b>              | <b>Peak 2:</b> 5405  | 0.0       | 649.8          |
| <b>Intercept: 0.872</b>        | <b>Peak 3:</b> 0.000 | 0.0       | 0.000          |

Result quality : **Good**

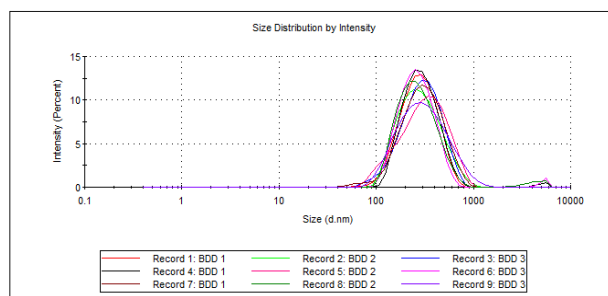


Size distribution by intensity, volume and number for unwashed diamond at an absorption coefficient of 0.01

Temperature (°C): 25.0      Duration Used (s): 60  
 Count Rate (kcps): 329.6      Measurement Position (mm): 3.00  
 Cell Description: Disposable low volume cuvette (50...      Attenuator: 8

|                                | Size (d.nm):         | % Number: | St Dev (d.nm): |
|--------------------------------|----------------------|-----------|----------------|
| <b>Z-Average (d.nm): 259.9</b> | <b>Peak 1:</b> 66.16 | 48.4      | 14.13          |
| <b>Pdi: 0.204</b>              | <b>Peak 2:</b> 187.0 | 51.6      | 99.53          |
| <b>Intercept: 0.859</b>        | <b>Peak 3:</b> 0.000 | 0.0       | 0.000          |

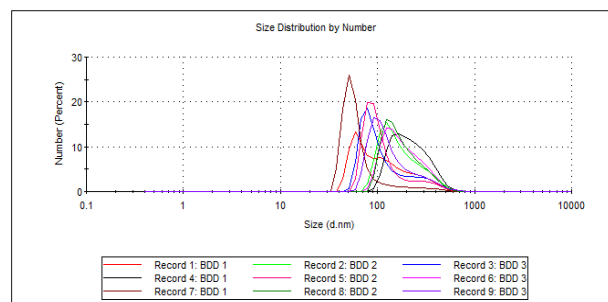
Result quality : Good



Temperature (°C): 25.0      Duration Used (s): 60  
 Count Rate (kcps): 329.6      Measurement Position (mm): 3.00  
 Cell Description: Disposable low volume cuvette (50...      Attenuator: 8

|                                | Size (d.nm):         | % Number: | St Dev (d.nm): |
|--------------------------------|----------------------|-----------|----------------|
| <b>Z-Average (d.nm): 259.9</b> | <b>Peak 1:</b> 66.16 | 48.4      | 14.13          |
| <b>Pdi: 0.204</b>              | <b>Peak 2:</b> 187.0 | 51.6      | 99.53          |
| <b>Intercept: 0.859</b>        | <b>Peak 3:</b> 0.000 | 0.0       | 0.000          |

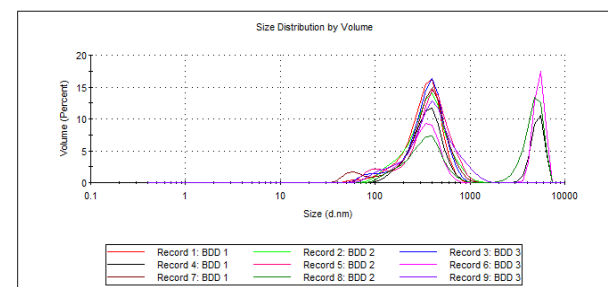
Result quality : Good



Temperature (°C): 25.0      Duration Used (s): 60  
 Count Rate (kcps): 329.6      Measurement Position (mm): 3.00  
 Cell Description: Disposable low volume cuvette (50...      Attenuator: 8

|                                | Size (d.nm):         | % Number: | St Dev (d.nm): |
|--------------------------------|----------------------|-----------|----------------|
| <b>Z-Average (d.nm): 259.9</b> | <b>Peak 1:</b> 66.16 | 48.4      | 14.13          |
| <b>Pdi: 0.204</b>              | <b>Peak 2:</b> 187.0 | 51.6      | 99.53          |
| <b>Intercept: 0.859</b>        | <b>Peak 3:</b> 0.000 | 0.0       | 0.000          |

Result quality : Good

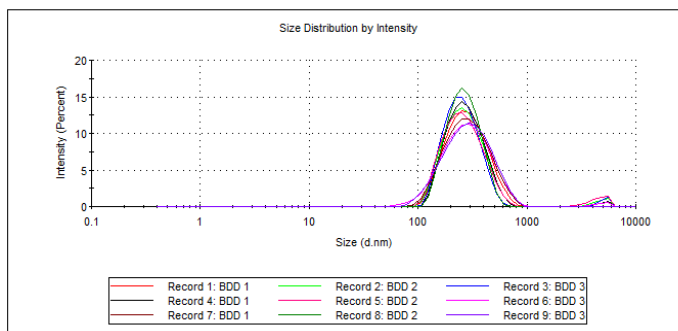


Size distribution by intensity, volume and number for unwashed diamond at an absorption coefficient of 0.5

Temperature (°C): 24.9      Duration Used (s): 60  
 Count Rate (kcps): 342.7      Measurement Position (mm): 3.00  
 Cell Description: Disposable low volume cuvette (50...      Attenuator: 8

|                                | Size (d.nm):         | % Number: | St Dev (d.nm): |
|--------------------------------|----------------------|-----------|----------------|
| <b>Z-Average (d.nm):</b> 253.5 | <b>Peak 1:</b> 224.7 | 100.0     | 106.3          |
| <b>Pd:</b> 0.146               | <b>Peak 2:</b> 0.000 | 0.0       | 0.000          |
| <b>Intercept:</b> 0.868        | <b>Peak 3:</b> 0.000 | 0.0       | 0.000          |

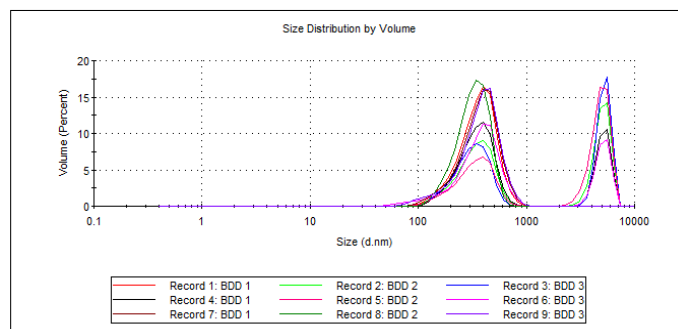
**Result quality : Good**



Temperature (°C): 24.9      Duration Used (s): 60  
 Count Rate (kcps): 342.7      Measurement Position (mm): 3.00  
 Cell Description: Disposable low volume cuvette (50...      Attenuator: 8

|                                | Size (d.nm):         | % Number: | St Dev (d.nm): |
|--------------------------------|----------------------|-----------|----------------|
| <b>Z-Average (d.nm):</b> 253.5 | <b>Peak 1:</b> 224.7 | 100.0     | 106.3          |
| <b>Pd:</b> 0.146               | <b>Peak 2:</b> 0.000 | 0.0       | 0.000          |
| <b>Intercept:</b> 0.868        | <b>Peak 3:</b> 0.000 | 0.0       | 0.000          |

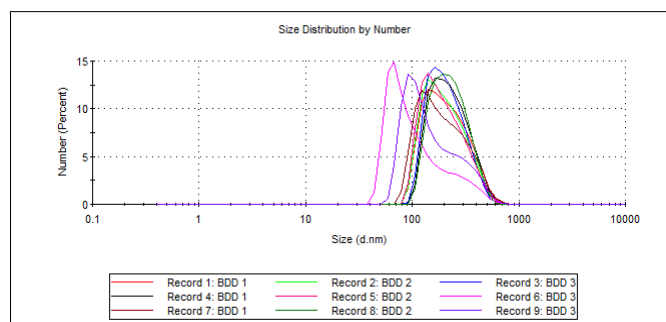
**Result quality : Good**



Temperature (°C): 24.9      Duration Used (s): 60  
 Count Rate (kcps): 342.7      Measurement Position (mm): 3.00  
 Cell Description: Disposable low volume cuvette (50...      Attenuator: 8

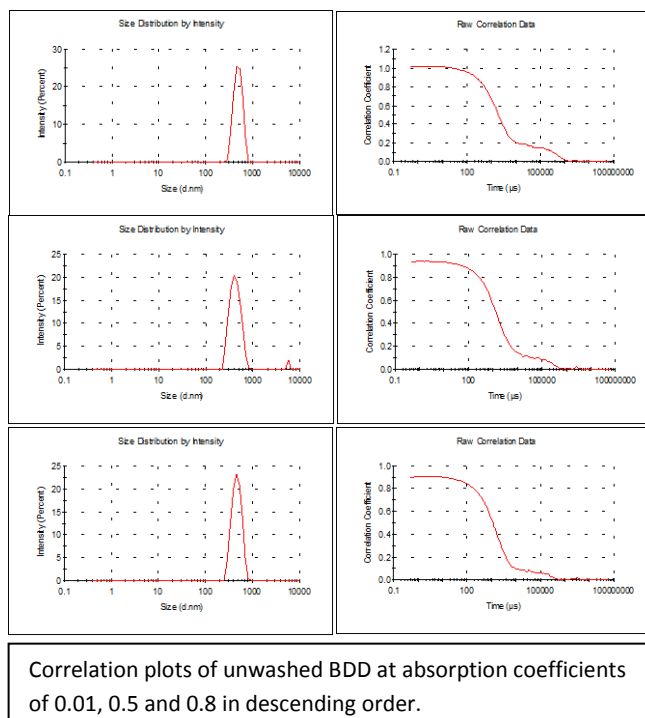
|                                | Size (d.nm):         | % Number: | St Dev (d.nm): |
|--------------------------------|----------------------|-----------|----------------|
| <b>Z-Average (d.nm):</b> 253.5 | <b>Peak 1:</b> 224.7 | 100.0     | 106.3          |
| <b>Pd:</b> 0.146               | <b>Peak 2:</b> 0.000 | 0.0       | 0.000          |
| <b>Intercept:</b> 0.868        | <b>Peak 3:</b> 0.000 | 0.0       | 0.000          |

**Result quality : Good**

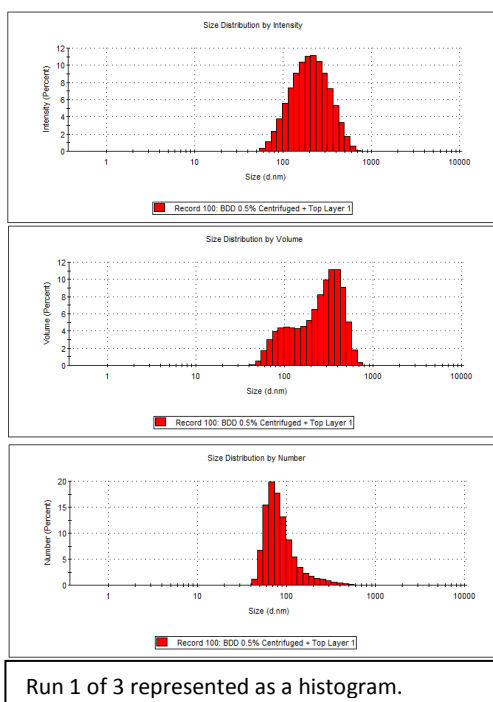


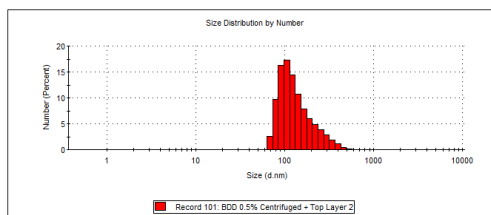
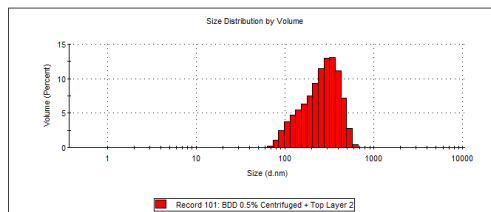
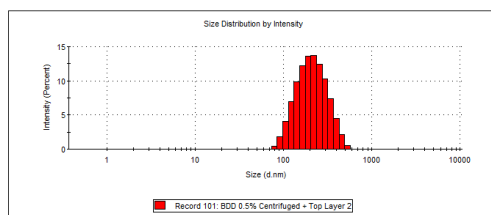
Size distribution by intensity, volume and number for unwashed diamond at an absorption coefficient of 0.8

## 2. Correlation plots of unwashed BDD

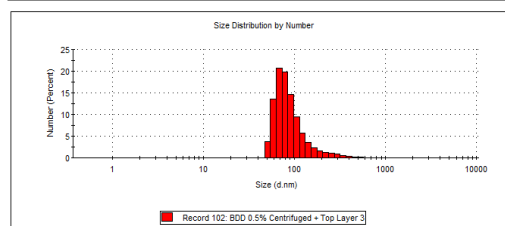
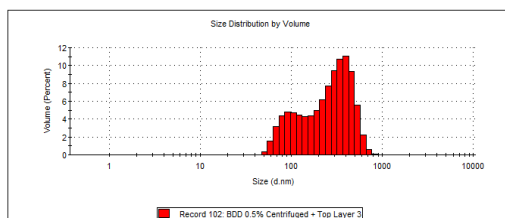
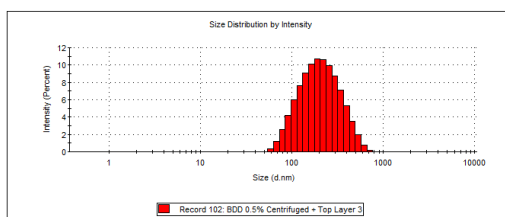


## 3. Size distributions by intensity, number and volume of sonicated and centrifuged acid washed BDD suspension



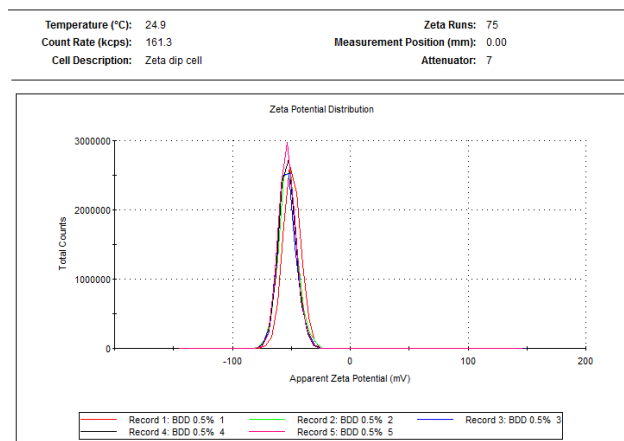


Run 2 of 3 represented as a histogram.



Run 3 of 3 represented as a histogram.

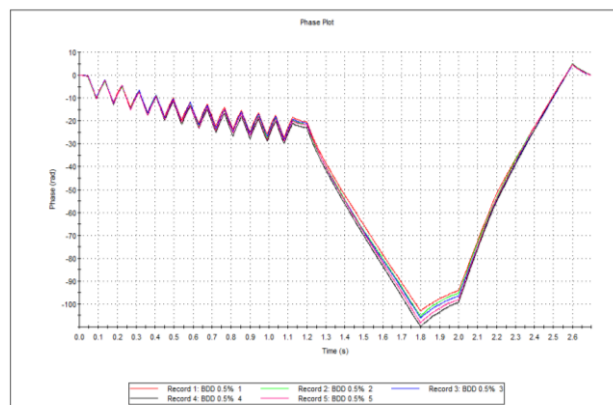
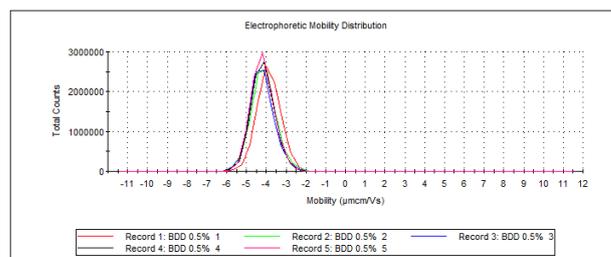
## 4. Supplementary Zeta Potential Information



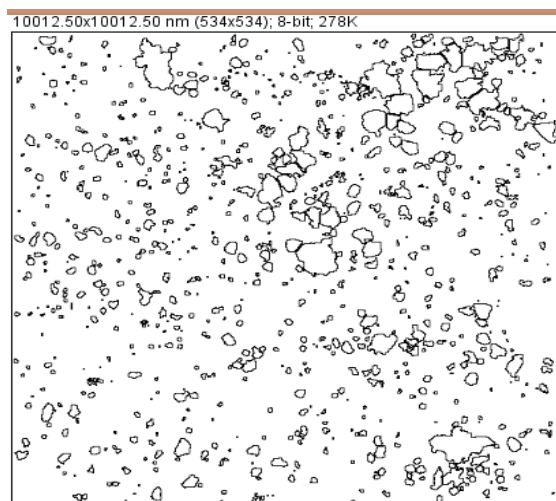
Temperature (°C): 24.9      Zeta Runs: 75  
 Count Rate (kcps): 161.3      Measurement Position (mm): 0.00  
 Cell Description: Zeta dip cell      Attenuator: 7

|  | Mean ( $\mu\text{mcm/Vs}$ ) | Area (%) | St Dev ( $\mu\text{mcm/Vs}$ ) |
|--|-----------------------------|----------|-------------------------------|
| Mobility ( $\mu\text{mcm/Vs}$ ): -3.875      | Peak 1: -3.88               | 100.0    | 0.582                         |
| Mobility Dev. ( $\mu\text{mcm/Vs}$ ): 0.5818 | Peak 2: 0.00                | 0.0      | 0.00                          |
| Conductivity (mS/cm): 0.352                  | Peak 3: 0.00                | 0.0      | 0.00                          |

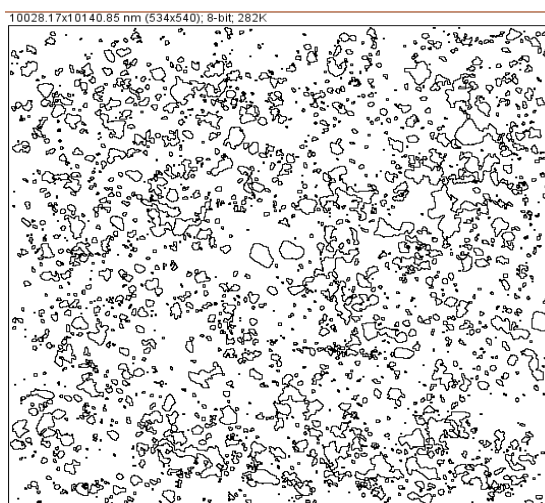
Result quality : Good



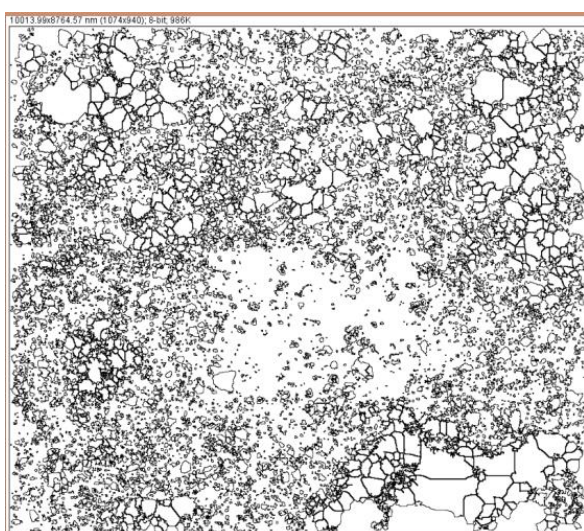
## 5. Fractional Coverage Images



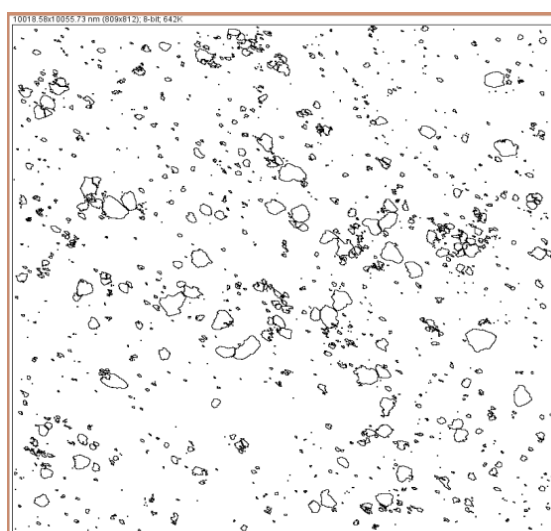
**W +  $\Delta$  + O<sub>3</sub> + 0.5% HMW PEI + 0.5% BDD (A)**



**W +  $\Delta$  + O<sub>3</sub> + 5% HMW PEI + 0.5% BDD (B)**



**W + O<sub>3</sub> + 0.5% LMW PEI + 0.5% BDD (C)**

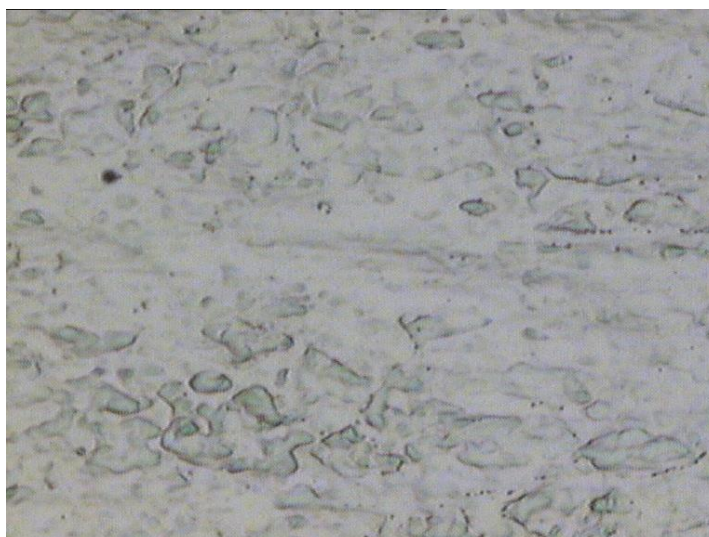


**W + O<sub>3</sub> + 5% LMW PEI + 0.5% BDD (D)**

6. Optical images of bare W surface

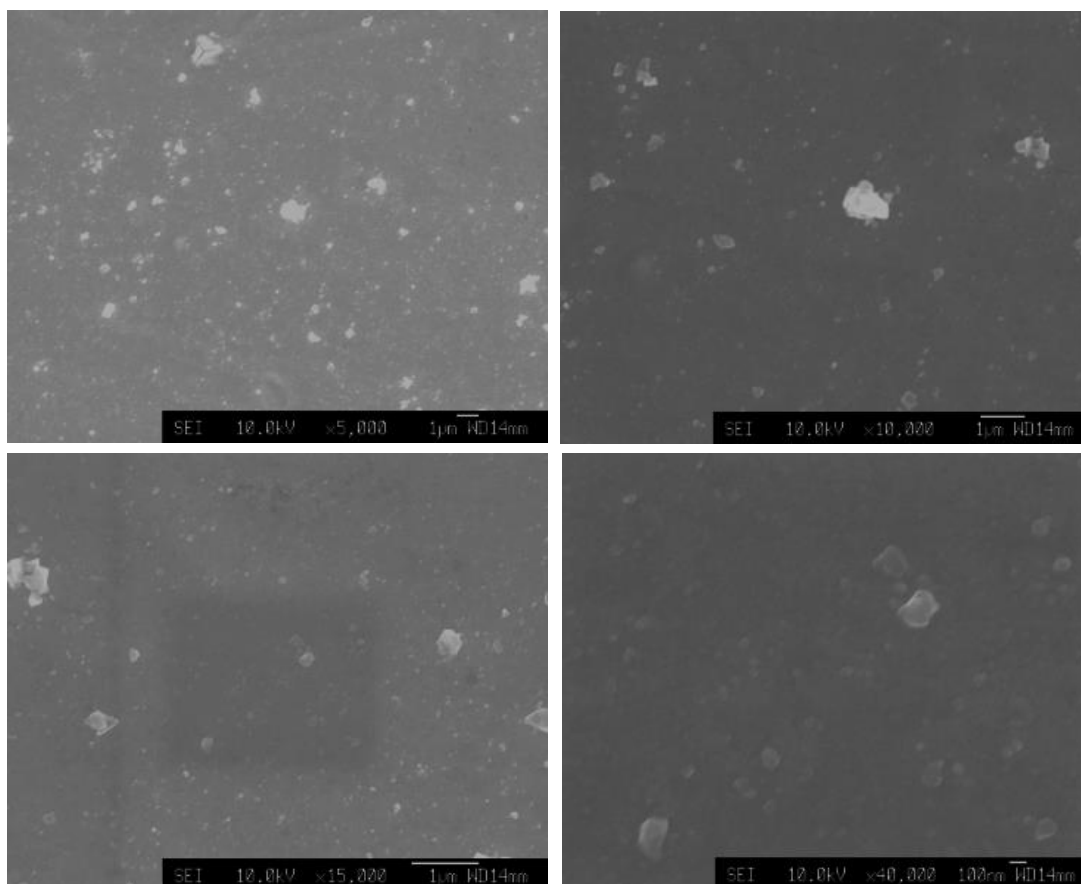


Optical Image of bare W (Mag. at x5)

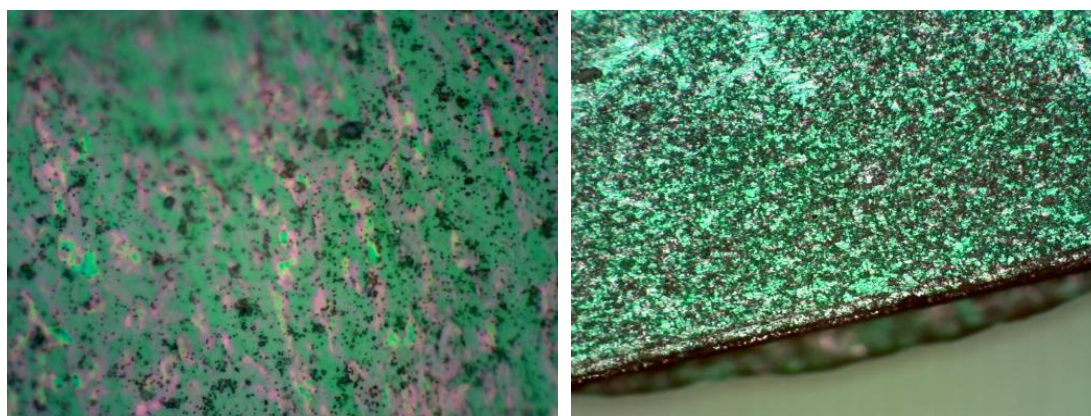


Optical Image of bare W (Mag. at x100)

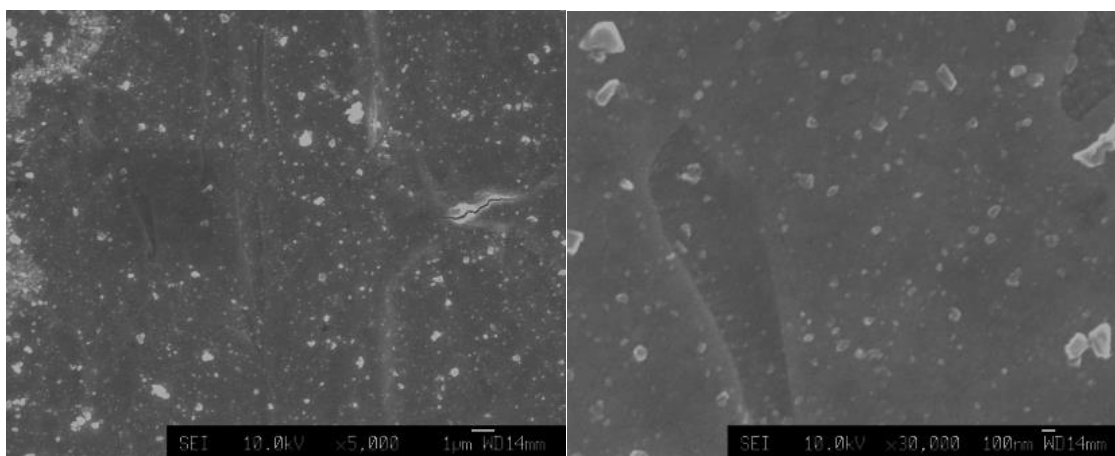
## 7. Optical and SEM images of self-assembled samples



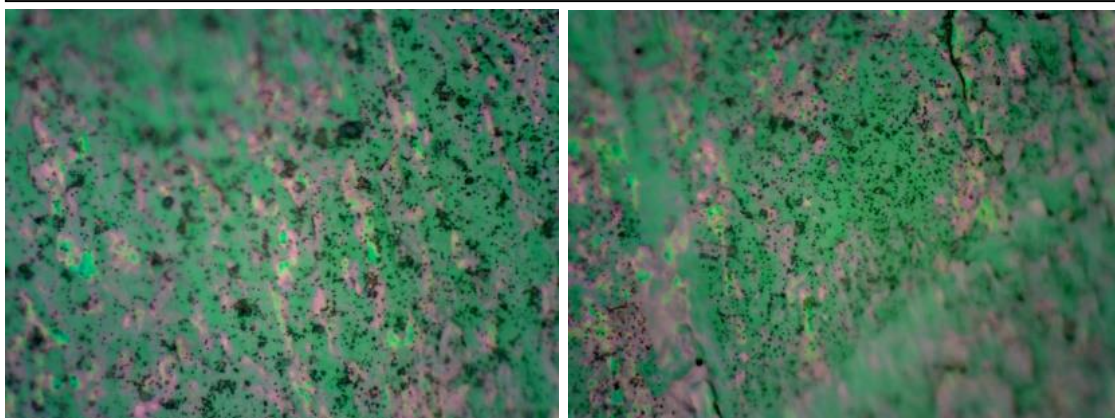
SEM Images of W +  $\Delta$  + 5% LMW PEI + 0.5% BDD



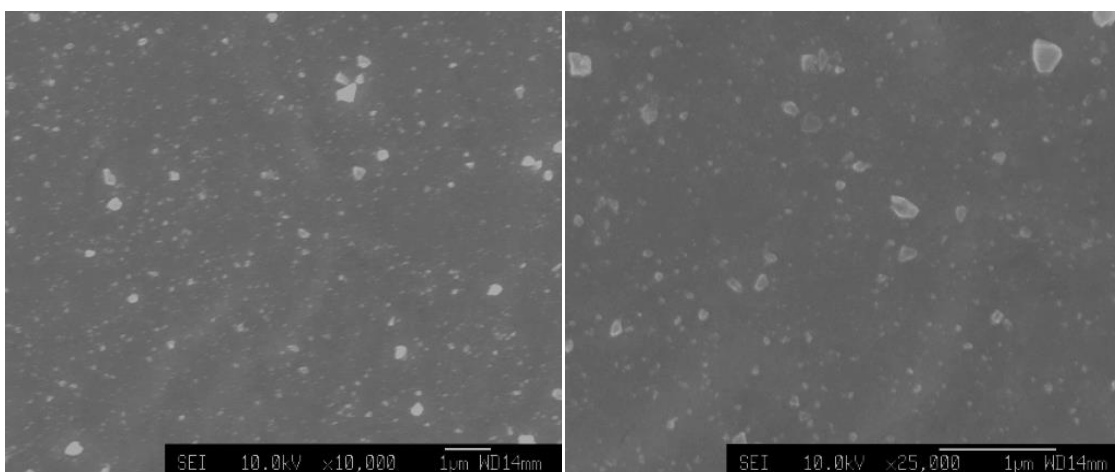
Optical Images of W +  $\Delta$  + 5% LMW PEI + 0.5% BDD (Mag. at  $\times 100$  (left) and  $\times 10$  (right))



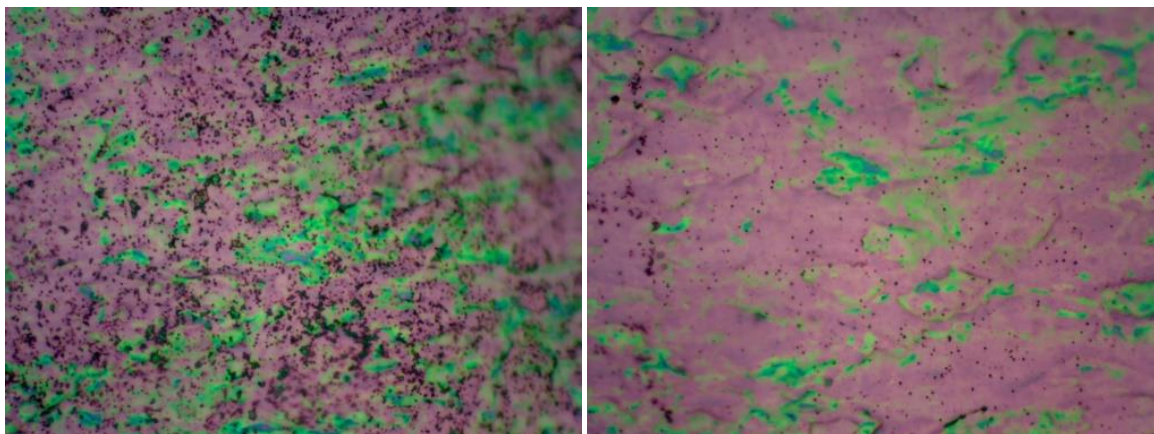
**SEM Images W +  $\Delta$  + 0.5% LMW PEI + 0.5% BDD**



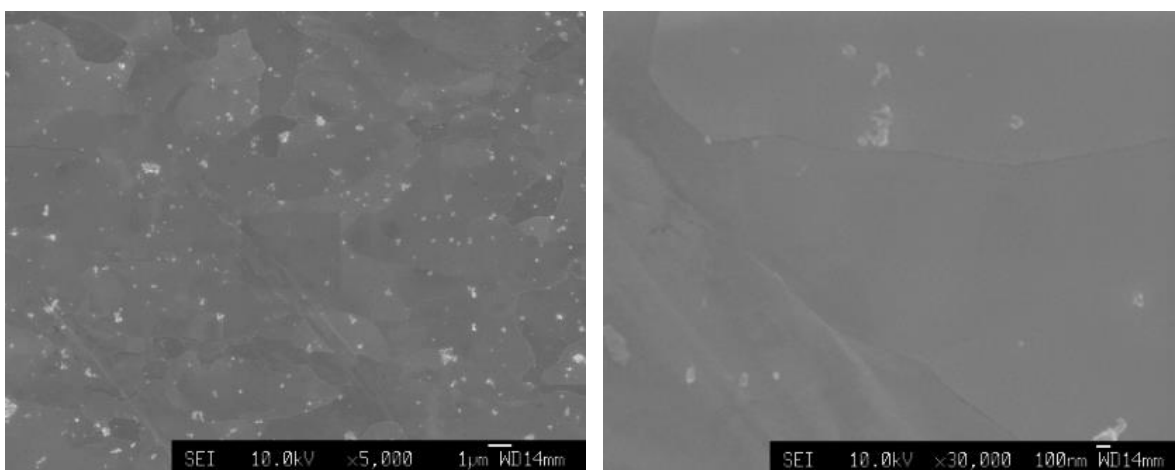
**Optical Images W +  $\Delta$  + 0.5% LMW PEI + 0.5% BDD (Mag. at x100)**



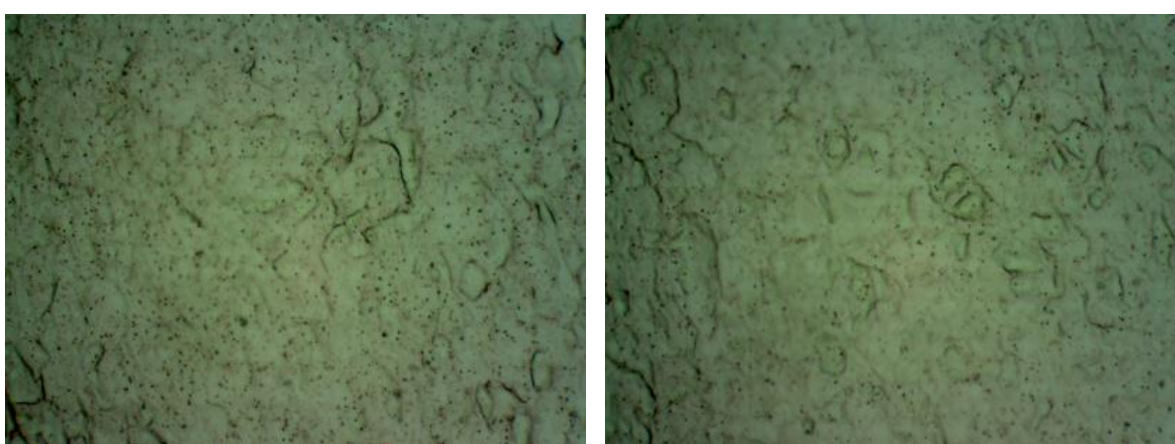
**SEM Images W + O<sub>3</sub> + 0.5% LMW PEI + 0.5% BDD**



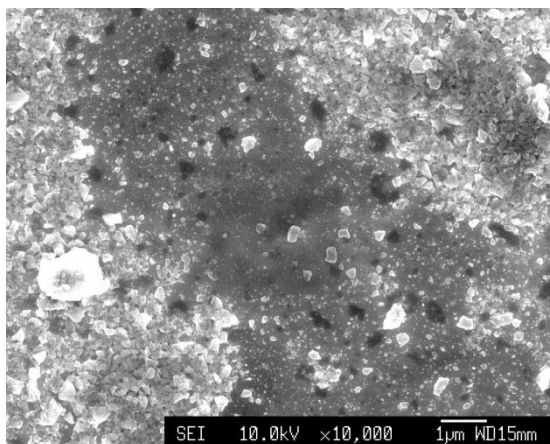
Optical images W + O<sub>3</sub> + 0.5% LMW PEI + 0.5% BDD



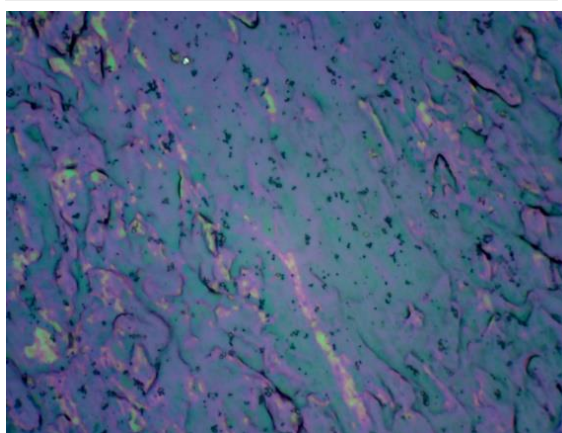
SEM Images W + O<sub>3</sub> + 0.5% HMW PEI + 0.5% BDD



Optical images W + O<sub>3</sub> + 0.5% HMW PEI + 0.5% BDD



SEM Images W + Δ + 0.5% HMW PEI + 0.5% BDD

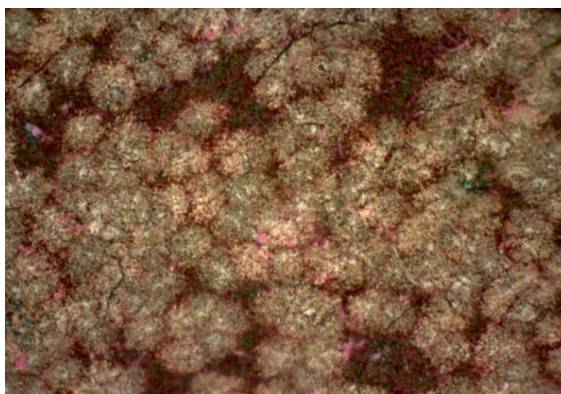


SEM Images W + Δ + 0.5% HMW PEI + 0.5% BDD

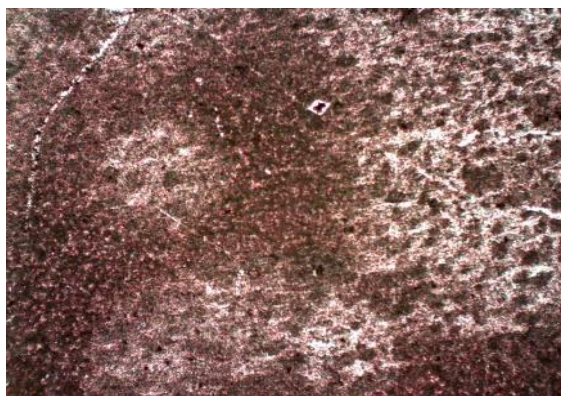
## 8. Optical images of lithiated samples



Optical Image W + Δ + O<sub>3</sub> + 0.5% HMW PEI + 0.5% BDD (A) after annealing (x100)



**Optical Image of W +  $\Delta$  + O<sub>3</sub> + 5% HMW PEI + 0.5% BDD (B) after annealing (x100).**



**W+ O<sub>3</sub> +0.5% LMW PEI + 0.5% BDD (C) after annealing (x100).**

## 9. UV-Raman Spectra of annealed samples

